OPTISCHE SPEKTROSKOPIE STARK KORRELIERTER ELEKTRONENSYSTEME

Zur Erlangung des akademischen Grades eines

DOKTORS DER NATURWISSENSCHAFTEN

von der Fakultät für Physik der Universität (TH)

Karlsruhe

genehmigte

DISSERTATION

von

Dipl.-Phys. Andreas Schumacher

aus Neuenbürg

Tag der mündlichen Prüfung: 16. Februar 2001
Referent: Prof. Dr. Daniel S. Chemla
Korreferent: Prof. Dr. Claus Klingshirn

Zusammenfassung

Die vorliegende Arbeit stellt zeitaufgelöste, nicht–lineare optische Studien und lineare optische Messungen an stark korrelierten Elektronensystemen vor. Darunter versteht man metallische Systeme, bei denen der Beitrag der Coulombwechselwirkung zwischen den Elektronen über die Fermienergie dominiert. Aus der starken Coulombwechselwirkug der Elektronen resultieren eine Vielzahl interessanter Phänomene und elementare Anregungen magnetischer und elektronischer Natur. Ein tiefergehendes Verständnis dieser Anregungen, ihrer Wechselwirkungen und Symmetrien ist von Interesse für Theorien beispielsweise zum Quantenmagnetismus oder der Hochtemperatur–Supraleitung. Diese Dissertation untersucht solche Zusammenhänge, und konzentriert sich dabei auf zwei Typen von Elementaranregungen, die für stark korrelierte Elektonensysteme charakteristisch sind: Das "Charge–Transfer" (CT) Exziton ist die fundamentale, elektronische Anregung für Energien im Bereich optischer (∼1–3 eV) Übergänge, wo die untersuchten Systeme durch den Hubbard–Hamiltonoperator beschrieben werden können. Auf einer niedrigeren Energieskala (∼100 meV) sind die dominierenden Anregungen magnetischen Ursprungs. Diese können im Rahmen des Heisenberg–Hamiltonoperators verstanden werden, der die Niedrigenergie–Näherung des Hubbard–Hamiltonoperators für stark korrelierte Elektronensysteme im Grenzfall starker Kopplung darstellt.

Für den experimentellen Teil der Arbeit wurde ein Aufbau entwickelt, der Ultrakurzzeitspektroskopie über einen weiten Bereich von Pump- und Abfrageenergien, Polarisationszuständen und Temperaturen ermöglicht.

Zeitaufgelöste Untersuchung der Spinwellen–Dynamik in Cr_2O_3

Im Zentrum des ersten Teils der Arbeit steht die Dynamik von Spinwellen kurzer Wellenlänge. Dazu wird mittels Femtosekunden Pump-Abfragespektroskopie der Exziton-Magnon (X-M) Übergang in dem antiferromagnetischen Übergangsmetalloxid Cr_2O_3 mit zeitlicher und spektraler Auflösung studiert. Die X-M Anregung kann als magnetisches Seitenband eines Exzitons bei 1.72 eV aufgefasst werden. Effektiv wird somit die Zustandsdichte für magnetische Anregungen zu höheren Energien hin verschoben, wodurch antiferromagnetische Spinwellen durch einen im nahen Infrarot operierenden Femtosekundenlaser *optisch* angeregt werden können. Bedingt durch den Anregungsmechanismus in unserem Experiment sind diese optisch erzeugten

Spinwellen vorwiegend zu großen **k**-Vektoren hin gewichtet. Die Dichte der somit erzeugten Nichtgleichgewichts–Verteilung am Zonenrand ist groß genug, um Wechselwirkungseffekte und eine Energie-Renormierung der Spinwellen beobachten zu können.

Wir berichten über einen neuartigen nichtlinearen optischen Effekt, der aus der Nichtgleichgewichts–Verteilung kurzwelliger Spinwellen zu resultieren scheint. Erst Δt=100 ps *nach* der optischen Anregung mit einem 100 fs Laserpuls kann eine Renormierung der Magnonenenergie experimentell gefunden werden. Die gemessene Energieänderung stimmt dann gut mit den Vorhersagen existierender Spinwellentheorien überein, wenn eine Renormierung der Spinwellen–Dispersionsrelation durch die optisch erzeugten Spinwellen angenommen wird. Bei einem kürzeren Zeitabstand zwischen Anregung und Abfrage jedoch weichen unsere Beobachtungen dramatisch von existierenden Theorien ab: das erwartete Signal bleibt zuerst nahezu vollständig aus, und wächst erst auf einer ps–Zeitskala zu dem erwarteten Wert hin an. Dies deutet darauf hin, daß die ursprünglich erzeugten, kurzwelligen Magonen nicht wie erwartet zur Renormierung beitragen. Erst auf einer Zeitskala von 100 ps relaxieren die Spinwellen dann vom Rand der Brillouin–Zone zu deren Zentrum hin, wo sich der erwartete Renormierungseffekt einstellt. Ein phänomenologisches Modell, das die Brillouin–Zone in zwei Bereiche unterschiedlicher optischer Eigenschaften, für kurz- und für langwellige Magnonen, unterteilt, erklärt unsere Daten gut.

Lineare und nichtlineare Spektroskopie des Charge–Transfer Exzitons in $Sr_2CuO_2Cl_2$

Im Kern des zweiten Teils dieser Arbeit stehen die linearen und nichtlinearen optischen Eigenschaften des Charge–Transfer Exzitons in $Sr_2CuO_2Cl_2$. Dieses Material ist charakterisiert durch seine zwei–dimensionalen CuO_2 Ebenen und seine stabile Stochiometrie. Zwar wird es mangels freier Ladunsträger bei tiefen Temperaturen nicht supraleitend, ist aber das klassische Modellsystem für Hochtemperatur– Supraleiter im Grenzfall niedriger Dotierung. Wir beobachten erstmals eine Urbach–Ausläufer im optischen Absorptionsspektrum, der auch bei sehr tiefen Temperaturen nicht verschwindet. Der Urbach–Verlauf im allgemeinen und sein Tieftemperaturverhalten im besonderen können nur durch ein Modell erklärt werden, das eine starke Kopplung mittels Phononen zwischen dem CT Exziton und einer weiteren elektronischen, energetisch unter dem CT Exziton liegenden Anregung annimmt. Diese Therie wird in hier ausgeführt, und erklärt Messungen der linearen Absorption in $Sr_2CuO_2Cl_2$ über einen weiten Temperatur- und Energiebereich sehr gut.

Um Aufschluss über Zustände zu erhalten, die in der elektrischen Dipolnäherung für einen Ein–Photonen–Übergang verboten sind, wurde optische Frequenzverdreifachung in $Sr_2CuO_2Cl_2$ über einem weiten Energiebereich gemessen. Durch geschickte Wahl der Polarisation der Laserpulse können wir die nichtlineare

Suszeptibilität $\chi^{(3)}_{ijkl}(-3\omega;\omega,\omega,\omega)$ in der Cu–O Ebene—ein komplexwertiger Tensor vierter Stufe—vollständig charakterisieren. Wir sehen eine breite Resonanz in $|\chi^{(3)}_{xxxx}|$ im Bereich von 0.7 eV, und schließen durch Polarisationsmessungen auf eine zu Grunde liegende quasi–sphärische Symmetrie der Elektronenverteilung. Die Stärke der Resonanz legt eine drei–Photonen Anregung des CT-Exzitons aus dem Grundzustand nahe. Eine leichte Abweichung von der sphärischen Symmetrie könnte durch einen Cu $3d_{x^2-y^2}$ →Cu $3d_{3z^2-r^2}$ Zwischenzustand verursacht werden. Modellrechnungen zur nichtlinearen Suszeptibilität reproduzieren unsere Messergebnisse gut.

Abschließend präsentieren wir vorläufige Resultate zur zeitaufgelösten Spektroskopie des CT Exzitons über einen weiten Bereich von Anregungs– und Abfrageenergien. Der spektrale und zeitliche Verlauf des Signals legt—wie schon in der linearen Spektroskopie vermutet—eine starke Kopplung zwischen Phononen und CT-Exzitonen als den für die Dynamik Ausschlag gebenden Prozess nahe. Weitherin beobachten wir einen Sättigungseffekt im spektral aufgelösten Pump–Abfragesignal. Dessen Stärke findet sich im Einklang mit geometrischen Argumenten zur Phasenraumfüllung des CT–Exzitons.

Abstract

In this thesis, both time-resolved, nonlinear optical spectroscopy and linear spectroscopy are used to investigate the interactions and dynamics of elementary excitations in strongly correlated electron systems.

In the first part, we investigate the renormalization of magnetic elementary excitation in the transition metal oxide Cr_2O_3. We have created a nonequilibrium population of antiferromagnetic spin waves and characterized its dynamics, using frequency– and time–resolved optical spectroscopy of the exciton–magnon transition. We observed a time–dependent pump–probe line shape, which results from excitation induced renormalization of the spin wave band structure. We present a model that reproduces the basic characteristics of the data, in which we postulate the optical nonlinearity to be dominated by interactions with long–wavelength spin waves, and the dynamics due to spin wave thermalization.

Using linear spectroscopy, coherent third–harmonic generation and pump–probe experiments, we measured the optical properties of the charge–transfer (CT) gap exciton in $Sr_2CuO_2Cl_2$, an undoped model compound for high–T_c superconductors. A model is developed which explains the pronounced temperature dependence and newly observed Urbach tail in the linear absorption spectrum by a strong, phonon–mediated coupling between the charge–transfer exciton and ligand field excitations of the Cu atoms.
The third–order nonlinear optical susceptibility $\chi^{(3)}_{ijkl}(-3\omega;\omega,\omega,\omega)$ within the Cu–O plane of $Sr_2CuO_2Cl_2$ is fully characterized over an energy range from 0.6 eV to 1.5 eV in both amplitude and phase, and symmetry based conclusions are made with respect to the spatial arrangement of the underlying charge distribution. Theoretical considerations ascribe a newly reported resonance in $|\chi^{(3)}_{xxxx}|$ at 0.7 eV to a three–photon resonance with the charge–transfer exciton. An intermediate state, possibly of Cu $3d_{x^2-y^2}$ →Cu $3d_{3z^2-r^2}$ origin, is found to contribute to the transition.
Finally, preliminary results of time–resolved pump–probe spectroscopy confirm the strong coupling of the CT exciton or one of its constituent parts to LO-phonons. We suggest ultrafast thermalization with the lattice as the dominating mechanism underlying the dynamical properties.

Acknowledgements

If I have seen further it is by standing on ye shoulders of Giants

Newton to Hooke, Feb. 5th, 1676

Both in terms of scientific and personal development, a dissertation is a formidable endeavor. The privilege of of being guided and supported by truly exceptional people can therefore hardly be overstated. Beyond teaching me physics, Daniel Chemla set an example for a creative, thorough and healthy approach to physics. That he is always available and ready to help despite his workload is another thing which never ceases to amaze me. I spent most of my days together with Steve Dodge, and I cannot imagine a better teacher in the lab. Apart from discussing physics, I tremendously enjoyed the opportunity to talk about everything from South American policy to the Op–Ed in the New York Times.

Steve told me that getting Ph.D. is mostly about acquiring a certain way of thinking and approaching things—an attitude which surely cannot be learned in just three years. My parents deserve the largest credit for that, since they instilled curiosity and the joy of studying and learning into me. And thank you for all your support, love and help over many, many years.

Prof. Claus Klingshirn from the Universität Karlsruhe initially enabled my stay in Berkeley, and was a kind and helpful advisor despite the distance between Karlsruhe and Berkeley. My Berkeley years would not have been possible without financial support first and foremost by the German National Merit Foundation and also the German Academic Exchange Service DAAD.

In recent months, I enjoyed working with Robert Kaindl and Marc Carnahan. It was very fortunate for my thesis the Robert Lövenich provided invaluable input to the linear absorption theory, and worked out all the math.

The part of the second floor group which remained a constant during my time here were Neil Fromer, Jen Glass, Shimon Weiss, Gino Segrè and John Corson. I very much enjoyed the the time with you, and I'll miss you. Thank you, guys! John and Gino deserve special credit: for being good friends, good listeners and—using two slightly different approaches—for submerging me in American culture.

I would like to acknowledge many helpful discussions and support from the following people: Jean–Yves Bigot (Université de Strasbourg), Thilo Kopp (Universität Augsburg), Lance Miller (Ames Laboratory), Andy Millis (Rutgers University), Ted Norris (University of Michigan), Joe Orenstein (U. C. Berkeley), Sofia Reck (Stanford Synchrotron Radiation Laboratory), Robert Schönlein (Berkeley National Laboratory), Lou Sham (U. C. San Diego) and the Building 2 Machine Shop at LBNL.

On my first day in Berkeley, I met Julie. We became best friends and now we are married. Meeting her and her family was the most important and most fortunate thing which happened to me. Thank you Ruth, Larry, Amy, Emily and Rob for opening your hearts to me and for being so much *fun*. And thank you, Julie, for all your love and everything which plain words utterly fail to describe.

Contents

Zusammenfassung **I**

Abstract **V**

Acknowledgements **VII**

Table of Contents **IX**

List of Figures **XI**

I Introduction **1**
I.1 Motivation and Overview 1
I.2 Outline of this work 2

II Strongly correlated electron systems **5**
II.1 Strong correlation and the Hubbard model 6
II.1.1 The Hubbard model 6
II.1.2 Some properties of the Hubbard model 7
II.2 The Hubbard model in real materials 8
II.2.1 Transition metal oxides 9
II.2.2 Two dimensional cuprates and high-temperature superconductors 12

III Optical spectroscopy **15**
III.1 Theoretical aspects of optical spectroscopy 16
III.1.1 The limit of linear optics 17
III.1.2 Density matrix and time-resolved measurements 17
III.1.3 The linear susceptibility $\chi^{(1)}$ 19
III.1.4 The structure of higher-order susceptibilities 20
III.2 Experimental setup 22
III.2.1 The laser and amplifier system 23
III.2.2 Linear absorption measurements 27
III.3 Sample preparation 28
III.3.1 $Sr_2CuO_2Cl_2$ 28
III.3.2 Cr_2O_3 29

IV Spin-wave dynamics in Cr_2O_3 **31**
IV.1 Introduction 32
IV.1.1 Spin wave theory 32
IV.1.2 The exciton-magnon transition in Cr_2O_3 33
IV.2 Spectroscopy of the X-M transition 35
IV.2.1 Theory for long delay times 37
IV.2.2 Comparison to thermal difference spectroscopy 39
IV.2.3 Temporal evolution of the spin wave population 40
IV.3 Conclusions 44

V The charge transfer gap in $Sr_2CuO_2Cl_2$ **45**
V.1 Material characteristics of $Sr_2CuO_2Cl_2$ 46
V.2 Linear absorption near the CT gap 47
V.2.1 Existing theories of the charge transfer gap 47
V.2.2 Linear absorption and the Urbach tail 50
V.2.3 Theory 53
V.2.4 Conclusions 60
V.3 Coherent nonlinear optics at the CT gap 60
V.3.1 Resonant enhancement of $|\chi^{(3)}_{xxxx}|$ 61
V.3.2 Characterization of $\chi^{(3)}(-3\omega;\omega,\omega,\omega)$ 65
V.3.3 Model calculations for $\chi^{(3)}$ 71
V.3.4 Conclusions 73
V.4 Pump-probe spectroscopy at the CT gap 75
V.4.1 Previous pump-probe experiments in undoped cuprate materials 75
V.4.2 Instantaneous, spectrally resolved response 76
V.4.3 Temporal evolution of the pump-probe signal 81
V.4.4 Pump-probe experiments below the charge transfer gap . 83
V.4.5 Conclusions 84

Bibliography **87**

Publications **96**

List of Figures

II.1 Illustration of $3d$ orbitals 9
II.2 Possible excitations in a multi–band Hubbard model 10
II.3 Schematic density of states for a transition metal oxide 11
II.4 Phase diagram of $La_{2-x}Sr_xCuO_4$ 12
II.5 Schematic of a two–dimensional CuO_2 plane 13

III.1 Time scales for decay processes 18
III.2 Feynman diagrams for $\chi^{(3)}_{ijkl}$ 21
III.3 Layout of the optical table 23
III.4 Schematic of the regenerative amplifier 24
III.5 Spectra and pulse widths of the Ti:Al_2O_3 seed laser and the regenerative amplifier 25
III.6 Spectrum of the white light continuum 26

IV.1 Linear absorption spectrum of Cr_2O_3 34
IV.2 Schematic of the exciton-magnon excitation 35
IV.3 Schematic of a pump-probe experiment 36
IV.4 Pump-probe spectrum of Cr_2O_3 37
IV.5 Comparing theoretical and measured X-M absorption 38
IV.6 Comparison between pump-probe line shape, model calculations and thermal difference spectroscopy 40
IV.7 Time-resolved pump-probe signal in Cr_2O_3 41

V.1 Crystal structure of $Sr_2CuO_2Cl_2$ 46
V.2 Linear absorption near the CT gap in $Sr_2CuO_2Cl_2$ 48
V.3 Illustration of the charge-transfer exciton structure 49
V.4 Symmetries of CT exciton wave functions 50
V.5 Shift and broadening of the CT absorption peak 51
V.6 Experimental evidence for an Urbach tail in linear absorption . . 52
V.7 Calculated absorption for CT exciton only 57
V.8 Linear absorption in $Sr_2CuO_2Cl_2$, data and theory 59
V.9 Setup for phase- and amplitude measurement 62
V.10 Maker fringes in SiO_2 63
V.11 Third harmonic intensity in $Sr_2CuO_2Cl_2$ 64
V.12 Theoretical plot of total third harmonic intensity 67

V.13 Retardance measurement at 1.13 eV 68
V.14 Relative phase and absolute magnitude of $\chi^{(3)}_{xxxx}$ and $\chi^{(3)}_{xxxx}$ . . . 69
V.15 Models for the nonlinear response of $Sr_2CuO_2Cl_2$ 72
V.16 Instantaneous ($\Delta t \approx 0$) photoinduced changes in $Sr_2CuO_2Cl_2$ after excitation at 2.1 eV 77
V.17 Time and energy resolved plot of photoinduced response at 3.1 eV pump energy 78
V.18 Photoinduced response at 2.1 eV and 3.1 eV pump energy 79
V.19 Time–resolved spectroscopy at 3.1 eV pump and 2.1 eV probe energy 82
V.20 Time–resolved spectroscopy below the charge transfer gap 83

Chapter I

Introduction

I.1 Motivation and Overview

The large ($\approx 10^{23}$ cm^{-3}) number of interacting particles lies at the core of the difficulty when dealing with the solid state phase. Despite the fact that only the Coulomb force acts between the electrons and lattice ions of a solid, even the equilibrium state of matter is understood completely only for a few systems.

One of the most successful techniques of dealing with this challenge is that of *elementary excitations*. These are wave packets of the eigenstates of the fully interacting, many–body Hamiltonian which behave like the eigenstates of a much simpler system. One of the most powerful manifestations of this idea is Landau's Fermi–liquid theory: Under certain conditions, the excitations near the Fermi–surface are long–lived fermions ("Landau quasi–particles") which can be mapped onto the electron and hole excitations of a non–interacting Fermi gas. The physical properties of the interacting system are thus only quantitatively modified compared to the non–interacting case.

This simplification comes at a cost. The elementary excitations can exhibit an internal structure, and the vacuum state is no longer "empty" and featureless. In addition, the concept of elementary excitations is limited to certain conditions, mostly low energy and density. At higher densities, details about the internal structure of the elementary excitations become relevant and observable. Yet despite these limitations, the concept has been so successful that it is often taken for granted in solid state physics. However, there remain many examples of systems whose elementary excitations are only partially understood.

Strongly correlated electron systems are an interesting example of a physical system where many questions about elementary excitations remain open. The class encompasses such seemingly diverse materials as polymers, transition metals and their oxides, fullerenes (C_{60}), liquid helium and high–temperature su-

perconductors. The theoretical standard model used to describe these systems is the Hubbard model, and understanding the elementary excitations of this Hamiltonian is thus clearly of importance.

This thesis seeks to provide some new insight into the nature of the two basic elementary excitations of the Hubbard model in solids: Magnetic excitations at low energies and charge excitations at higher energies.

Spin waves—or magnons in the language of quantization—are the elementary excitation in the limit of low energies (∼100 meV), where in certain limits the Hubbard is equivalent to the Heisenberg Hamiltonian. Controlled theoretical approximations and extensive experimental investigations were carried our predominantly in the long–wavelength and low density limit. Short wavelength spin–waves are more difficult to treat theoretically, and even in three dimensions their mutual interaction is not fully understood. A better understanding of the Heisenberg Hamiltonian in two dimensions is thought by many to be a key in understanding high–temperature superconductivity. Our work is motivated by the desire to better understand the interactions between magnetic excitations with large **k** vector.

The fundamental elementary excitation of the Hubbard Hamiltonian at higher (∼1-2 eV) energies is the charge transfer exciton, which constitutes another example of a poorly understood elementary excitation. Its previously observed strong temperature dependence has been addressed only by a few authors. This is surprising, owing the importance of a coupling between excitations at optical energies on one hand and magnons or phonons on the other. Furthermore, numerous optically dipole allowed and forbidden excitations exist in the vicinity of the charge transfer gap and continue to be debated. This motivated us to examine the charge transfer exciton in an undoped parent compound of the high–T_c superconductors more carefully.

Nonlinear spectroscopy is a tool uniquely suited for the investigation of the large number of elementary excitations in strongly correlated systems: It allows us to excite very selectively specific sub–populations of the system, and then monitor their decay over a wide range of energies. By using different excitation and detection schemes, we can learn about the symmetry of excited and intermediate states, their decay channels and strength of coupling to other excitations. Merging the powerful techniques of nonlinear optical spectroscopy with the field of strongly correlated materials in a systematic way provides for a very interesting and still novel field of research.

I.2 Outline of this work

This thesis is organized as follows:

- In the next chapter, strongly correlated electron systems are briefly in-

troduced. The Hubbard model, which is the theoretical standard model for this class of materials is given, and its application to real materials discussed.

- In chapter 3, we will recall some of the theory of nonlinear optics and subsequently give an overview of the experimental techniques and setups employed for this thesis. We will also explain how the samples used for this work were prepared.
- Chapter 4 shows how time-resolved, nonlinear optical spectroscopy may be used to investigate the interactions and dynamics of magnetic degrees of freedom in a strongly correlated electron system.
- Chapter 5 turns to the charge–transfer transition at higher energies in the undoped cuprate $Sr_2CuO_2Cl_2$. We use linear spectroscopy, coherent third–harmonic generation spectroscopy and time–resolved spectroscopy to probe this transition.

Chapter II

Strongly correlated electron systems

The issue of strong electron–electron correlation is an important one in solid state physics, since it governs the ground and excited states of such seemingly different systems like high-temperature superconductors [7], polymers [71], transition metals and their oxides [39] or fullerenes [12]. While a single model cannot be expected to describe all these materials in detail, it is nevertheless possible to find an effective Hamiltonian which captures many of the basic principles. This *Hubbard* Hamiltonian is the most widely used model, and some its properties are briefly described here, most notably the metal–Mott insulator transition and the wealth of possible magnetic and charge excitations. A more complete review is well beyond the scope of this thesis; a very good introduction is given in Ref. [27].

Our experiments were carried out on two materials, Cr_2O_3 and $Sr_2CuO_2Cl_2$. Both belong to the class of transition metal oxides, where the partially filled and narrow $3d$ shells give rise to striking electronic and magnetic properties. While Cr_2O_3 has a three–dimensional structure and a total spin S=32, the most interesting properties of $Sr_2CuO_2Cl_2$ are due to its two–dimensional Cu–O square lattice with S=12. Such a structure, if doped appropriately with free hole carriers, gives rise to high–temperature superconductivity [7]. Due to its stable stoichiometry, $Sr_2CuO_2Cl_2$ serves as a model system for the high–T_c superconductors in the limit for low doping. While further details about both compounds and the excitations of interest will be given in the respective chapters V and IV, some common electronic features are introduced already here.

II.1 Strong correlation and the Hubbard model

The importance of strong correlation in solids was perhaps best exemplified by Mott in the following *Gedankenexperiment*:

> Consider a "crystal" composed of hydrogen atoms. In an independent–electron picture, the material appears as a conductor for all lattice constants, since its s-band is only partially filled. This metallic state is indeed realized for a lattice spacing small compared to the Bohr radius, where the electrons screen their mutual Coulomb interaction well. In the opposite limit, the non–interacting picture clearly fails, since the "crystal" should now more appropriately be thought of as an (insulating) hydrogen gas. The energy cost for double occupancy of a proton due to electron–electron repulsion is larger than the kinetic energy gained by delocalization, and hence the ground state consists of one electron per site. As a function of the lattice constant, the "crystal" undergoes a transition from insulating to metallic behaviour. This transition is called the Mott transition.

The insulating behaviour in such a *Mott-Hubbard insulator* can thus only be understood if the electrons' mutual interaction is taken into account. This provides a clear distinction to materials where the insulating behaviour is based on electron–ion interaction and can be approached within the framework of an effective *single* particle theory. Theses particles need not be single electrons, but within the framework provided by quasiparticle theory they can be described by non–interacting objects with a renormalized mass and energy. Examples of the latter category are band insulators (electrons interact with the periodic potential of the lattice), Peirls insulators (interaction between electrons and a static lattice deformation) and Anderson insulators (disorder–induced insulating behaviour). Care should be taken to differentiate between a Mott Insulator which does not require the existence of pre–formed magnetic moments for the metal–insulator transition, and the Slater insulator which turns into a metal above a critical temperature.

II.1.1 The Hubbard model

A simple Hamiltonian, which nevertheless captures the main ideas of Mott's model, was used by Gutzwiller [32], Kanamori [45] and Anderson [4], but formally introduced by Hubbard [39]. It contains a kinetic energy term, which captures the electrons' itinerant features, and the potential energy or interaction term. The latter gives rise to the electrons' correlated behaviour or even their localization into an insulating state:

$$\hat{\mathcal{H}} = -t \sum_{<ij>,\sigma} \hat{c}^{\dagger}_{i,\sigma}\, \hat{c}_{j,\sigma} + U \sum_{i} \hat{n}_{i,\uparrow}\, \hat{n}_{i,\downarrow}. \tag{II.1}$$

$\hat{n}_{i,\sigma}=\hat{c}^{\dagger}_{i,\sigma}\, \hat{c}_{i,\sigma}$ is the number operator for $\sigma=\uparrow,\downarrow$ spin electrons, and $< ij >$ denotes next nearest neighbor pairs. U is the interaction strength, which in this

simple model equals the sum of electron ionization energy and electron affinity, and t is the hopping matrix element between adjacent sites. In addition to these explicit parameters, the physical properties are implicitly influenced by the dimension d of the system, the electron density $n_\sigma = N_\sigma / L$ (L stands for the number of sites) and the temperature. In the derivation of this model, two assumptions are important: (a) only on–site, inter–atomic Coulomb interaction is considered, e. g. $\langle i,j|\frac{1}{r}|i,j\rangle \sim \delta_{ij}$ and (b) only *one* band with s-like character exists close to the Fermi energy, while the interaction with electrons of others bands can be represented through a Hartee–Fock mean field approach.

Variants of "the" Hubbard model (II.1) include modifications to accommodate hopping beyond next nearest neighbour sites, additional bands or further interaction terms. Yet despite its simplicity, no satisfying solution to (II.1) exists to date for all but some limiting cases.

II.1.2 Some properties of the Hubbard model

Despite still being a challenge to theorists and expemimentalists alike, some basic conclusions can be drawn for materials which are governed by the Hubbard Hamiltonian.

Limits of the Hubbard Hamiltonian

Exact solutions for the Hubbard model exist in a few limiting cases, such as for example:

- the Fermi gas limit for U=0, which describes an (ideal) metal lacking any correlation effects.
- the opposite case of t=0, which characterizes the "atomic" limit. The ground state is highly degenerate and insulating, since individual sites do not communicate with each other. The number of zero, single and double occupancies in the system is determined by the ratio NL, the interaction strength and the temperature.
- a case of great practical interest is the "large–U" limit, $U \gg t$. For arbitrary filling, one can then derive the "t–J model" [27], which is often used to model the copper-oxide planes in high-T_c materials [6] at low energies. In the additional limit of exact half filling ($2n_\uparrow$=$2n_\downarrow$=

  $$NL$$

  =1), the Hubbard model becomes equivalent to the (insulating) antiferromagnetic Heisenberg model

  $$\hat{\mathcal{H}} = J_{ij} \sum_{<ij>} \hat{\mathbf{S}}_i \cdot \hat{\mathbf{S}}_j. \tag{II.2}$$

  The exchange coupling J=$4t^2/U > 0$ sets the magnetic energy scale of the system.

Due to its importance, a large number of approximation methods exist for the theoretical treatment of the Hubbard model, as well as solutions in certain dimensional limits (in one or infinite dimensions). For a review, see Ref. [27].

Magnetic properties

General statements about the magnetic properties of even the simple, undoped Hubbard model are difficult to make and depend critically on the value of the total spin S and the dimension d of the system. However, in a simple Ising model, the presence of antiferromagnetic order can be understood intuitively:

Parallel spin alignment on two adjacent sites prohibits hopping and subsequent double occupancy due to Pauli's exclusion principle. If the spins are oriented in an anti–parallel fashion, hopping and double occupancies are no longer prohibited. The resulting delocalization of the electrons lowers the total energy of the system in second order perturbation theory by J=4t^2/U, thus resulting in an antiferromagnetic ground state.

Beyond the Ising model, the situation becomes more complicated: for the corresponding spin-1/2 Heisenberg chain however, no long range order (LRO) exists even at T=0 (for finite T, the Mermin-Wagner theorem rules out magnetic order in d=1 and 2 in the first place [68]). In the case of great interest for high-T$_c$ superconductivity—the two–dimensional, isotropic spin-1/2 Heisenberg antiferromagnet—no rigourous proof is known to us for either the existence or nonexistence of antiferromagnetic LRO at T=0. Anderson therefore conjectured a ground state which exhibits short-range order ("spin liquid" [5]). Despite the lack of theoretical confirmation however, it is widely believed that Néel long range order exists at T=0 K in the 2D, spin-1/2 case and spin-wave theory applies for this system [65].

In higher dimensions ($d \geq 3$), antiferromagnetic order has been proven to exist in for large total spins $S \geq 1/2$ [27] and below a critical temperature [23, 47]. This is very important for our experiments in chapter IV, where we compare our results to spin wave theory, which assumes a magnetically ordered state from which spin waves can arise. To assure that we conduct our experiments in a regime where spin wave theory applies, our investigation focused on the antiferromagnetic transition metal oxide Cr_2O_3, a three-dimensional, S=3/2 system.

II.2 The Hubbard model in real materials

We will now introduce some of the complications which arise if the Hubbard model is applied to real solid state materials. The remarks are limited to the compounds of interest in this work, the three–dimensional transition metal oxide

(TMO) Cr_2O_3, and the two–dimensional cuprate $Sr_2CuO_2Cl_2$.[1]

II.2.1 Transition metal oxides

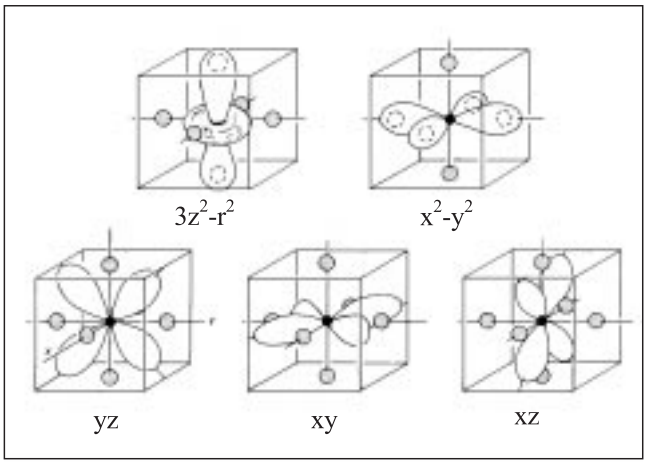

Figure II.1: $3d$ orbitals. The five–fold degeneracy is partially lifted in a cubic environment. A tetragonal distortion (not shown here) would further reduce the degeneracy and cause a splitting into (xz,yz), xy, $3z^2$-r^2 and x^2-y^2 states (listed by increasing *electron* energy).

Transition metal oxides exhibit a wide variety of electronic, magnetic and structural properties such as insulator–to–metal transitions, structural and magnetic phase transitions and even superconductivity if doped appropriately. These phenomena—and the difficulties in describing them—are a direct result of the highly correlated motion of the electron (or hole) quasiparticles in the partially filled, well localized and narrow $3d$ orbitals.

In the perovskite structure, a transition metal ion is surrounded by six oxygen ions O^{2-}, which give rise to the crystal field potential. The free rotation symmetry of the electrons is hindered and the orbital angular momentum quenched by the crystal field splitting of the d orbitals. The $d_{x^2-y^2}$ and $d_{3z^2-r^2}$ wave functions point towards the oxygen ions and have higher energies than the d_{xy}, d_{yz} and d_{xy} orbitals. When electrons are placed into these orbitals, their distribution is determined by the semi–empirical Hund's rule [20]. Depending one the filling of the d states, either a electron or hole quasiparticle picture is typically adopted to describe the material.

[1] It should be noted that a large body of work deals especially with the issue of high-temperature superconductivity, and that we do not attempt to review all the issues surrounding these materials in general

One of the assumptions in the Hubbard model, that only on-site Coulomb interaction needs to be considered, is justified since the Coulomb matrix elements between the well localized bands decay fast with distance.

No longer though can a one–band model sufficiently describe the material, and the Hubbard model has to be treated as a many–band problem [27]. As a consequence, the magnetic ground state, together with on-site and intra-site excitations, allows for a wealth of possible excitations.

Multiple excitation energy scales

If magnetic ordering exists, it is possible to excite magnetic spin waves with an energy $J \sim$10–200 meV in addition to electronic excitations at higher energies (Chapter IV deals with the behaviour of such spin waves at short wavelengths and high densities). Figure (II.2) schematically illustrates such a situation. "A"

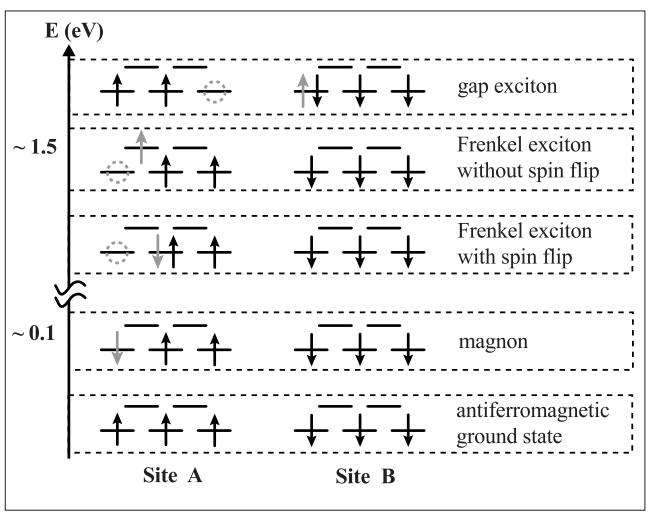

Figure II.2: Possible excitations in a multi–band Hubbard model. "A" and "B" depict two adjacent sites of the antiferromagnetically aligned sublattices. Three quasi-particles occupy the degenerate intra–atomic levels, oriented in accordance with Hund's rule

and "B" depict two adjacent sites of the antiferromagnetically aligned sublattices. Expanding on the one–band Hubbard model, in this cartoon we allow for six atomic orbitals, which are characterized by two intra-atomic energy levels (2– and 3–fold orbitally degenerate). Each of the six orbitals is 2–fold spin degenerate. This describes for example a situation where the 5–fold degeneracy of the $3d$ orbitals is partially lifted by a cubic crystaline environment. Such effects are not included in the simple Hubbard Hamiltonian (II.1), but cannot be neglected here. In this example, three electron quasiparticles occupy the lowest

energy states. Their spins are aligned in accordance with Hund's rules. The lowest energy excitation is of magnetic origin and consists in this cartoon of a spin flip on one site [2]. Due to the spin–reversal involved, the spin–wave cannot be excited by linear optical methods. At higher energies, electronic *intra–atomic* and therefore charge–neutral excitations can be accessed, which involve changes in the *orbital* symmetry, either with or without a spin flip and therefore either optically dipole forbidden or allowed, respectively. Both excitations can be viewed as tightly bound Frenkel excitons, since both the electron and hole reside on the same lattice site. Finally, the gap energy for charged excitations is given by the electron–transfer energy from one site to the next, and marks the onset of (optical) conductivity.

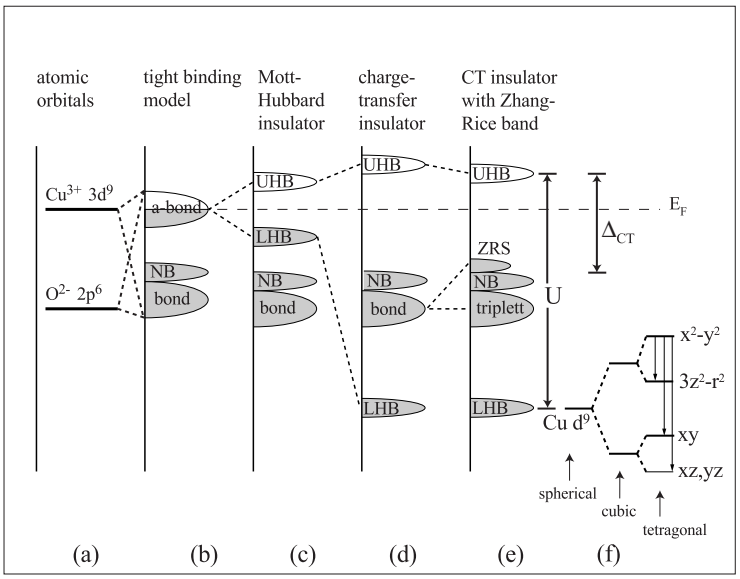

Figure II.3: Schematic density of states for a transition metal oxide. (a) atomic orbitals. (b) in a single–electron tight binding picture the oxygen–like bonding bands (bond) and non–bonding band (NB) lie below E_F, whereas the anti-bonding (a-bond) bands are close to E_F. (c) on–site Coulomb interaction splits the conduction band into lower (LHB) and upper (UHB) Hubbard bands. (d) for $\Delta_{CT} < U$, the material is a charge transfer insulator. Δ_{CT} is the gap between the highest oxygen–like state and the UHB. (e) Cu $3d$–O $2p$ hybridization creates Zhang–Rice singletts (ZRS, see chapter V) just below the UHB. (f) charge–neutral on–site excitations can occur within the LHB, and are influenced by the crystal symmetry

[2] This "local" picture is oversimplified. In reality, the spin flip is distributed over the lattice due to the translational symmetry, resulting in a spin wave. Going one step further, these spin waves can be quantized, which leads to the concept of magnons

This gap excitation can also be thought of as an exciton. Although in this simple picture one would expect again a Frenkel–type small exciton, hybridization in real materials increases the excitons' size somewhat. Another important modification affects the interaction energy U. In real materials, depositing or removing an electron from a nearby s level, or from the p levels of neighbouring oxygen atoms might be energetically more favourable than the charge transfer from one TM site to the next. This is schematically shown in Figure (II.3) for the example of a Cu–O material:

In a non–interacting tight–binding model, the atomic Cu^{2+} $3d^9$ and O^{2-} $2p$ orbitals hybridize and form mixed Cu $3d$ and O $2p$ bands. Strong on–site Coulomb interaction then splits the former "conduction" band into a lower and an upper Hubbard band. If the oxygen p band lies between the two Hubbard bands, the energy for charged excitations is no longer determined by the Hubbard U but by the *charge transfer* energy Δ_{CT}. The insulator is hence called a charge–transfer insulator.

II.2.2 Two dimensional cuprates and high-temperature superconductors

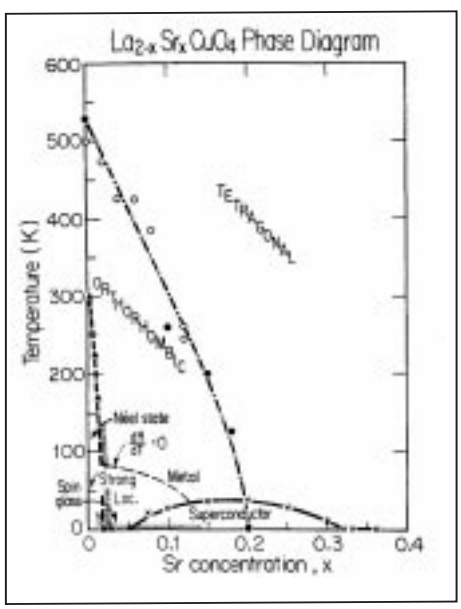

Figure II.4: Phase diagram of cuprate $La_{2-x}Sr_xCuO_4$. From Ref. [46].

Two features are common to all high–T_c superconducting materials. First, they are quasi—two-dimensional and the structural key units are the CuO_2 layers. The interplane coupling is weak, and at half–doping, the planes themselves are a very good realization of the two–dimensional Heisenberg quantum antiferromagnet. Second, superconductivity sets in at a low temperature when charge carriers are added to this Mott insulator.

Early cuprate compounds such as $La_{2-x}Sr_xCuO_{4+\delta}$ with a T_c=38 K display a reasonably simple structure. But the complexity seems to increase with T_c, as the record of 133 K for $HgBa_2Ca_2Cu_3O_{8+\delta}$ shows. So from a conceptual point of view it seems advantageous to focus on the simpler, perhaps even the undoped parent compounds.

When (hole) carriers are added to the two–dimensional TM oxide layers by electrochemical techniques or substitution of buffer layer ions, numerous phase transitions occur as shown for $La_{2-x}Sr_xCuO_4$ in Fig (II.4). Substitution of Sr^{2+} for La^{3+} introduces holes to the CuO_2 layers, which results in a rapid drop in the Néel temperature, until antiferromagnetic LRO is completely suppressed above x_c=0.02. For doping levels above x_c, various forms of local or incommensurate magnetism survive even into the superconducting phase [75]. Superconductivity sets in at about 5% doping and reaches the highest T_c around x_c=0.15. In addition to the electronic and magnetic phase transitions, structural transitions appear as well [46].

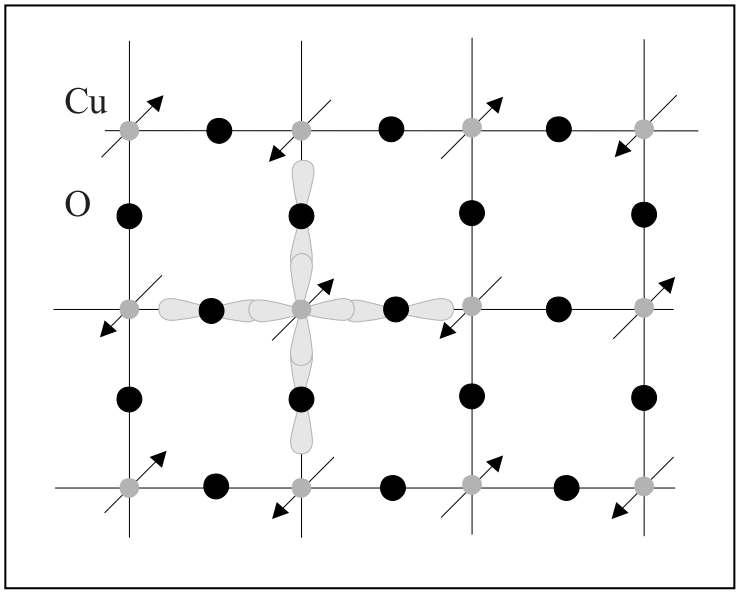

Figure II.5: Schematic of the two–dimensional CuO_2 plane common to all high–temperature superconductors. Arrows indicate a possible alignment of spins in the antiferromagnetic ground state. In the undoped case (half–filling), one hole resides on each copper ion in a $3d_{x^2-y^2}$ symmetry. Shaded areas visualize the Cu d and O $p\sigma$ orbitals responsible for strong correlation and superexchange, respectively.

Since the hybridization between Cu $3d$ and O $2p$ bands again leads to the formation of a charge transfer rather than Hubbard gap, a model based on equation (II.1) fails to model the detailed electronic structure of the CuO already in the undoped parent compounds. Instead, a three–band model of one copper and two oxygen levels is often employed ("Emery model" or "Varma–Schmitt-Rink–Abrahams model" [25, 101]). There, to supplement the original Hubbard U_d between the copper d electrons, additional correlation terms govern

the oxygen p electrons and nearest neighbour interaction between Cu $3d$ and O $2p$ electrons. Since exchange between the Cu d orbitals is mediated by oxygen, it leads to a strong "superexchange" coupling $J \sim$100 meV despite the large spatial separation of two copper ions.

It has been argued that this three-band Hubbard model can be reconciled with an effective one–band model, which at least captures the low energy physics of the superconductors [6]. Just below the charge transfer gap, the Cu–O hybridization leads to the formation of a "Zhang-Rice" singlett (see chapter V and [111]). Since the so formed electron–hole pair does not disturb the antiferromagnetic background, it has a large bandwidth and can be viewed as a spinless exciton quasiparticle.

Chapter III

Some aspects of optical spectroscopy and experimental techniques

The previous chapter illustrates how strongly correlated systems exhibit a wealth of excitations, which can be both optically dipole active and inactive (but allowed e. g. as a two–photon transition) and are spread over a wide range of energies.

Before introducing the experimental techniques used in this work, to probe these excitations, some aspects of linear and nonlinear optical spectroscopy are highlighted. Many of these issues are now well known and documented, and therefore we will only summarize results that are important for the work presented here. Particular emphasis is placed on how macroscopically observable quantities, such as the index of refraction n and the absorption coefficient α can be related to underlying microscopic effects. We will also discuss how coherent nonlinear processes can be applied to identify and characterize electronic states inaccessible to linear optics. Finally, we will briefly comment on the transition between the coherent and incoherent regime as it relates to the investigation of relaxation processes of non–equilibrium populations.

The second section describes the core parts of the optical setup. It incorporates a 100 fs mode-locked Ti:Al_2O_3 laser, a 250 kHz, μJ regenerative amplifier system and a near-IR optical parametric amplifier (OPA) as excitation light sources. Supercontinuum generation [1] allows us to cover the wide range of probe energies mandated by our choice of sample materials. Towards the end of the chapter, some comments will be made on sample preparation.

III.1 Introduction to some aspects of linear and nonlinear optical spectroscopy

Nonlinear optics describes phenomena which result from the modification of the optical properties of a material through interaction with intense light. To understand the underlying microscopic structure of the material and why it changes, we need to make the link between microscopic physics and changes in the way light interacts with the material. This short section can only highlight some of the aspects which we deem relevant for the understanding of this work. Comprehensive reviews of nonlinear optics can be found in the books of Boyd [9] or Shen [87].

In the dipole approximation, the propagation of electromagnetic waves in matter is governed by the wave equation, driven by the polarization created in the sample[1] (in cgs units)

$$\left[\nabla^2 + \frac{1}{c^2}\frac{\partial^2}{\partial t^2}\right]\mathbf{E}(\mathbf{r},t) = -\frac{4\pi}{c^2}\frac{\partial^2 \mathbf{P}(\mathbf{r},t)}{\partial t^2} \tag{III.1}$$

Information about the physical properties of the material is contained in the polarization $\mathbf{P}(\mathbf{r},t)$, which in general depends in a complicated manner upon the incident electrical incident field $\mathbf{E}(\mathbf{r},t)$. Once $\mathbf{P}(\mathbf{r},t)$ is known as a function of the electric field, time and the population state of the system, Eq. (III.1) needs to be solved self–consistently. Neglecting magnetic effects and within the dipole approximation, the polarization is a function of the electrical field only, and this relation can be expressed in the form of a Taylor series

$$\mathbf{P} = \chi^{(1)} \cdot \mathbf{E_1} + \chi^{(2)} : \mathbf{E_1}\mathbf{E_2} + \ldots + \chi^{(n)} \vdots \mathbf{E_1} \cdots \mathbf{E_n} \tag{III.2}$$

where $\chi^{(n)}$ is a complex tensor of rank $(n+1)$ called the nonlinear susceptibility of nth order. Deriving $\chi^{(n)}$ from microscopic parameters such as orbital– or band structures and energy levels not only gives access to the absolute value of the nonlinear susceptibility, but also leads to characteristic internal symmetries of the tensor. In solids, knowledge of crystal symmetries can be used to *a priori* reduce the number of independent and non–zero elements of $\chi^{(n)}$ considerably. A demonstration of how crystal symmetries on one hand and symmetries in the measured optical response on the other can be facilitated to systematically explore $\chi^{(n)}$ is given in chapter V.

Eq. (III.2) is frequently expressed in frequency space. Again in the dipole ap-

[1] In this brief overview, we neglect magnetic interactions, which might at first seem surprising given the magnetic structure of many strongly correlated systems. Yet the significance of magnetic effects diminishes rapidly at the higher frequencies of optical spectroscopy.

proximation, it reads

$$\mathbf{P}^{(n)}(\mathbf{k} = \sum_{\alpha=1}^{n} \mathbf{k}_\alpha, -\omega; \sum_{\alpha=1}^{n} \omega_\alpha) = \chi^{(n)}(\omega_1, \ldots, \omega_n) \vdots \mathbf{E}(\mathbf{k}_1, \omega_1) \cdots \mathbf{E}(\mathbf{k}_n, \omega_n). \tag{III.3}$$

The sums on the left hand side of this equation are due to energy and momentum conservation, and therefore $\omega = \sum_{\alpha=1}^{n} \omega_\alpha$. It is worth noting that the $\mathbf{k}$–vector dependence only needs to be considered if the optical response has a nonlocal character. If the response is local, i. e. the polarization at a point $\mathbf{r}$ is independent of $\mathbf{P}(\mathbf{r}')$, the $\mathbf{k}$–dependence of $\chi^{(n)}$ can be neglected.

III.1.1 The limit of linear optics

In the limit of linear optics, only terms of (III.3) to first order in the electric field are considered. Introducing the frequency dependent dielectric constant

$$\varepsilon(\omega) = \varepsilon_1(\omega) + i\varepsilon_2(\omega) = 1 + 4\pi\chi^{(1)}(-\omega; \omega) \tag{III.4}$$

establishes the link with the two commonly used quantities of linear optics, the index of refraction n and the absorption coefficient $\alpha(\omega)$:

$$\begin{aligned} \alpha &= \frac{\omega}{c_0}\frac{\varepsilon_2}{n} \\ n &= \sqrt{\frac{1}{2}(\varepsilon_1 + \sqrt{\varepsilon_1^2 + \varepsilon_2^2})} \end{aligned} \tag{III.5}$$

Very often, one finds that $\varepsilon_1 \gg \varepsilon_2 \geq 0$, which finally leads to

$$\begin{aligned} n &\simeq \sqrt{\varepsilon_1} \\ \alpha &\simeq \frac{\omega}{c_0}\frac{\varepsilon_2}{\sqrt{\varepsilon_1}}. \end{aligned} \tag{III.6}$$

Under the very general assumptions of local response and causality ($\chi(t - t') \equiv 0 \; \forall \; t' > t$), complete (over the entire frequency range) knowledge of either the absorption coefficient α or the index of refraction n can be used to calculate the respective other with the help of the Kramers–Kronig relations [49]. "Complete" information is of course difficult to obtain, but in practice it is often sufficient to know ε_1 or ε_2 in a frequency band not too narrow around the energy of interest.

III.1.2 Density matrix and time-resolved measurements

One common formalism for calculating the polarization and describing the temporal evolution of the system is by means of the density matrix operator $\hat{\rho}(t)$ of the system [9],

$$\hat{\rho}(t) = \overline{|\psi(t)\rangle\langle\psi(t)|} \tag{III.7}$$

where the overbar represents the ensemble average. In this notation, the time–evolution of the system is governed by the Liouville equation, and the expectation value of the polarization is evaluated by taking the trace of the product of $\hat{\rho}(t)$ and the operator $\hat{\mathbf{P}}(\mathbf{r},t)$:

$$\begin{aligned} \frac{\partial}{\partial t}\hat{\rho}(t) &= -\frac{i}{\hbar}[\hat{\mathcal{H}}(\mathbf{E}(\mathbf{r},t)),\hat{\rho}(t)] \\ \mathbf{P}(\mathbf{r},t) &= tr(\hat{\rho}\cdot\hat{\mathbf{P}}). \end{aligned} \tag{III.8}$$

The diagonal matrix elements ρ_{nn} of the density matrix give the probability for the system to be in the energy eigenstate n. The coherence of the system is described by the off-diagonal elements ρ_{mn}, which are only non–zero if the system is in a coherent superposition of states. Physical processes which are characterized by $\rho_{mn} \neq 0$ are said to take place in the *coherent* regime. After the coherence is lost during random scattering events, the population relaxation takes place in the *incoherent* domain. In general, equations (III.8) and (III.1)

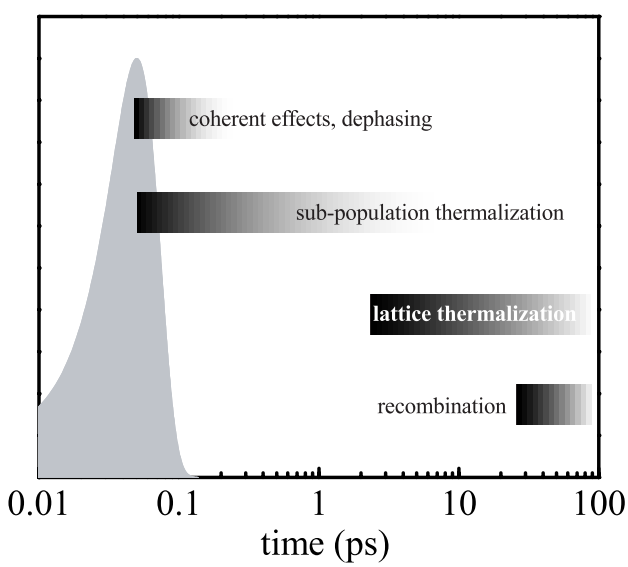

Figure III.1: Time scales for decay processes in solids. The system loses coherence on a ps time scale T_2 after excitation. At the same time, a population relaxation starts, and the system thermalizes into a hot Fermi distribution. Eventually it cools to the lattice temperature via the emission of phonons.

need to be solved in a self–consistent manner to determine the temporal evolution of the system. Relaxation terms are added to the Liouville equation by

hand. Two decay rates are needed to describe the time–dependent properties of the system:

- The dipole dephasing or transverse relaxation rate γ_{nm}=1/T_2 gives the damping rate of the coherence. Typical time scales for T_2 are ten to a few hundred femtoseconds.
- $\Gamma_{nn\rightarrow mm}$=1/$\mathrm{T}_1$ describes the population decay from level n into level m. The population decays in general much more slowly than the coherence; $\mathrm{T}_1 \gg \mathrm{T}_2$.

If the Liouville equation is evaluated with the added relaxation terms, it eventually leads to the optical Bloch equations [9], which is beyond the scope of this work.

III.1.3 The linear susceptibility $\chi^{(1)}$

We will now give the explicit expression for the linear susceptibility $\chi^{(1)}$. The derivation in the framework of the density matrix formalism is given in textbooks [9] and we display only the final result:

$$\chi^{(1)}_{ij}(-\omega;\omega) = \frac{N}{\hbar}\sum_{gm}\rho^0_{gg}\left[\frac{\langle g|\mu^i|m\rangle\langle m|\mu^j|g\rangle}{(\Omega_{mg}-\omega)-i\gamma_{mg}} + \frac{\langle g|\mu^j|m\rangle\langle m|\mu^i|g\rangle}{(\Omega_{mg}+\omega)+i\gamma_{nm}}\right] \qquad \text{(III.9)}$$

Here, N is the number density of atoms or molecules, μ^i (i=x,y,z) the i-th component of the electric dipole operator μ=-e·$\mathbf{r}$ and $|g\rangle$ the ground state of the system. Together with the value of the matrix elements $\langle g|\mu^i|m\rangle$, the transition energy Ω_{nm} and the line width γ_{nm} provide information about the system:

Symmetry: Since μ is an odd operator, only transitions between states of different parity can contribute to $\chi^{(1)}$. By examining linear optical spectra, we can therefore gain some insight into the the symmetry of the underlying electronic states. Yet at the same time, the inability to observe transitions between states of equal parity sets a fundamental limit to linear spectroscopy.

Energy levels: Inspecting (III.9), it is clear that the expression for $\chi^{(1)}$ undergoes a resonance as $\omega \rightarrow \pm\Omega_{mg}$ This corresponds to transition lines observed in linear absorption spectra, with a width given by the damping γ_{mg} and an oscillator strength governed by the value of the matrix elements $\langle g|\mu^i|m\rangle$. The following chapters will illustrate how changes in Ω_{mg} and γ_{mg} provide insight into physical problems:

- In chapter IV, we show how through a laser pulse and by (thermal) heating the population density n($\mathbf{k}$) in a specific subsystem can be altered, which gives rise to a renormalization of the energy levels, Ω_{mg}=Ω_{mg}(n($\mathbf{k}$)). Either a second light pulse (in the case of pump–probe spectrosopy) or a simple light bulb for linear absorption experiments can probe these changes.

- The first section of chapter V illustrates how coupling between excitations, mediated through phonons, influences the line width and the energy of the transition under investigation.

III.1.4 The structure of higher-order susceptibilities

Going beyond optical effects due to a linear field–dependence of the polarization greatly expands the amount of information we can obtain through spectroscopy. As a reminder, Table (III.1.4) gives an overview of some of the nonlinear effects which can arise from higher order susceptibilities:

order	susceptibility	optical effect
1	$\chi^{(1)}(-\omega;\omega)$	linear refraction
	$\Im\chi^{(1)}(-\omega;\omega)$	linear absorption
2	$\chi^{(2)}(-\omega;\omega_1,\pm\omega_2)$	frequency mixing
		$(\omega=\omega_1\pm\omega_2)$
	$\chi^{(2)}(-\omega;\omega,0)$	Pockels effect
	$\chi^{(2)}(-2\omega;\omega,\omega)$	second–harmonic generation
3	$\chi^{(3)}(-\omega;\omega_1,\pm\omega_2,\pm\omega_3)$	four–wave mixing
		$(\omega=\omega_1\pm\omega_2\pm\omega_3)$
	$\chi^{(3)}(-3\omega;\omega,\omega,\omega)$	third–harmonic generation
	$\chi^{(3)}(-\omega;\omega_1,\omega_1,-\omega_2)$	Raman scattering
		$(\omega=2\omega_1-\omega_2)$
	$\Im\chi^{(3)}(-\omega;\omega,\omega,-\omega)$	two-photon absorption

Table III.1: Some nonlinear effects of order n

Importantly, we showed in (III.1.3) that linear optical techniques are unable to access states of the same parity as the ground state. For the optical spectroscopy of strongly correlated materials, this is a serious limitation, since a large number of same–parity excitations exist. It will be demonstrated below that nonlinear techniques can overcome this limitation. Some $\chi^{(3)}$ sensitive techniques, most notably Raman spectroscopy, have been used extensively in the past to probe transitions which are forbidden in optical spectroscopy [31, 57].

In all centrosymmetric crystals—such as the materials investigated in this work—the second order susceptibility $\chi^{(2)}$ vanishes identically due to symmetry considerations [9]. We will therefore restrict our comments to $\chi^{(3)}$.

The derivation of the full expression for $\chi^{(3)}$ is rather lengthy and will again be skipped. Diagramatic techniques are generally used to calculate higher order susceptibilities, since they not only give simple rules for representing and writing higher–order terms, but also illuminate the microscopic processes. The eight basic diagrams to be considered for $\chi^{(3)}$ are shown in Fig. III.2. Information

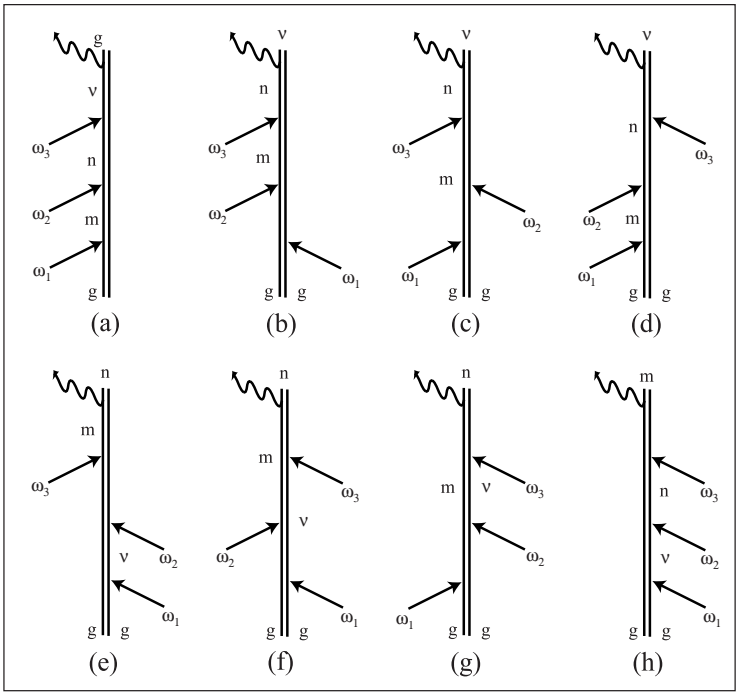

Figure III.2: The four basic Feynman diagrams for $\chi^{(3)}_{ijkl}$. (a) through (d) correspond to term one through four in Eq. III.10.

about diagramatic techniques can be found e.g. in Ref. [87], but unfortunately, different rules have been adopted by different authors.

$$
\begin{aligned}
\chi^{(3)}_{ijkl}(-\omega;\omega_1,\omega_2,\omega_3) &= \frac{N}{\hbar^3}\mathcal{P}\sum_{gmn\nu}\rho^0_{gg} \\
&\times\Bigg\{\frac{\langle g|\mu^i|\nu\rangle\langle\nu|\mu^j|n\rangle\langle n|\mu^k|m\rangle\langle m|\mu^l|g\rangle}{[(\Omega_{\nu g}-\omega_3-\omega_2-\omega_1)-i\gamma_{\nu g}][(\Omega_{ng}-\omega_2-\omega_1)-i\gamma_{ng}][(\Omega_{mg}-\omega_1)-i\gamma_{mg}]} \\
&+\frac{\langle g|\mu^l|\nu\rangle\langle\nu|\mu^i|n\rangle\langle n|\mu^j|m\rangle\langle m|\mu^k|g\rangle}{[(\Omega_{n\nu}-\omega_3-\omega_2-\omega_1)-i\gamma_{n\nu}][(\Omega_{m\nu}-\omega_2-\omega_1)-i\gamma_{m\nu}][(\Omega_{\nu g}+\omega_1)+i\gamma_{\nu g}]} \\
&+\frac{\langle g|\mu^i|\nu\rangle\langle\nu|\mu^k|n\rangle\langle n|\mu^l|m\rangle\langle m|\mu^j|g\rangle}{[(\Omega_{n\nu}-\omega_3-\omega_2-\omega_1)-i\gamma_{n\nu}][(\Omega_{\nu m}+\omega_2+\omega_1)+i\gamma_{\nu m}][(\Omega_{mg}-\omega_1)-i\gamma_{mg}]} \\
&+\frac{\langle g|\mu^j|\nu\rangle\langle\nu|\mu^i|n\rangle\langle n|\mu^k|m\rangle\langle m|\mu^l|g\rangle}{[(\Omega_{\nu n}+\omega_3+\omega_2+\omega_1)+i\gamma_{\nu n}][(\Omega_{ng}-\omega_2-\omega_1)-i\gamma_{ng}][(\Omega_{mg}-\omega_1)-i\gamma_{mg}]} \\
&+\ldots\text{(four additional terms)}\ldots\Bigg\}
\end{aligned}
\tag{III.10}
$$

($\mathcal{P}$ is a permutation operator, which accounts for the fact that e.g. in process (a) of Fig. (III.2), the order in which the absorption of the three photons ω_1, ω_2 and ω_3 takes place is arbitrary).

The third order susceptibility has eight basic terms, each corresponding to one of the diagrams shown in Fig. (III.2) and additional permutations of those. Since at this point only the general structure is of interest, we give only the first four terms here. They describe the processes depicted by (a)–(d) in Fig. (III.2). The complete expression can be found e. g. in Ref. [9].

From the structure of Eq. (III.10) it becomes clear how involving higher–order processes, transitions between odd *and* even parity states can now be resonant. As in the case of $\chi^{(1)}$, resonances still occur if energy levels close to $\omega{=}\omega_1 \pm \omega_2 \pm \omega_3$ exist. But since resonances can now occur with the absorption of one, two or three photons, a transition between two states with the same parity is no longer forbidden. It should be pointed out however that the interpretation of experimental data can also be complicated by the larger number of possible resonances. Additional information, e.g. about the phase or the relative strength of different tensor elements is needed to distinguish between odd and even parity excitations. In the second part of chapter V, we show how carefully evaluating the symmetry properties of the excitation can clarify the picture.

To summarize, we illustrated how the underlying electronic structure influences the optical properties of solids. Nonlinear optical spectroscopy is a valuable tool to probe the different excitations and their mutual interactions in strongly correlated systems. Even in the incoherent regime, a considerable amount of information can be extracted:

- Lasers can be used to excite non–equilibrium sub–populations of the solid at different energies very selectively.
- Already the presence or absence of a signal contains information about *symmetry* properties of states involved. Through nonlinear processes of different order in the incident electric field, both optically dipole allowed and dipole forbidden states can be accessed.
- By studying various decay products, information can be extracted about the relevant degrees of freedom of the originally excited state.
- Studying the decay time in the incoherent regime helps to determine the strength of the coupling between different degrees of freedom.

III.2 Experimental setup

In this section, we give a practical overview of the experimental techniques, and in particular over the laser systems used in this thesis. A general outline of the

optical setup and its main experimental components is shown in Fig. (III.3).

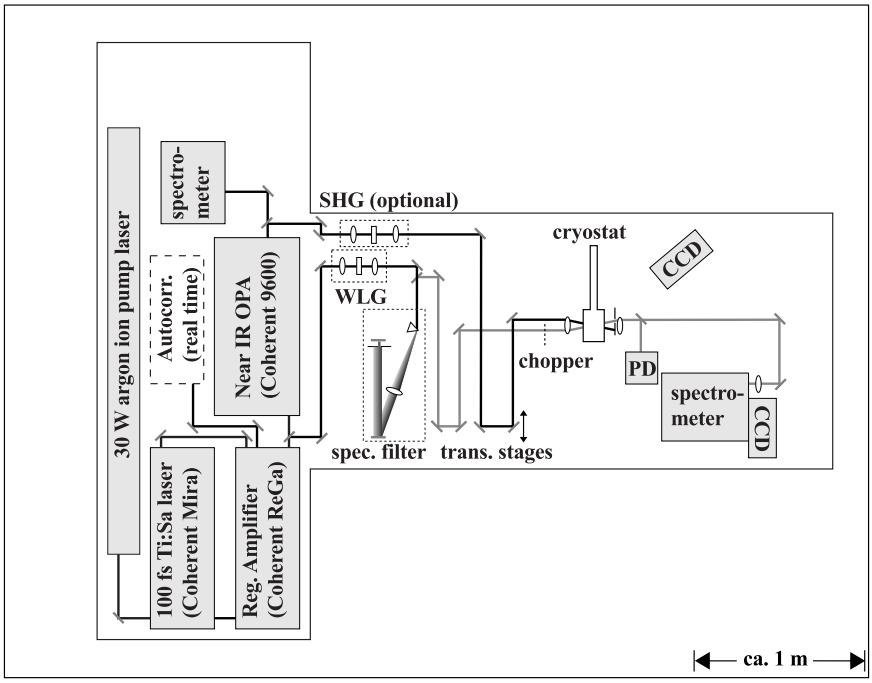

Figure III.3: Layout of the optical table. Autocorr.: real time and stepper motor autocorrelator, non–colinear geometry. SHG: 1 mm BBO crystal for frequency doubling of the near-IR OPA (optional). WLG: Supercontinuum generation in a 3 mm sapphire crystal. PD: UV enhanced Si large area photo diode for time-resolved measurements. A CCD camera is used to monitor the beam positions on the sample. Not shown are various filters and polarization optics used in different experiments.

III.2.1 The laser and amplifier system

Mode–locked 100 fs Ti:Al_2O_3 laser

The laser used for all experiments is a 100 fs Ti:Al_2O_3 laser (Coherent Mira 900F). It operates on the principle of passive mode–locking: the Ti:Al_2O_3 crystal acts both as an amplification medium and, by means of the optical Kerr–effect, as the mode–locker [91]. The Kerr effect induces an intensity–dependent self–focusing of the cavity mode, which results in selective amplification for the more intense parts of the beam. A slit inside the laser cavity serves as a hard aperture for the lower–intensity pulse components. To compensate for group velocity dispersion accumulated during the circulation of the femtosecond pulse

inside the laser cavity, the laser is equipped with an internal prism compensator. The system is pumped by 8 W partial output of a 30 W Ar^+ ion laser (Coherent Innova 400). It very reliably produces output pulses at 800 nm with temporal width of 100 to 150 fs and a pulse energy of about 1 nJ (see Fig. III.5). The typical peak–to–peak noise is 2%, and limited by the pump laser. For the nonlinear measurements on Cr_2O_3, we took advantage of the wide tuning range (695-1030 nm) of the mode locked laser. If used as a seed laser for the regenerative amplifier system, only 30% of the laser output is needed, the remainder is available for pulse characterization.

Regenerative amplifier

Initial attempts to use a home–built regenerative amplifier system [84] did not succeed in obtaining the same day–to–day reliability as a commercial system. Hence, experiments were performed with a Coherent RegA9000 amplifier, which uses a design by Ted Norris [72].

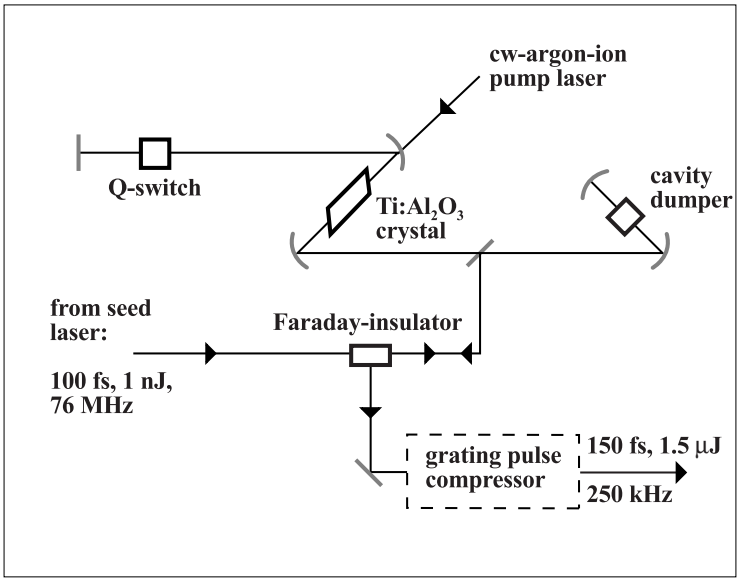

Figure III.4: Schematic of the regenerative amplifier.

The amplifier facilitates the principle of "chirped–pulse" amplification. If the pulse length were to remain unchanged during the amplification process, the peak intensities inside the amplifier cavity would quickly lead to nonlinear effects or even damage to the optical components [92]. To counter the high peak intensities, pulses can be either stretched in time before they are injected into the amplifier, or allowed to broaden passively while circulating in inside the cavity. In both cases, a pulse compressor shortens the pulse after amplification,

ideally to its initial length. In our system, group velocity dispersion inside the regenerative amplifier cavity is used to stretch the pulse.

The amplifier is seeded by the partial output of the Ti:Al_2O_3 laser and pumped by 12 to 14 W of the cw Ar^+ ion laser. Unlike pulsed pump laser systems, the continuous pumping allows for amplifier repetition rates up to 300 kHz, since the rate is only limited by the inverse gain recovery time of the Ti:Al_2O_3 crystal (If a pulsed pump laser is used, its repetition rate typically limits the overall system performance to some 10 kHz). A schematic of the amplifier is given in Fig. (III.4). During the pumping part of the amplification cycle, an acousto-optical Q-switch suppresses lasing in the resonant amplifier cavity, and a population inversion builds up in the continuously pumped Ti:Al_2O_3 crystal. Pulses with a duration of 100 fs and an energy of 1 nJ then seed the amplifier by means of a second acousto-optical element, the cavity dumper. Coincidental with the injection of a seed pulse, the intra–cavity Q-switch opens the cavity, thereby allowing the seed pulse to circulate in the amplifier resonator and to be amplified during multiple passes. After 24 to 27 round trips, the population inversion is depleted and the pulse energy has reached a saturation value. The latter is important, since it allows the peak–to–peak noise to be kept at 2-3%. The amplifier pulse is then ejected from the cavity through the cavity dumper. Due to group velocity dispersion, the pulse has broadened in time to about 20 ps. This is the desired effect of chirped–pulse amplification.

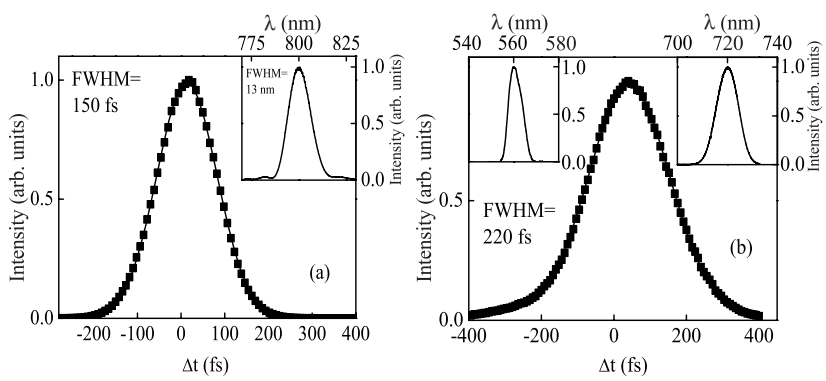

Figure III.5: Typical laser spectrum and autocorrelation. (a) output of the Ti:Al_2O_3 seed laser. From this measurement, the time-bandwidth product $\Delta\nu\Delta t$=0.67 for a Gaussian profile. (b) autocorrelation of an amplifier pulse, together with narrow probe spectra obtained by filtering of the white light continuum at different wavelengths.

A Faraday–insulator prevents back–reflection of the output into the seed laser and directs the amplified pulse towards a grating compressor [98]. Here, the

20 ps long pulse is re–compressed to below 200 fs. With a well–aligned system, we obtained pulse energies of 4-5 μJ after the compressor. Fig. (III.5) shows typical spectra and autocorrelations of both the seed laser and the amplifier system.

White light generation

We used 300 mW of the total amplifier output to create a stable white light probe continuum [1,10,79]. A white–light supercontinuum is one of the most fascinating examples for nonlinear effects in matter. The intensity–induced change in the index of refraction of the material leads to self–focusing and strong self–phase modulation. As a result, the bandwidth of the pulse is broadened dramatically. In the case of our 800 nm, near-IR input pulse, the generated continuum spans from 500 nm to above 1100 nm. To achieve white–light generation, amplified pulses are focused with a f=32.5 mm plano–convex lens into a 3 mm thick sapphire disc (c-axis normal to the surface) and re–collimated with a f=25 mm achromat. An iris in front of the focusing lens allows fine–tuning of the input beam parameters and influences the spectral composition of the continuum slightly. An example of the continuum spectrum is displayed in Fig. (III.6).

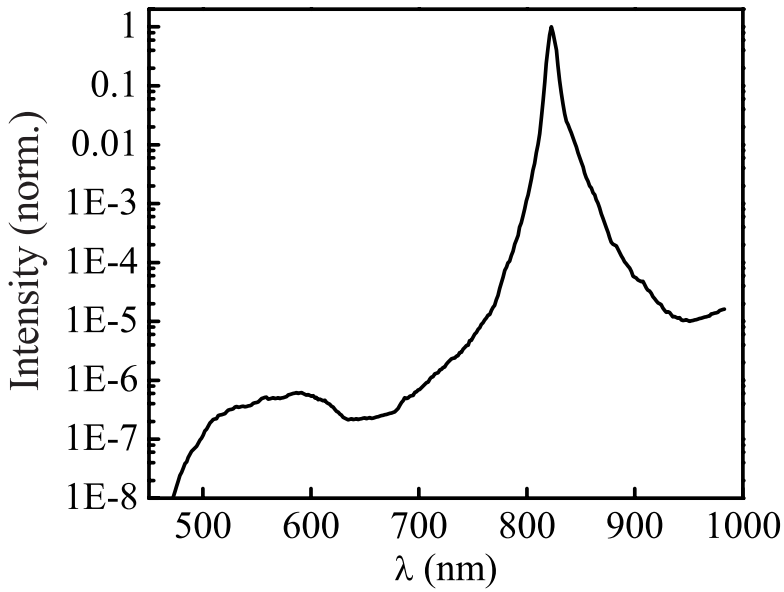

Figure III.6: Spectrum of the white light continuum. The resolution at the long-wavelength side is limited by the spectrometer. The spectrum shows the typical plateau on the high–energy side [10].

After collimation, we used a zero-dispersion prism stretcher as a spectral filter (Fig III.3). With a variable slit on a translation stage, a 7–10 nm wide part of the continuum can be selected and tuned continuously from 550 nm to 740 nm. For wavelengths closer to the fundamental of 800 nm, we were not able to obtain a clean spectrum. Two examples of the probe spectra obtained from the continuum are shown in the inset of Fig. (III.5.

Optical parametric amplifier

High power pump pulses covering the range from 1150 nm to 1800 nm were obtained by means of an optical parametric amplifier (Coherent OPA 9600) [78]. In the optical parametric amplification process, a strong pump pulse $(\omega_p, \mathbf{k}_p)$ is used to amplify weak input pulses at signal $(\omega_s, \mathbf{k}_s)$ and idler $(\omega_i, \mathbf{k}_i)$ frequency. Energy and momentum conservation dictate $\omega_s+\omega_i=\omega_p$ and $\mathbf{k}_s+\mathbf{k}_i=\mathbf{k}_p$ [107].

Weak seed pulses at $(\omega_s, \mathbf{k}_s)$ are generated by a second white light continuum created inside the OPA. One particular wavelength then needs to be selected for amplification. This is accomplished by changing the phase matching angle [107] between $\mathbf{k}_s$ and $\mathbf{k}_p$. In our system, a 3 mm thick type II BBO crystal is employed for parametric amplification, and rotating it provides the desired modification of the phase matching conditions. Both pump and signal beam pass through the crystal twice, which results in a significant increase in output power compared to single–pass systems [78]. A series of dichroic mirrors separate pump, signal and idler wavelengths after the parametric process. In the wavelength range from 1200 nm to 1500 nm, we routinely obtained pulse energies of $\sim$1 μJ and a spectral width (FWHM) of 40-60 nm. Towards longer wavelength the performance dropped somewhat but $\sim$0.1 μJ were still available at 1700 nm.

After the amplifier, a 1 mm thick BBO crystal was optionally employed to double the frequency of the OPA output externally.

III.2.2 Linear absorption measurements

We measured the linear absorption of our samples by illuminating them with an incandescent light bulb. Since some of the samples (the thin $Sr_2CuO_2Cl_2$ crystals, which will be further described below) had a very small homogeneous surface area of only ($\sim$20 μm)^2, we built a spectrometer with a very small focal spot size and the capability to keep the samples at a wide range of temperatures. Light from a tungsten lamp illuminated a pinhole with a specified diameter of 5 μm. This pinhole was then imaged with an f=70 mm achromatic lens doublet and a long working–distance microscope objective into a continuous flow liquid helium cryostat (Oxford Instruments "He–Microstat"). The beam diameter at the focus as measured by a 10% to 90% knife–edge test was only 3 μm. After the sample, the light was directed into a 0.25 m spectrometer and detected either by a CCD array or a silicon photodiode. We used 400 gr/mm and 1200 gr/mm gratings depending on the desired resolution. Spectra were taken with and with-

out the sample in place, and the absorption coefficient was calculated using the expression

$$\alpha(\omega) = \frac{-1}{L} \ln \frac{I_{sample}}{I_{sub}}. \tag{III.11}$$

L is the sample thickness, which we obtained by transmission measurements with a HeNe laser in the case of $Sr_2CuO_2Cl_2$ and through the spacing of interference fringes in the case of Cr_2O_3. I_{sample} and I_{sub} are the transmitted intensity with the sample plus substrate and only the substrate in place, respectively.

III.3 Sample preparation

Two different sample materials were used for the experiments described in this thesis. Here, we will briefly comment on their growth and preparation. Details about the properties of strongly correlated materials in general can be found in chapter II, and about the optical properties of Cr_2O_3 and $Sr_2CuO_2Cl_2$ in chapters IV and V, respectively.

III.3.1 $Sr_2CuO_2Cl_2$

The high quality $Sr_2CuO_2Cl_2$ single crystals used for this work were grown by L. L. Miller [69] at Iowa State University. The synthesis involves mixing of the stoichiometric precursors $SrCuO_2$ and $SrCl_2$, which are then reacted to monophasic $Sr_2CuO_2Cl_2$. Due to its very stable stoichiometry, $Sr_2CuO_2Cl_2$ is of great interest for experimentalists, and any attempt to dope it with oxygen so far has failed. Crystals are grown by melting and very slow cooling of the compound. The black, hygroscopic crystals are then mechanically removed. Raw samples provided to us had a typical (001) or (a,b) surface area of a few mm^2 and were 0.1–1 mm thick. The micataceous nature of the material allowed us to tape-cleave very thin single crystals.

In preparation for cleaving, we attached a crystal to a microscope slide with crystal bond. This "master sample" was then tape–cleaved until it became visually transparent under a 20× microscope (Often, the layers which were removed from the master sample and remained attached to the cleaving tape could be used as a starting point for further cleaving). Since the absorption coefficient of $Sr_2CuO_2Cl_2$ in the visible range of the spectrum is $\approx 1\times10^5$ cm^{-1}, this corresponds to a thickness of ≈100 nm. The crystal bond was then dissolved in a special solvent (Crystal Bond Stripper®) which did not etch the sample or degrade the surface quality of the fragile crystal pieces. The thin samples were subsequently floated onto a c-axis oriented sapphire substrate. Due to the mechanical cleaving, it was not possible to obtain *thin* samples with a homogeneous surface area of much more than $(80\ \mu m)^2$. During sample handling, a constant flow of dry nitrogen was maintained over crystal. Otherwise, the humidity in

the laboratory would lead to surface degradation over a few minutes to an hour.

Finding the correct orientation of these small samples with respect to the (a,b) axes (along the Cu–O bonding direction) proved to be a difficult task. We decided to orient the crystals only after the cleaving, since their orientation was hard to preserve during the removal/transfer process. Large sample pieces of crystal could readily be characterized with a Laue camera in back–scattering geometry. But once a sufficiently small ($\sim$50 μm diameter) aperture was inserted to minimize the strong background signal from the sapphire substrate, the X-ray flux from the Laue camera was too small to provide a signal. Eventually, we aligned the crystal at Beamline 2.2 of the Stanford Synchrotron Radiation Laboratory (SSRL), where a much higher X-ray flux was available.

III.3.2 Cr_2O_3

We obtained our Cr_2O_3 sample from Nick Ingle in the group of M. R. Beasly at Stanford University. The sample was a 2.2 μm thick film grown epitaxially on a sapphire substrate, by evaporation of Cr in a reactive oxygen environment. The c–axis of both Cr_2O_3 and sapphire were normal to the film surface. The sample as mounted on the substrate was both mechanically and chemically very stable, and no further processing on our part was required.

Chapter IV

Time-resolved optical observation of spin-wave dynamics

The low energy scale in strongly correlated electron systems is set by the magnetic interaction energy $J{=}4t^2/U$. Neglecting electronic excitations at higher energies, the Hubbard Hamiltonian is in the limit of strong interaction and half-filling approximated by the magnetic Heisenberg Hamiltonian

$$\hat{\mathcal{H}} = J_{ij} \sum_{<ij>} \hat{\mathbf{S}}_i \cdot \hat{\mathbf{S}}_j, \tag{IV.1}$$

where i, j denote next nearest neighbor sites. The understanding of this phase and its elementary excitations remains a fundamental problem of solid state physics and beyond [21]. Renewed attention was brought to the Heisenberg model with the discovery of high-T_c superconductivity, since it is generally assumed that the ground state of the undoped parent compounds of high-T_c superconductors is well described by the Heisenberg Hamiltonian in two dimensions [65]. Understanding the elementary excitations and interaction mechanisms of the Heisenberg model therefore poses a challenge for solid state physics. These elementary excitations are magnetic spin waves or magnons in their quantized form. Their theoretical understanding is well developed only in the long wavelength, low density limit, and optical observations were so far mostly limited to that region as well. But it is the short wavelength regime which is of great current interest, e. g. in the interpretation of mid-infrared absorption data from high-T_c superconductors [30, 58].

In this chapter, we demonstrate how time-resolved, nonlinear optical spectroscopy may be used to investigate the interactions and dynamics of such short wavelength spin waves. At short times after optical excitation, our results deviate sharply from the predictions of spin wave theory. A phenomenological model is given which accounts for the observed effects.

IV.1 Theoretical aspects of spin wave theory and the exciton magnon line

IV.1.1 Spin wave theory

In the periodic lattice of a magnetic crystal the concept of a spin wave appears naturally when the fermionic spin-Hamiltonian is expressed in terms of Boson operators. Bloch first described the concept of a spin wave as the reversal of a single spin in a ferromagnetic lattice, coherently distributed over the crystal [8]. His theory explicitly assumes a low density of spin waves, so that interactions among them may be neglected. The same constraints apply to a later model by Holstein and Primakoff (H-P), who introduced creation and annihilation operators for spin waves in ferromagnets [38]. This gave rise to the concept of magnons as the quanta of magnetic excitations. Anderson and Kubo [3,53] extended the concept to describe the ground state of antiferromagnets with large total spin S.

The assumption of a large total spin S is an important one, since spin wave theory consists of an expansion in powers of $1/(zS)$, z being the coordination number. The second condition on which the theory rests is that of long-range order (LRO) in the ground state. Dyson was the first to point out limitations of the $1/(zS)$ expansion and offered a more rigorous general theory of spin waves in a ferromagnetic compound [24]. Oguchi then reconciled the Holstein-Primakoff picture with Dyson's expansion to first order in $1/(zS)$ in what is now used as the prevailing model for spin wave theory [74].

In the absence of an external field, the spin-wave modes of the different antiferromagnetic sublattices are degenerate, and the antiferromagnetic Hamiltonian $\hat{\mathcal{H}}^{SW}$ is identical to the simpler ferromagnetic one [105]:

$$\hat{\mathcal{H}}^{SW} = JNzS^2 - \sum_k \omega_k \hat{n}_k + \frac{1}{4JNzS^2} \sum_{k,k'} \omega_k \omega_{k'} \hat{n}_k \hat{n}_{k'}. \tag{IV.2}$$

$\hat{n}_k = \hat{a}_k^\dagger \hat{a}_k$ are the number operators for quantized spin waves, and ω_k their (unrenormalized) energies[1]. The condition that the free energy of the system is an extremum with respect to the average occupancies $\langle n_k \rangle$ determines the occupancies to have a Bose-Einstein form with a renormalized energy $\bar{\omega}_{\mathbf{k}}$

$$\bar{\omega}_{\mathbf{k}}(\{n_{\mathbf{k}'}\}) = \omega_{\mathbf{k}}^0 [1 - \frac{1}{zJS^2N} \sum_{\mathbf{k}'} \langle n_{\mathbf{k}'} \rangle \omega_{\mathbf{k}'}]. \tag{IV.3}$$

(here, we omit a constant factor which sets the antiferromagnetic case apart from the ferromagnetic one. Since it does not depend on the spin wave density, we cannot observe it in our experiment) The sum $\sum_{\mathbf{k}'} \langle n_{\mathbf{k}'} \rangle \omega_{\mathbf{k}'}$ in eq. (IV.3)

[1] It should be noted that the expansion in $1/(zS)$ occurs at an earlier stage in the derivation. The third term on the reight hand side of eq. IV.2 reflects the first order Oguchi correction.

equals the total energy $\mathcal{E}_{tot}^{Mag}$ in the magnon subsystem, regardless of the **k**-space distribution and therefore:

$$\bar{\omega}_{\mathbf{k}}(\{n_{\mathbf{k}'}\}) = \omega_{\mathbf{k}}^{0}[1 - \kappa\mathcal{E}_{tot}^{Mag}] \tag{IV.4}$$

While this approximation is valid for long–wavelength spin waves at low excitation densities, much less is known about short–wavelength spin waves. Especially at higher densities, theory must be guided by experimental observations. Neutron spectroscopy and linear optical spectroscopy have provided some of the best evidence for the existence of spin wave renormalization at elevated temperatures [105, 108]. But as previous measurements were largely limited to thermally occupied spin waves, not much is known about the interactions among excitations at short wavelengths. Theory suggests that in ferromagnetic systems the interactions may undergo qualitative changes as the zone boundary is approached and bound states between two magnons can be formed [88, 106]. But to our knowledge, convincing experimental evidence has been lacking so far.

IV.1.2 The exciton-magnon transition in Cr_2O_3

Cr_2O_3 is an antiferromagnetic transition metal oxide with corundum structure and a Néel temperature of T_N=308 K.Since the optical spectrum of its dilute paramagnetic isomorph, i. e. ruby, is well understood, it constitutes a good material for nonlinear optical studies. In a cubic environment, the three electrons per Cr^{3+} site possess a ground state with $^4A_2$ symmetry and a lowest excited ^2E state at ~ 1.7 eV [61] (This $^4A_2 \rightarrow {}^2E$ transition is the one facilitated in the ruby laser). In a lattice, these levels couple via superexchange interactions J and J', of order 50 meV. The ground state multiplet develops into antiferromagnetic spin waves, and the excited state multiplets into magnetic exciton bands. Both excitations individually cannot be accessed optically due to the spin flip involved. Figure (IV.1) shows the linear absorption of Cr_2O_3 in the vicinity of the lowest lying magnetic exciton bands. The two excitons σ_1 and σ_2 are nominally spin and parity forbidden, and their separation is due to Davydoff-splitting [2]. They acquire a finite amount of oscillator strength due to single–ion spin–orbit coupling and the crystal field mixing between charge-transfer and 3 d^3 states [61].

The stronger optical absorption feature at 1.76 eV is an exciton-magnon (X-M) transition, which can be understood as a magnetic side band to the exciton. Such electric dipole exciton-magnon absorption was first seen in MnF_2 and has since then been studied in a number of other materials as well [28, 85]. For this X-M compound object, the total spin projection S_z is preserved by the two simultaneous spin excitations, so the spin selection rule $\Delta m = \Delta m_X + \Delta m_M = 0$ for optical dipole excitation is satisfied. To conserve the total momentum, the photon is absorbed by an exciton and a magnon of equal and opposite momentum, $\mathbf{k}_X + \mathbf{k}_M$=0. Figure (IV.2) illustrates the excitation mechanism schematically: In the antiferromagnetic ground state, $M_S = -\frac{3}{2}$ on sublattice A and

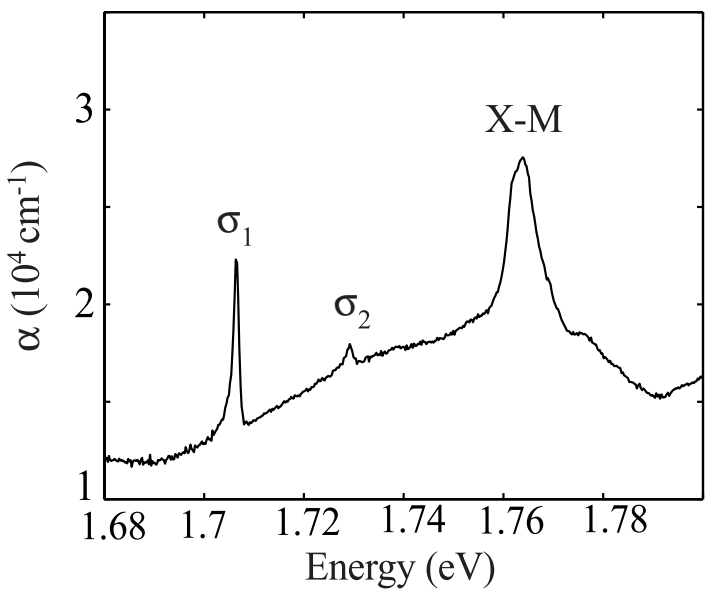

Figure IV.1: Linear absorption spectrum of Cr_2O_3 in the vicinity of the exciton magnon band. The two sharp features σ_1, σ_2 to the left are the optically weakly allowed $^4A_2 \rightarrow {}^2E$ excitons. The stronger absorption feature X-M to the right is the magnetic side band, or exciton-magnon compound object.

$M_S = +\frac{3}{2}$ on sublattice B. An electric field then induces a virtual transition into a higher-lying state of the Cr^{3+} ion on sublattice A. Parity must be conserved, hence the high-lying virtual state must be of opposite parity to the ground state. Due to the Coulomb interaction with neighboring ions on sublattice B, the excited ion on sublattice A relaxes to its first excited *electronic* state, while the ion on sublattice B is at the same time lifted to its first excited *spin* state. The excitation is largely localized to neighboring sites, and consequently draws its spectral weight from states over the entire Brillouin zone. However, since the magnon density of states is largest at the zone boundary, the distribution of magnons which are excited by this mechanism is weighted heavily towards short wavelength spin waves.

Neglecting interaction between the nearby exciton and magnon for clarity, the X-M absorption line shape is given approximately by the joint density of states (DOS) of excitons and magnons (phonon side bands can be ignored despite the localized character of the excitation, since the ^2E level couples very weakly to the lattice [61]):

$$\rho_{X-M}(\omega) = \sum_{\mathbf{k}} \delta(\omega - \omega^X_{\mathbf{k}} - \omega^M_{-\mathbf{k}}). \tag{IV.5}$$

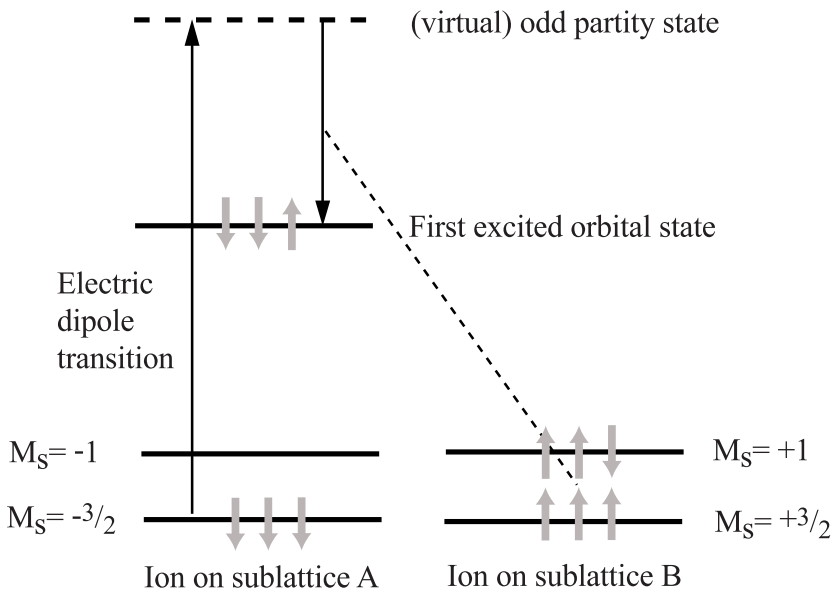

Figure IV.2: Optical excitation scheme of a (**k**,-**k**) exciton-magnon. Spin alignment in both the initial and final state is shown in grey. The ion on sublattice A forms a Frenkel exciton via a virtual transition. To conserve spin and momentum, a magnon with opposite momentum is formed on sublattice B.

The magnon dispersion is stronger than that of the exciton, and provides the dominant contribution to the line shape. The absorption feature may be qualitatively understood as the spin wave density of states, shifted up rigidly in energy by the exciton energy. This allows us to excite short wavelength spin waves and subsequently monitor their density of states, using a pulsed near-infrared laser.

IV.2 Time-resolved spectroscopy of the exciton-magnon transition

We have performed pump-probe spectroscopy of the X-M transition, using the 100 fs pulses emanating at 76 MHz from the Ti:sapphire laser system tuned to $\hbar\omega$ ≈1.765 eV (the regenerative amplifier and OPA were bypassed for this experiment). The beam is split in a 10:1 (pump:probe) ratio and the time delay, $\Delta t = t_{probe} - t_{pump}$ is controlled with the delay line.

Both pump and probe are focused through a microscope objective to a 6 μm diameter spot at the sample, which is held at 10 K with a cold finger cryostat. We estimate the average temperature at the sample to be $\leq$ 30 K, and at the

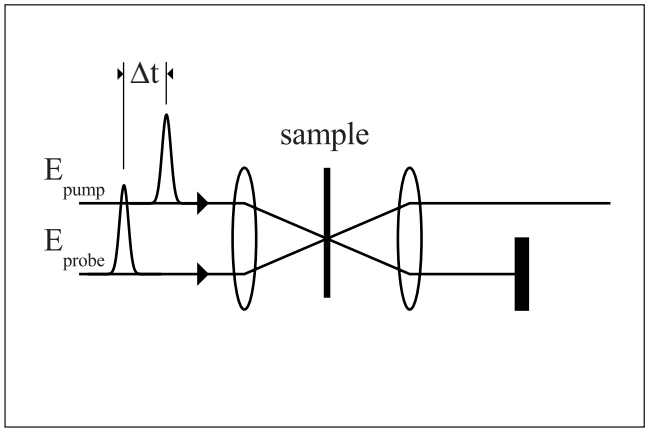

Figure IV.3: Schematic of a pump-probe experiment. A first pulse alters the optical properties of the sample. The probe pulse monitors these modifications, either by coherently interacting with the polarization induced by the pump, or by incoherently probing population changes.

peak of the X-M absorption line, the internal transmissivity of the sample is 52%.

After the sample we measure the relative change in transmission, ΔT/T as the pump beam is chopped mechanically to allow phase sensitive detection. The normalized change in transmission reproduces the differential absorption of the sample, by the relation $\Delta T/T \approx -\Delta\alpha\, L$ in the small signal regime. We measure ΔT/T as a function of wavelength and time delay, and subtract from this a small background contribution which persists at negative time delay because of the finite laser repetition rate. At excitation densities of $\sim 10^{-3}$/Crion, we observe the complex spectral feature shown in Fig. (IV.4) for three different time delays.

The data are well described in terms of two components: a spectrally featureless photo–induced absorption, which shifts the overall ΔT/T toward negative values and is relatively time independent over 100 ps, and a derivative–like line shape, which is very weakly evident at Δt=0 and *grows* as a spectral unit as Δt increases. This observation already is surprising, since in a "typical" pump–probe experiment the signal displays a very fast rise at Δt $\approx$0, followed by a decline in signal strength as the delay time increases and the population relaxes back into its the ground state.

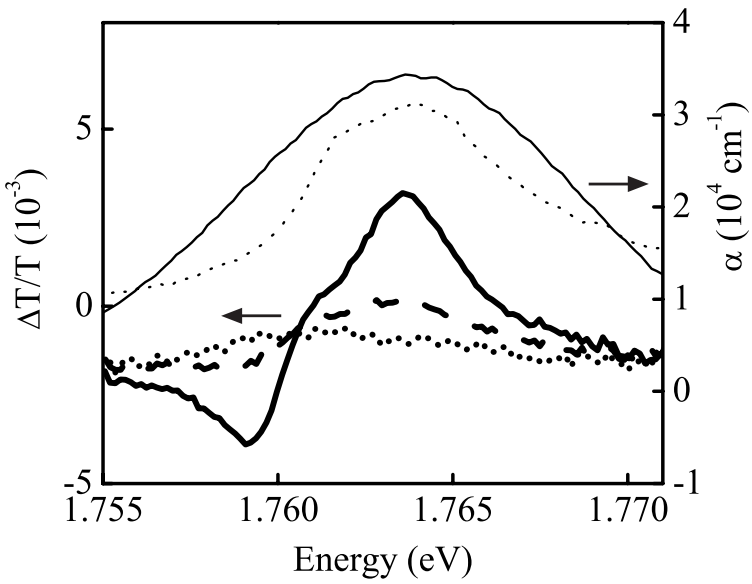

Figure IV.4: Pump-probe spectrum at $\Delta t = 0.3$ ps (heavy dotted line), 10 ps (heavy dashed) and 50 ps (heavy solid), with units given on the left, shown together with the absorption spectrum (light dashed), with units given on the right, and the incident laser spectrum (light solid), shown for reference in arbitrary units.

IV.2.1 Theoretical modeling of the signal at long time delays

To explain the magnitude and qualitative line shape of the nonlinear response shown in Fig. (IV.4), we modeled the expected renormalized line shape theoretically. Our calculations expand on an approach suggested by Macfarlane and Allen (MA) [61].

MA diagonalized the ligand-field Hamiltonian for the magnetic excitons of an isolated, single Cr^{3+}-ion analytically. Using numerical values obtained by linear spectroscopy, the model allows to calculate the exciton band structure without free parameters. Our own results of a calculation following this path are shown in the inset of Fig. (IV.5). The density of states of the exciton–magnon compound object can then be calculated (IV.5) using expressions for magnon dispersion and inelastic neutron–scattering data given by Samuelson [81]. A numerical evaluation can then be accomplished using a Monte-Carlo algorithm. Fig. (IV.5) displays our calculations, compared to measured linear absorption data. The model uses a number of approximations, i. e. (i) it neglects exciton–

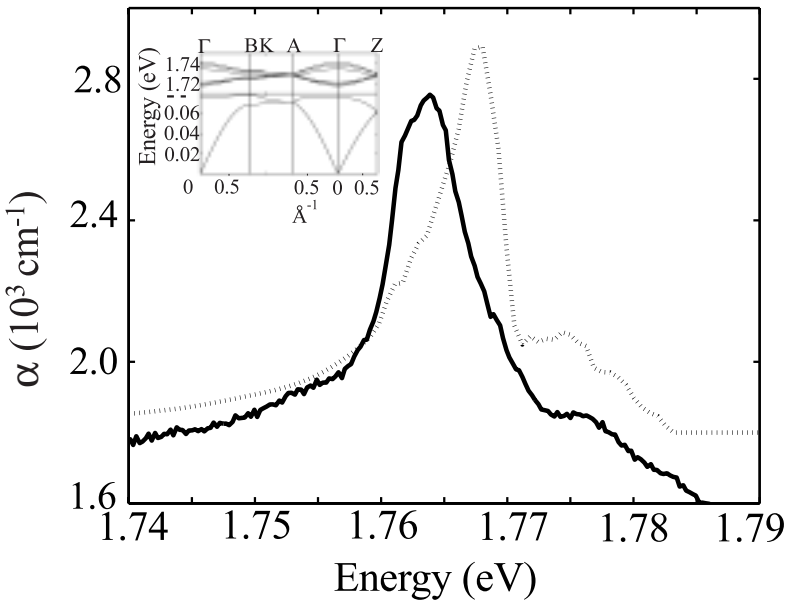

Figure IV.5: Comparison between the exciton-magnon absorption line as measured in linear absorption (solid) and the calculated absorption spectrum (dashed line) in Cr_2O_3. The inset details the calculated exciton and magnon dispersions along certain directions in the Brillouin-zone. The difference between experiment and theory may qualitatively be explained by the neglect of exciton–magnon interactions

magnon interaction, (ii) assumes equal coupling strength between all exciton branches and the magnon, (iii) uses next nearest neighbor approximations for the absorption mechanism and (iv) assumes that the exciton and magnon mode vectors are **k**–independent [61]. Despite these approximations, the theory compares well with the experimental line shape.

In our experiments, the X-M line shape reflects the renormalization of magnon energies (IV.3) following the optical excitation. The magnon energy $\bar{\omega}_{\mathbf{k}}(\{n_{\mathbf{k}'}\})$ (IV.3) and hence the joint density of states of excitons and magnons (IV.5) now depends on the magnon occupation $\sum_{\mathbf{k}'}\langle n_{\mathbf{k}'}\rangle\omega_{\mathbf{k}'}$. This results in a transient change in absorption, as $\alpha(\omega,\{n_{\mathbf{k}}\}) \simeq \rho_{X-M}(\omega,\{n_{\mathbf{k}}\})$ now depends on the time dependent distribution of photo–excited spin waves. The pump–probe experiment measures the time evolution of the now occupation–dependent absorption coefficient $\sum_{\mathbf{k}}\frac{d\alpha}{dn_{\mathbf{k}}}n_{\mathbf{k}}(t)$. In principle, the exciton dispersion relation should also be renormalized for the same reasons, but the exciton bandwidth is a factor of 2 narrower than that of the spin waves, and its dispersion is weakest near the zone boundary, so this effect contributes little to the overall line shape

change. Numerical simulations confirm these arguments. Since α is proportional to the integrated JDOS given in Eq. (IV.5), the total derivative $\frac{d\alpha}{dn_{\mathbf{k}}}$ includes two distinct contributions. One ($\frac{\partial\omega_{\mathbf{k}}}{\partial n_{\mathbf{k}}}$) stems from the level shifts and the other ($\frac{\partial\alpha}{\partial\omega_{\mathbf{k}}}$) from the change in the integration volume associated with the level shifts. Qualitatively, the level shifts produce an overall red shift in the energy, while the change in the integration volume reduces the spectral weight.

IV.2.2 Comparison between pump–probe spectrum and thermal difference spectroscopy

Owing to the fact that the renormalization is predicted to depend solely on the total amount of energy deposited in the sample (eq. IV.4), it is interesting to compare the pump-probe signal at long times to the change in the linear absorption induced by raising the temperature of the sample.

The spin wave energy absorbed from the laser is only $\mathrm{E_{magnon}/E_{exciton}} \sim 3\%$ of the total absorbed energy, so from the total incident energy density of 5.6 J/cm^3 only $\sim$ 100 mJ/cm^3 is absorbed by the spin wave system. From the known spin wave dispersion relation measured by neutrons [81], we may calculate the spin wave contribution to the specific heat, $C_p \simeq C_v = \frac{2\pi}{15}\frac{k_B^4}{D^3}T^3$, where $D \simeq 1.25 \times 10^{-28}$ Jcm. The energy density of one laser pulse thus corresponds to a temperature change of $\sim$ 60 K in the magnetic system. We measured the temperature dependent change in linear absorption α(60 K)-α(15 K), and in Fig. (IV.6), we compare the two.

To support our interpretation of the origin of the change of absorption, we also show the line shape calculated from equations (IV.5) and (IV.3), using a scale factor κ derived from the temperature dependent absorption spectra. The pump-probe spectrum has been scaled up by a factor of three, which may reasonably be attributed to the simplifications of Eq. (IV.3).

The good agreement among these curves confirms our assignment of the line shape to spin wave renormalization, and shows that the energy density in the magnetic system at long time delay is comparable to that absorbed directly by the spin system from the pump beam. The magnetic excitons absorb the majority of the laser energy, serving as a reservoir. The excess energy is transferred rapidly to quenching sites, whereupon it is dissipated over 100 ns to several microseconds via nonradiative processes [36]. In the steady state, a large number of these defect states will be excited, together with the steady-state phonon and spin wave distributions.

As a test for indirect energy transfer to the magnetic system via defects and phonons, we have performed two–color pump–probe experiments using our regenerative amplifier system to create high intensity pump pulses at 1.55 eV, well away from the X-M absorption feature. As described in Chapter 3, part of the

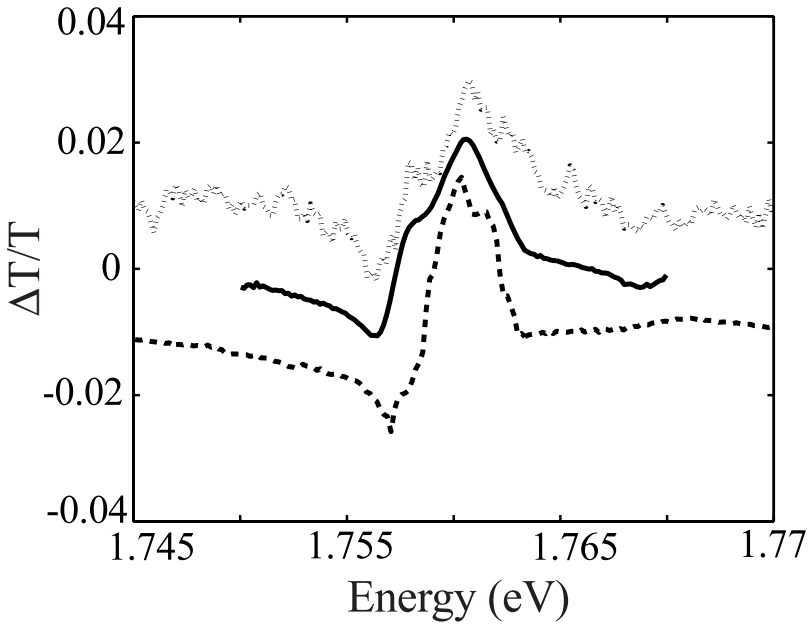

Figure IV.6: Comparison of the saturated pump-probe line shape with simulated and actual changes due to a thermalized energy density. Solid line: pump probe line shape, ×3; dotted line: thermal difference spectrum; dashed line: calculation using eqs. (IV.5) and (IV.3).

pulse energy was used to create a white-light continuum. We selected a 15 meV spectral range spanning the X-M absorption to probe it. For absorbed pulse energy densities ranging from 1-100 times those used in the degenerate pump-probe experiments, we observed no measurable change in the X-M absorption, indicating that the mechanisms for energy transfer from defect absorption into the magnetic system occur on time scales much longer than those of interest here. We conclude that the magnetic system behaves as a quasi–closed system at least during the first nanosecond, and that the dynamics which we observe are related to an intrinsic internal thermalization of the optically induced, nonequilibrium spin wave population.

IV.2.3 Temporal evolution of the spin wave population

We show the time evolution directly in Fig. (IV.7), where we plot the response at different wavelengths, keeping the laser center wavelength fixed. As in Fig. (IV.4), we have subtracted a small background component present at negative time delay, which is due to the steady state heating of the sample. When the probe frequency is outside the X-M line, ΔT/T exhibits prompt photo–induced absorption with a decay time longer than 500 ps, not shown here.

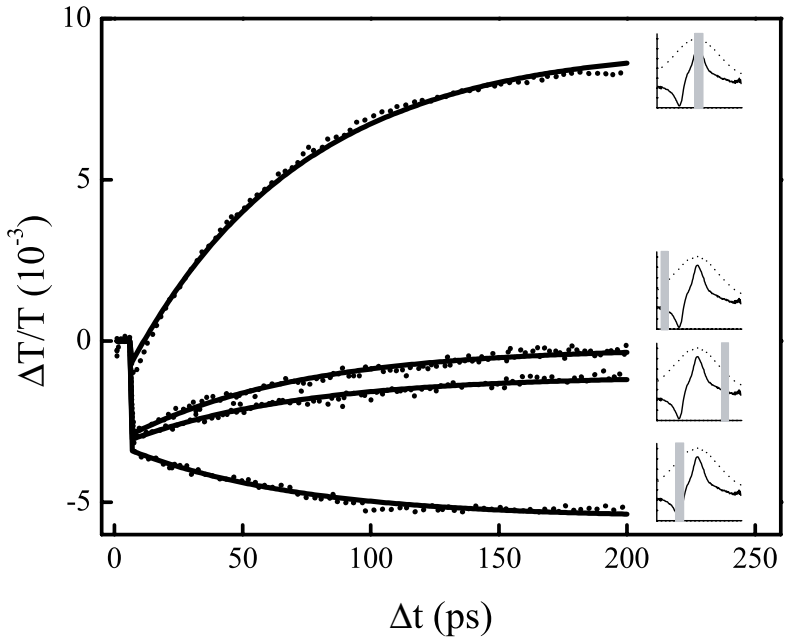

Figure IV.7: Time-resolved pump-probe signal at different wavelengths over energy bandwidth $\hbar\Delta\omega = 20$ meV. Probe energy ranges are indicated in the insets accompanying each curve, and correspond to the following average energies, listed from top to bottom: 1.764 eV, 1.751 eV, 1.771 eV, and 1.759 eV.

When the probe frequency is inside the X-M-line, ΔT/T exhibits both prompt photo–induced absorption and picosecond dynamics. The initial distribution of spin waves created by the laser is weighted heavily toward the zone boundary, because of the factor of $4\pi\mathbf{k}^2$ in the joint DOS integral given in Eq. (IV.5). If all spin waves contributed equally to the renormalization, as suggested by Eq. (IV.3), one would expect the spin wave renormalization and hence the X-M line shape to undergo an abrupt change at Δt=0, and remain unchanged during the internal thermalization of the spin wave system. This clearly is not the case: the initial population of $\mathbf{k} \approx \pi/a$ spin waves contributes little to the X-M renormalization line shape.

A phenomenological model for the dynamic response

Ignoring for the moment the underlying reason for the difference in optical response between zone center and zone boundary spin wave occupation, we can describe the dynamical response phenomenologically by dividing the occupied spin wave states into two different populations: those at the zone boundary (b)

and those at the zone center (c), with a boundary in reciprocal space chosen to reproduce the experiments. We assume that the decay of the initial nonequilibrium energy density $\mathcal{E}_b = \sum_{\mathbf{k}\in\mathbf{k}_b} n_{\mathbf{k}}\epsilon_{\mathbf{k}}$ into the thermalized energy density $\mathcal{E}_c = \sum_{\mathbf{k}\in\mathbf{k}_c} n_{\mathbf{k}}\epsilon_{\mathbf{k}}$ is governed by a single thermalization time, τ, and the decay over long times is set by an overall energy decay time, $\mathcal{T}$. Clearly, τ provides a measure of the interactions coupling the zone boundary spin waves to those at lower energy, both directly and via phonons. This process may be described by the following phenomenological rate equations:

$$\begin{aligned} \frac{d\mathcal{E}_b}{dt} &= -\mathcal{E}_b/\tau - \mathcal{E}_b/\mathcal{T}, \\ \frac{d\mathcal{E}_c}{dt} &= \mathcal{E}_b/\tau - \mathcal{E}_c/\mathcal{T}. \end{aligned} \tag{IV.6}$$

If we further assume that only the energy density due to zone center magnons $\mathcal{E}_c$ is involved in the renormalization line shape, we obtain the following equation for the time–dependent pump–probe signal, valid for each energy within the X-M absorption region:

$$\Delta\mathrm{T}/\mathrm{T} = a_1\Theta(t) + a_2[1-\exp(-t/\tau)]\exp(-t/\mathcal{T}), \tag{IV.7}$$

where a_1 and a_2 are prefactors which depend on the spectral region of interest. The step function $\Theta(t)$ is required to account for the photo–induced absorption, which we have taken to be time independent, consistent with experiments away from the X-M peak. The weak structure at early times, due to spin wave renormalization, is also included in a_1, though in principle this may be accounted for by an additional term. We have divided the 10 nm spectral range given by our laser spectrum into ten ranges of equal width, separated by 1 nm, and measured the temporal pump-probe response in each range. We then found the best global fits to the data of Eq. (IV.7), in which a_1 and a_2 are allowed to vary with probe wavelength, and $\tau = 40 \pm 10$ ps and $\mathcal{T} = 2 \pm 1$ ns are constrained to be the same for all ten wavelengths. The results for four of them are shown by the theoretical curves in Fig. (IV.7). This simple model captures very well the observed dynamics. What remains to be understood is the reason for the apparent absence of renormalization due to the increase in the population of short wavelength magnons.

Failure of spin wave theory for short wavelength spin waves?

The excitons and magnons are initially created on neighbouring sites and should interact moderately with each other, but the difference in their relative group velocities of ~10 Å/ps suggests that they are well separated after a picosecond or less, hence we do not believe that the observed dynamical change is associated with the decay of the X-M composite.

We can also rule out the argument that zone boundary magnons do not interact at all. The observation of spin wave *dynamics* at early times explicitly

requires interaction among the short wavelength spin waves, eventually leading to the thermalized magnon population which can be detected optically. Only in an ideal antiferromagnet, spin waves at the zone boundary are alleged to be well-defined quasiparticles with an infinite lifetime at T=0 K [51]. In a real system at finite temperatures, the most likely decay mechanism is thermal magnon–magnon scattering. Impurity-induced three magnon-splitting may also be involved [55], but the matrix element for this four–particle process should be much smaller (a two magnon decay is forbidden by spin conservation). The observed time scale of 40 ps is significantly too short for a thermal process involving first the generation of phonons with large momentum by magnons and then the phonons' subsequent decay. Albeit in a different material, no evidence was found for zone–edge magnon to mid–zone phonon decay [55], and it was suggested that magnons do not decay into phonons until the magnons scatter into magnetoelastic modes.

It is possible that the process of optical absorption in the presence of large **k** excitations is not described well by the particular approximation used here, but must include additional many–particle interactions. Such effects, however, would need to suppress the contribution of spin wave renormalization to the pump–probe line shape by an order of magnitude. In the past, this seemed unlikely in light of the fact that corrections to spin wave theory of order $1/(Sz)^2$ have already been calculated for the ideal 2D Heisenberg antiferromagnet and found to be very small [41]. Very recently it was pointed out theoretically how in a real, two–dimensional *anisotropic* system, $1/(Sz)^2$ corrections should play a more important role than in the isotropic case [64]. While similar calculations for three dimensions to the best of our knowledge do not exist, qualitative effects which contradict spin wave theory should in general be more pronounced for lower dimensions.

The simplest explanation for our result is that occupation at large **k** vectors produces weaker overall renormalization than those at the zone center. Such strong **k** dependence in spin wave interactions has long been indicated theoretically, and the variation of the interaction at short wavelengths may be so strong that the overall interaction effects cancel. Moreover, the notion that magnons are *not* well–defined quasiparticles at the Brillouin zone boundary was a key assumption in the recent description of photoemission data in $Sr_2CuO_2Cl_2$ [18]. It should not go unmentioned though that data obtained by means of neutron scattering so far has given no indication for a break–down of spin wave theory at short wavelengths. This seems to be true both for the three–dimensional compound investigated here [81], but also for materials of lower dimensionality [35, 95]. However, since error bars of these experiments are large, especially for large energies and momenta, interpretations beyond spin wave theory are still conceivable. Most importantly, while neutron scattering experiments can probe the magnon dispersion at large **k** values, they fail to provide information about magnon renormalization at high densities.

As a possible mechanism for such strong **k** dependence one might invoke two–magnon bound states. Those have been predicted—again only for the ferromagnetic case—to exist in three dimensions and particularly for large wave vectors [106]. It was also shown theoretically that two-particle bound states can have a strong influence on the energy renormalization [88]. Single magnons could scatter from the bound states, which might modify the magnon dispersion at the zone boundary to a point where magnons are no longer good quasiparticles [52]

IV.3 Conclusions

In summary, we have generated a macroscopic, nonequilibrium population of spin waves and observed its dynamics, using pulsed laser spectroscopy. At long times, the change in the absorption line shape is well understood by assuming that the photo-generated spin waves induce a renormalization of the spin wave dispersion relation. At short times, our results deviate sharply from the predictions of this model, indicating that short wavelength spin waves do not contribute to the renormalization of the line shape. The spin waves form a quasi-closed system over a 100 ps time scale. The evolution of this nonequilibrium population is consistent with a simple model of spin wave thermalization, and the thermalization time characterizes intrinsic spin wave coupling. The effects reported here provide us with information on elementary magnetic excitations that are inaccessible through conventional techniques, which typically probe only thermally occupied magnetic excitations.

The results are of particular interest considering the important role which magnetic elementary excitations play in the discussion of high-T_c superconductivity. Multi–magnon features, such as the two–magnon Raman excitation [34, 46, 95] and the phonon-bimagnon feature [30, 58–60] have attracted considerable interest recently. Successful modelling of these line shapes not only allows extracting the value of the exchange energy J, but more generally serves as a test for theories describing the physics of CuO–layers. While extended Heisenberg models (further neighbor interactions, or four-spin cyclic exchange [58]) describe the experimental observations reasonably well, discrepancies still remain [30]. Since the magnon-DOS is largest at the zone boundary, all the multi–magnon excitations strongly involve short wavelength magnons of the the type observed in this experiment.

Moreover, the technique demonstrated here may be used quite generally in magnetic insulators, and may be applied to a wide variety of optical magnetic excitations, including the aforementioned two–magnon excitations and the phonon–bimagnon feature in the undoped cuprates.

Chapter V

Optical properties of the charge-transfer gap in $Sr_2CuO_2Cl_2$

Understanding the wide variety of physical properties exhibited by strongly correlated electron systems is a major outstanding problem of solid state physics. Progress in the field is made difficult by the complexity of interactions between lattice, spin and charge degrees of freedom, introduced through strong correlation. One of many interesting phenomena is that of high–temperature superconductivity, which occurs as materials with a two–dimensional Cu–O plane are doped with free hole carriers.

To avoid the additional experimental and theoretical challenges introduced by doping and proceed in a systematic way, considerable effort is currently being made to better understand the undoped "parent" compounds of high-T_c superconductors. These undoped cuprates share the two–dimensional Cu–O layers with the superconductors, but lack free charge carriers. As a consequence, the optical spectra of the undoped compounds exhibit some well defined features, which vanish even with very weak doping. The dominant feature common to all materials and fundamental to strongly correlated systems in general is an *inter*–atomic electron transfer gap at about 1.5 to 2.0 eV. Considering its fundamental physical importance, surprisingly little attention has been given to the properties of this charge transfer gap and in particular to its coupling to lower energy degrees of freedom.

Even less is known about a number of *intra*–atomic transitions between Cu d states of different symmetry. These transitions were suggested as one possible coupling mechanism for Cooper–pairs [103]. Yet their energy, symmetry and oscillator strength even in the undoped cuprates remain controversial [31,57,76].

This chapter presents work on the linear and nonlinear optical properties of the two–dimensional charge transfer gap. In the first part, a comparative experimental and theoretical investigation of the linear optical properties in $Sr_2CuO_2Cl_2$ sheds light on the coupling between charge transfer gap excitations and lower energy degrees of freedom. Phonon mediated phenomena play an important role in our findings. On the other hand, our model suggests that magnetic degrees of freedom have no measurable influence on the exciton.

In the second section, we expand our measurements to include non–linear techniques, which allows us to identify a new, previously unobserved resonance at 0.7 eV. For the first time in these materials, we fully characterize the components of the complex nonlinear susceptibility tensor $\chi^{(3)}_{ijkl}(-3\omega;\omega,\omega,\omega)$ from 0.6 eV to 1.5 eV. We report a near–spherical symmetry of the electronic state(s) responsible for the resonance. First attempts to model the resonance theoretically are shown.

Finally, we present preliminary time–resolved experiment over a wide range of pump- and probe energies, above and below the charge transfer gap. Our findings underline the strong coupling between excitons and phonons found in linear spectroscopy.

V.1 Material characteristics of $Sr_2CuO_2Cl_2$

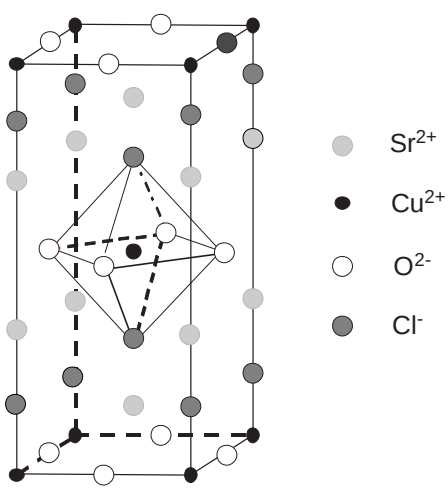

Figure V.1: Crystal structure of $Sr_2CuO_2Cl_2$

A special class of undoped cuprates are the one-layered oxyhalides such as $Sr_2CuO_2Cl_2$, $Ca_2CuO_2Cl_2$ and $Ca_2CuO_2F_2$ [69]. Rather than oxygen, they all contain different apical halogen atoms, but share the 2-dimensional Cu–O layers which form the structural and electronic basis for high-temperature superconductivity. Due to its very stable stoichiometry, $Sr_2CuO_2Cl_2$ is of great interest for experimentalists. The CuO_2 planes are unbuckled, and no orthorhombic distortion of the tetragonal symmetry is found down to at least 10 K [69]. Therefore, $Sr_2CuO_2Cl_2$ is regarded as an almost ideal realization of a two-dimensional, spin-1/2 Heisenberg antiferromagnet at half filling and serves as the test compound for any theory in the low-doping regime. The single hole per CuO_2 unit cell in the

ground state is located on the Cu site and exhibits a $3d_{x^2-y^2}$ symmetry.

The magnetic properties of $Sr_2CuO_2Cl_2$ are characterized by an exchange interaction energy J=125 meV [95] and a Néel temperature T_N ≈255 K. Even at T=350 K, it has been reported that the antiferromagnetic spin correlation length is still 250 Å [29], meaning that the tightly bound excitations studied here remain embedded in an antiferromagnetic background even at room temperature.

V.2 Linear absorption of the charge-transfer gap: Evidence of phonon mediated coupling between charge transfer and ligand field excitons in $Sr_2CuO_2Cl_2$

The broad excitonic feature at the charge-transfer (CT) gap, about half an electron volt wide, exhibits strong dependence on temperature and doping [17, 26, 99]. Despite the strong interest in insulating cuprates and the fundamental physical significance of the CT gap exciton, few attempts have been made to explain its structure and coupling to lower energy electronic or lattice degrees of freedom [26, 110]. Existing theories have little in common: they either invoke lattice- [26], magnetic- [17] or no lattice and no magnetic degrees of freedom at all, but include additional intra–atomic electronic states [89, 110].

In the first part of this chapter, we present an experimental and theoretical investigation of the linear absorption in $Sr_2CuO_2Cl_2$ and a new theory for the charge transfer excitation in the CuO_2 plane. We observe that the linear absorption spectrum over a wide range of energies and down to surprisingly low temperatures exhibits an exponential behaviour and can be fit by the Urbach formula. We present a model that accounts for phonon scattering to infinite order and allows us to explain accurately the data by assuming a phonon-mediated coupling of the charge transfer gap to lower energy electronic excitations.

V.2.1 Existing theories of the charge transfer gap

The lowest energy optically allowed electronic excitation in $Sr_2CuO_2Cl_2$ corresponds to the Cu $3d_{x^2-y^2}$ to O $2p\sigma$ transfer of a hole in the CuO_2 layer (described in detail below). This transition classifies the material as a charge–transfer insulator [109]. The optical absorption spectrum, shown in Fig. (V.2), consists mainly of a rather sharp peak near the band edge at about 2 eV [17].

A detailed analysis of the energy region below the band edge reveals a weak absorption feature with a very sharp, step–like onset at about 1.4 eV, two orders of magnitude smaller than the main CT structure. It is attributed to a Cu ligand field transition, which some authors believe to be of the $3d_{x^2-y^2} \rightarrow 3d_{xy}$

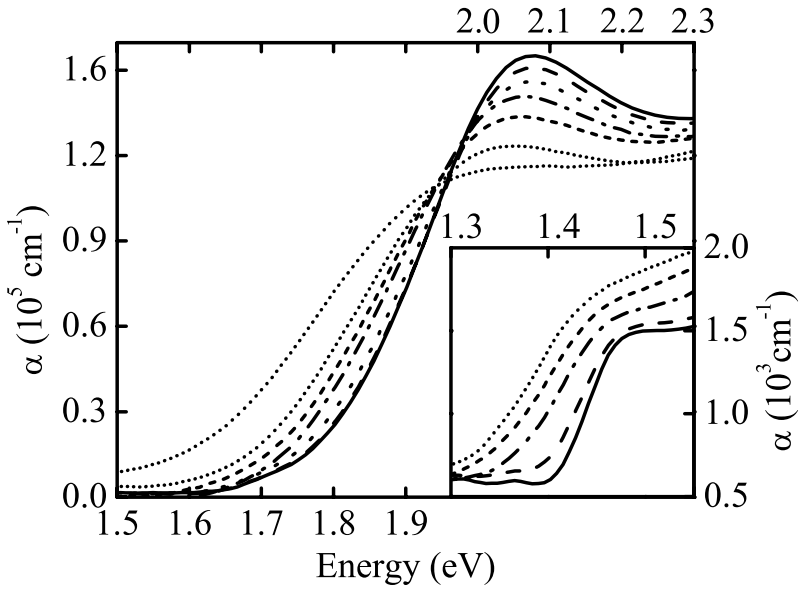

Figure V.2: Linear absorption at variable temperature near the charge transfer gap in $Sr_2CuO_2Cl_2$. T=15 K (solid line), 100 K (dashed) 150 K (dotted). Obtained from transmission data on a 95 nm thick sample. The inset details the weak onset of the absorption around 1.4 eV, recorded on a 300 μm thick sample

kind [76], while others place a $3d_{x^2-y^2} \rightarrow 3d_{3z^2-r^2}$ transition at this energy. Both should be optically forbidden, but acquire a small oscillator strength owing to a breaking of the crystal symmetry (see inset in Fig. V.2).

The dominant peak at the band edge is attributed to a bound excitonic state. An early, phenomenological model by Falck *et al.* attributes the peak to Frenkel excitons formed by electron and hole polarons [26]. Falck *et al.* observed the temperature shift and broadening of the excitonic peak in La_2CuO_4, a charge–transfer insulator isomorphic to $Sr_2CuO_2Cl_2$. By approximating the Coulomb interaction between electron and hole polarons with an attractive contact interaction they derived a simple expression for the absorption coefficient. While without interaction the interband contribution to the absorption consists just of the density of states, the short range contact interaction leads to an increased absorption near the band edge. Falck's model further accounts for the shift of the band edge and the finite lifetime of the exciton by assuming that its decay rate is the sum of the individual polaron decay rates. With four parameters, Falck *et al.* are able to describe their measured linear absorption in La_2CuO_4 well [26].

A microscopic model for the exciton, which however lacks coupling to phonons, was introduced by Zhang and Ng [110]. As indicated in Fig. (V.3), the exciton

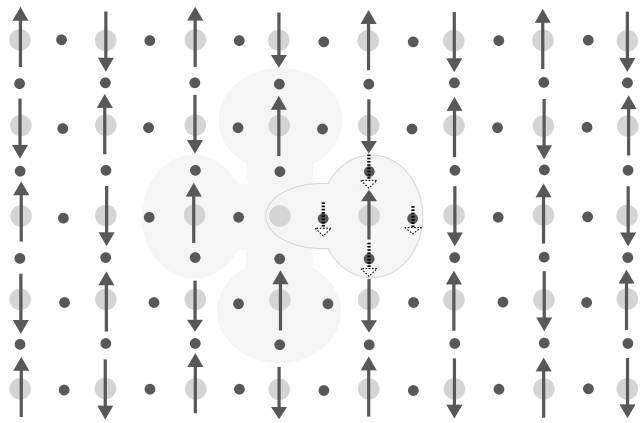

Figure V.3: Illustration of the charge-transfer exciton structure in Ref. [110]: A quasihole is transferred from the Cu (large, shaded circle) $3d_{x^2-y^2}$ to the O (small, solid circle) $2p\sigma$ state, and through Cu–O hybridization shared with surrounding oxygen atoms (broken arrows). Together with the electron on the Cu site, this object forms the exciton (outlined). Rotation symmetry (shaded) of the crystal leads to four exciton eigenstates.

forms through the transition of a quasihole from the Cu $3d_{x^2-y^2}$ to the O $2p\sigma$ state (the nonbonding O 2 $p\pi$ are not included in this model). Due to the strong Cu–O hybridization, the hole in the O $2p\sigma$ state is delocalized among the other oxygen atoms surrounding the neighboring copper site (illustrated by the small broken arrows on the oxygen sites in Fig. V.3). The attractive Coulomb potential between electron and hole is large, since screening charge carriers are missing in this insulating compound. Finally, the four–fold crystal symmetry in the plane has to be accounted for, which results in four exciton eigenstates with well defined local s, d, p_1 and p_2 symmetry. Of those, only p_1 and p_2 are optically allowed. For $\mathbf{k}$=0, these two states are degenerate and form the charge transfer gap exciton which is prominently observable in the linear absorption spectrum Fig. (V.4).

Zhang's model correctly predicts a large bandwidth of about 1.2 eV [69, 102] for the center of mass motion of the exciton in $Sr_2CuO_2Cl_2$. This is remarkable compared to the much smaller dispersion width 0.35 eV for a single quasihole in the same material [104], yet can be understood by the fact that the movement of the exciton from one site to another—in contrast to the movement of a hole by itself—does not disturb the antiferromagnetic order of the background.

Finally, Choi *et al.*, without mentioning it explicitly, use Zhang's model and

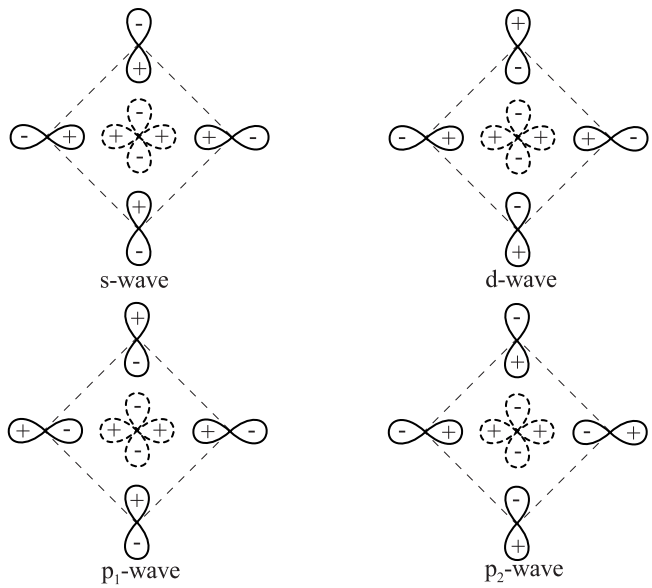

Figure V.4: Symmetries of the exciton wave functions after Ref. [110]: The center d wave represents the Cu^+ vacancy. For the oxygen sites, the $2p_{x,y}$ hole wave functions are shown. Not shown are spin degrees of freedom, which are the same as in Fig. V.3

attribute the shift and broadening of the exciton to a "weakening of the antiferromagnetic background with increasing temperature" [17]. The model fails, however, to provide further quantitative insight.

V.2.2 Linear absorption at the long wavelength tail and Urbach behaviour

As evident from Fig. (V.5), the excitonic peak shows a strong temperature dependence. With increasing temperature the width—measured as the half width at half maximum—increases from 180 meV at 15 K to 270 meV at 350 K.

The absorption maximum at $\hbar\omega_{max}$ exhibits a red shift of about 80 meV in this temperature range. Falck's model cannot reproduce such a strong shift for any physical choice of parameters [1]. The temperature dependence of the excitonic peak is shown in Fig. (V.5). Both the shift towards lower energies and the broadening can be fit by a Bose–Einstein occupation function with a single oscillator, following Ref. [26]. The energy of this oscillator, $\hbar\omega_0 \approx$45 meV agrees well with

[1] As we will shown below, this failure might be due to the fact that Falck's model includes only single–phonon processes in lowest order

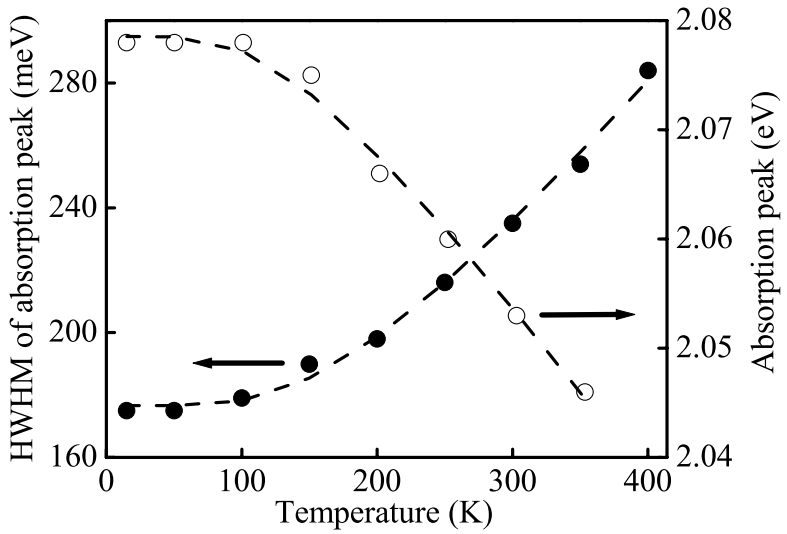

Figure V.5: Shift and broadening of the charge transfer exciton peak in $Sr_2CuO_2Cl_2$. Filled circles plot the half width at half maximum (HWHM) of the peak (left axis), open circles its energy(right axis). The dashed lines represent best fits to a Bose-Einstein occupation function with a single oscillator. The fit gives $\hbar\omega_0$=45 meV as the energy of this oscillator

previously identified longitudinal optical (LO) phonons of $\hbar\omega_0$=50 meV [94], yet is well below the characteristic *magnetic* energy scale of J=125 meV in $Sr_2CuO_2Cl_2$. Despite the poor fit results we obtained using Falck's phenomenological description, this experimental evidence gives a first hint that coupling of the charge transfer exciton to phonons rather than to magnetic excitations might be at the origin of its red shift and broadening [26].

Coupling to phonons as a reason for the temperature dependence is further supported by a careful analysis of the line shape of the low energy side of the CT excitation. Our absorption measurements are plotted on a logarithmic scale in Fig. (V.6), and display an exponential behaviour over a wide range of energies and temperatures.

This characteristic behaviour has been reported in a variety of insulators and semiconductors—though not in cuprates—and is called the Urbach rule [54,100]. A number of theories have been developed to explain the exponential absorption tail at long wavelengths, yet there is still no single accepted explanation. Among the mechanisms proposed are interaction of the exciton with phonon

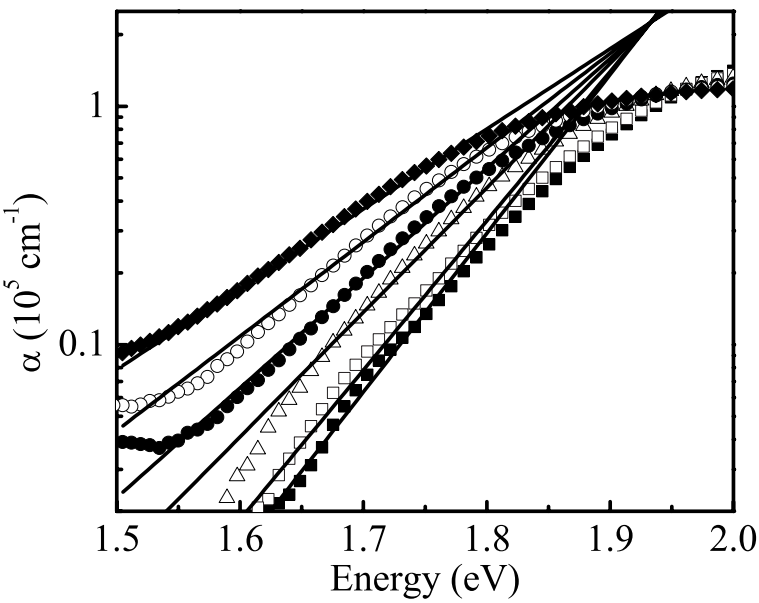

Figure V.6: Linear absorption to of $Sr_2CuO_2Cl_2$, plotted on a semi-logarithmic scale. The lines represent global best fits to the Urbach-formula (V.2). Solid squares T=15 K, open squares T=150 K, open triangles T=250 K, solid circles T=300 K, open circles T=350 K, solid diamonds T=400 K.

modes through quadratic interaction [83, 96], creation of in–gap states through microfields caused by disorder and phonons [22], and thermal fluctuations of the the band gap energy [90]. Despite the large number of models used to explain Urbach's empirical results, all existing theories to our knowledge suggest that *interaction of electrons or excitons with phonons* lies at the heart of the mechanism.

In the most general form, Urbach's rule can be written as:

$$\alpha(\omega, T) = \alpha_0 \exp \frac{\sigma(T)(E - E_0)}{k_B T}; \tag{V.1}$$

$$\sigma(T) = \sigma_0 \frac{2k_B T}{\hbar\omega_0} \tanh \frac{\hbar\omega_0}{2k_B T}. \tag{V.2}$$

E_0 and α_0 are temperature independent parameters, and $\hbar\omega_0$ is the energy of the phonon to which the exciton couples. From the global best fits we obtain $\hbar\omega_0$=45 meV in excellent agreement with the peak shift and -broadening, and E_0=1.93 eV. The latter number is smaller than the energy of the absorption

maximum for all temperatures observed, which suggests that the CT exciton exhibits a localized character [54].

The parameter σ_0 is inversely proportional to the coupling strength between phonons and excitons which is responsible for the Urbach behaviour. We find σ_0=0.35, which implies a very strong coupling (see table V.1). It is very surpris-

substance	σ_0	$\hbar\omega_0(meV)$	ΔT (°K)
ZnSe	1.2	25	77 to 300
CdSe	2.6	21	77 to 300
CdS	2.45	7.5	4 to 300
NaCl	0.76	10	10 to 570

Table V.1: Steepness parameter σ_0, phonon energy $\hbar\omega_0$ and temperature range for which the Urbach rule has been observed for a selection of materials ([54] and references therein).

ing that an Urbach–tail can be observed at a temperatures of 15 K, where the occupation probability of LO–phonons with $\hbar\omega_0$=45 meV is $N_0 \approx 2\times10^{-16}$ and hence the absorption of thermal phonons is negligible. It is generally assumed that the Urbach rule only applies at temperatures above the Debye–temperature of a material [54].

V.2.3 Theory: phonon coupling to ligand field excitations

To the best of our knowledge, the model of Falck *et al.* [26] is the only one in the literature which describes the temperature dependence of the charge transfer exciton. Yet the model has significant shortcomings:

- Our experimental results show excellent agreement with Urbach's law down to very low temperatures, which is in striking contradiction to the prediction of Ref. [26]. Falck's model by construction always produces a Lorentzian rather than an exponential tail.
- The coupling constant obtained in Ref. [26] is α=10.8.[2] This value is very large compared to normal semiconductors (where it is well below 1.0) and even other materials with a strong electron–phonon coupling. For such a high coupling constant the one–phonon approximation facilitated by Falck *et al.* is clearly no longer valid.

Since experimental evidence points to a strong coupling between the exciton and LO–phonons as the reason for the strong temperature dependence, we[3] propose

[2] The coupling constant used in Ref. [26] a factor of 2 smaller the standard convention [62]

[3] The theory was developed in a collaborative effort between R. Lövenich, D. S. Chemla and the author

a more advanced model, taking into account many–phonon processes. The approach was inspired by results obtained for conventional semiconductors [56], where Urbach tails are found at high temperatures.
The model Hamiltonian:

$$H = H_0 + V \tag{V.3}$$

$$H_0 = \sum_{jn\mathbf{k}} E^j_{n,\mathbf{k}}\, a^{j\dagger}_{n,\mathbf{k}}\, a^j_{n,\mathbf{k}} + \hbar\omega_0 \sum_{\mathbf{q}} b^\dagger_{\mathbf{q}}\, b_{\mathbf{q}} \tag{V.4}$$

$$V = \sum_{jj'} \sum_{nm\mathbf{q}} M^{jj'}_{nm,\mathbf{q}}\, a^{j\dagger}_{n,\mathbf{k}+\mathbf{q}}\, a^{j'}_{m,\mathbf{k}} \left[b_{\mathbf{q}} + b^\dagger_{-\mathbf{q}} \right] \tag{V.5}$$

is written in an exciton basis, where $a^{j\dagger}_{n,\mathbf{k}}$ is the creation operator for an exciton of type j, internal quantum number n and center of mass momentum $\mathbf{k}$. In the case of the (j=CT) charge transfer exciton we account for a bound state (n=0), and for the unbound exciton electron–hole continuum (n >0). The pair $(n, \mathbf{k})$ can then be transformed to the pair of electron and hole momentum, which is more suited to describe the free electron–hole pair. In the case of the ligand field excitation (j=LF) we consider continuum states only. The reason to include the two different kinds of excitons will become evident later. The operators $b_{\mathbf{q}}$ and $b^\dagger_{\mathbf{q}}$ respectively describe the annihilation and creation of a dispersionless LO–phonon of frequency ω_0.

The absorption is given by the imaginary part of the retarded Green's function

$$\varepsilon_2(\omega) \propto \mathrm{Im}\left\{ \sum_{j=\mathrm{CT},n\mathbf{k}} G^j(n\mathbf{k}=0;\omega) \right\}, \tag{V.6}$$

where the summation includes only the optically dipole active charge transfer exciton of p symmetry.

Since the excitation starts from a ground state characterized by empty hole and electron states, the retarded Green's function equals the time–ordered one, for which an expansion in the electron–phonon coupling exists:

$$G^j(n\mathbf{k};t) = -\frac{i}{\hbar}\theta(t) \sum_{\nu=0}^{\infty} W^j_\nu(n\mathbf{k};t) \tag{V.7}$$

$$W^j_\nu(n\mathbf{k};t) = \frac{(-i)^{2\nu}}{\hbar^{2\nu}(2\nu)!} \int_0^t dt_1 \ldots \int_0^t dt_{2\nu} \left\langle T \bar{a}^j_{n,k}(t)\, \bar{V}(t_1) \ldots \bar{V}(t_{2\nu}) \bar{a}^{j\dagger}_{n,k}(0) \right\rangle, \tag{V.8}$$

with the time-ordering operator T. The unperturbed Green's function is given by $G^j_0(n\mathbf{k};t) = -i/\hbar\,\theta(t)\,\exp(-iE^j_{n,\mathbf{k}}\,t/\hbar)$. The first order term in (V.7) would

give rise to one–phonon processes. However, it is possible to account for multi-phonon processes by re–summing the expansion eq. (V.7) in form of an exponential, leading to the cumulant expansion or linked–cluster theory. We write

$$G^j(n\mathbf{k};t) = G_0^j(n\mathbf{k};t)\,\exp\left(\sum_{\nu=1}^{\infty} F_\nu^j(n\mathbf{k};t)\right), \tag{V.9}$$

where F_ν denotes a contribution which contains the 2ν-th power of the coupling matrix–element. Comparing the different powers of the expansions (V.7) and (V.9), the following relations hold:

$$F_1^j(n\mathbf{k};t) = e^{iE^j_{n,\mathbf{k}}\,t/\hbar}\,W_1^j(n\mathbf{k};t) \tag{V.10}$$

$$F_2^j(n\mathbf{k};t) = e^{iE^j_{n,\mathbf{k}}\,t/\hbar}W_2^j(n\mathbf{k};t) - \frac{1}{2!}\,F_1^{j\,2}(n\mathbf{k};t)\ . \tag{V.11}$$

The advantage of this re-summation is that F_1 already includes independent phonon scattering to infinite order. Thus as long as these scattering events are independent of each other, the first term in the cumulant expansion F_1 accounts for all contributions in contrast to the expansion (V.7). Similarly F_2 describes all electron–phonon interactions involving two phonons simultaneously, etc. The cumulant expansion (V.9) is expected to converge much faster than (V.7) and to be appropriate for low and intermediate coupling constants. Up to now we restricted ourselves to the lowest order only, which means that we treat the fields induced by the lattice distortions classically.

The time–integrations in (V.8) can be performed analytically, which yields:

$$\begin{aligned} F_1^j(n\mathbf{k}=0;t) = & \sum_{h'm\mathbf{q}} \left|M^{jj'}_{nm,\mathbf{q}}\right|^2 \Big\{(N_0+1)\bar{f}(E^{j'}_{m,\mathbf{q}} - E^j_{n,0} + \hbar\omega_0, t) \\ & + N_0\,\bar{f}(E^{j'}_{m,\mathbf{q}} - E^j_{n,0} - \hbar\omega_0, t)\Big\}\,, \end{aligned} \tag{V.12}$$

where the time dependence is described by the function

$$\bar{f}(\varepsilon,t) = \frac{1}{\varepsilon^2}\,(1 - e^{-i\varepsilon t/\hbar} - \frac{i\varepsilon t}{\hbar})\ . \tag{V.13}$$

This function is regular for all values of ε and has its maximum value at ε=0, which in eq. (V.12) corresponds to $E^{j'}_{m,\mathbf{q}} = E^j_{n,0} \pm \hbar\omega_0$, i.e. the absorption and emission of LO-phonons in the $(j', m\mathbf{q}) \leftrightarrow (j,n)$ transition.

In order to keep our model simple, we neglect the $\mathbf{q}$ dependence of the coupling matrix elements $M^{jj'}_{nm,\mathbf{q}}$ as well as the dependence on the relative momentum if $m > 0$ or $n > 0$ (which describes the electron–hole continuum). This means we have to consider the following five scattering processes:

M_{xx} Scattering from the CT-exciton into its center of mass continuum;

M_{xc} Scattering from the CT-exciton into its own electron–hole continuum;

M_{cc} Scattering within the CT electron–hole continuum;

M_{xd} Scattering from the CT-exciton into the LF exciton band;

M_{cd} Scattering from the CT electron–hole continuum into the LF exciton band;

Since the matrix–elements do not depend on momentum variables any more, the summations over momentum variables in (V.12) can be transformed into energy integrals with the density of states into which the CT-exciton is scattered:

$$\begin{aligned} F_1(n=\{x,c\},0;t) &= \int d\varepsilon \sum_{m=x,c,d} M_{nm}\, z_m(\varepsilon) \\ &\quad \times \Big\{ (N_0+1)\bar{f}(\varepsilon - E_{n,0} + \hbar\omega_0, t) \\ &\qquad + N_0\, \bar{f}(\varepsilon - E_{n,0} - \hbar\omega_0, t) \Big\} . \end{aligned} \tag{V.14}$$

The densities of states are defined as:

$$z_x(\varepsilon) = \frac{1}{N}\sum_{\mathbf{q}} \delta(\varepsilon - E_{x,\mathbf{q}}) \quad \text{and} \tag{V.15}$$

$$z_c(\varepsilon) = \frac{1}{N^2}\sum_{\mathbf{qk}} \delta(\varepsilon - E_{\mathbf{k},\mathbf{q}}) . \tag{V.16}$$

We model the energy dispersion of the exciton by a two–dimensional tight binding dispersion $E_{x,\mathbf{q}} = \frac{B}{4}\cdot(2-\cos q_x - \cos q_y)$ with a bandwidth of B=1.2 eV as found by EELS experiments [102]. For the electron–hole continuum the bandwidth of the relative motion is assumed to be 0.6 eV, also with a 2d tight binding dispersion. We then solve eq. (V.6) for three cases of physical interest. In case (1) we consider a situation where phonon scattering occurs only within the charge transfer states, i.e., CT bound-exciton and its own electron–hole continuum. The transition into other exciton bands is not allowed; therefore $M_{xd} \equiv 0$ and $M_{cd} \equiv 0$. In the other cases (2a, 2b) we *do* allow phonon scattering of the charge transfer exciton with other, lower energy excitonic states (LF exciton band). Then, we explore the generality of our assumptions by considering two slightly different LF exciton bandwidths.

Phonon scattering within charge transfer band only

The results for case (1) with the contribution of the CT-exciton only ($n = x$ in (V.9) are shown in Fig. (V.7) and are in obvious contradiction with experiment. Clearly the coupling to LO–phonons has the desired effect of broadening the CT exciton line with increasing temperature. The line becomes asymmetric with a longer tail at the high energy side. On the low energy side, the spectrum exhibits

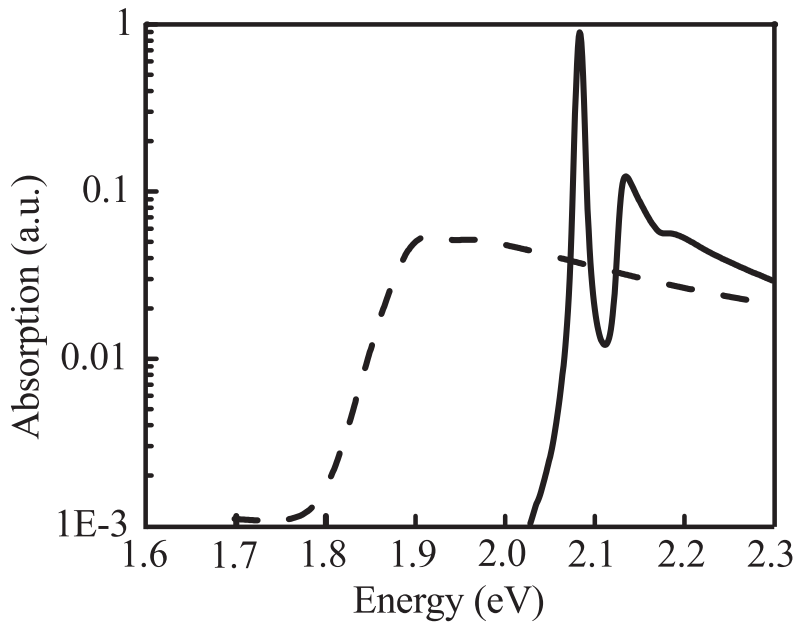

Figure V.7: Calculated absorption spectrum for the contribution of the CT exciton only (scattering only into the exciton and e-h continuum). Solid line T=15 K, dashed line T=300 K. The parameters are the same as for the final calculations, except that the coupling constants are twice as big and the inhomogeneous broadening was only 2 meV.

an Urbach tail, but the width is extremely small, especially at low temperatures. This is true even for very high coupling constants. Attempts to account for the large width at low temperatures by assuming a much stronger homogeneous or inhomogeneous broadening would lead to a Lorentzian or Gaussian profile of the lower energy side of the spectrum.

Inspection of Eq. (V.14) reveals why the LO–phonon coupling has only little effect at low temperatures. At zero temperature only the LO–phonon *emission* term proportional to $(N_0 + 1) \to 1$ contributes. The CT-exciton densities of states $z_x(\varepsilon)$ and $z_c(\varepsilon)$ start at the bound exciton energy and its band edge energy, respectively. The function $\bar{f}(\varepsilon - E_{n,0} + \hbar\omega_0, t)$ however has its maximum one phonon-energy below the exciton energy and decays roughly with $1/\varepsilon$. This implies that the contribution of F_1 is very small. Although the coupling to LO–phonons gives rise to the correct profile, the effect is too small to explain the experimental data. Physically, this means that at low temperatures, the phonon occupation is too low to allow sufficient broadening of the exciton line.

Phonon mediated coupling to ligand field excitations

From the above discussion the shortcoming of our model in case (1) is evident. Since experimentally we observe the Urbach law even at very low temperatures, phonon emission transitions still govern the interaction with the lattice and their contribution is dominant as implied by eq. (V.14). Therefore, for a broad CT-exciton peak with a flat exponential tail to occur there must be real states available below the exciton energy and the CT-exciton has to be able to couple to these states by phonons. Only then can LO–phonon scattering be strong even at zero temperature.

Both our own data and the experiments in Ref. [17, 76] show that such a continuum below the exciton exists. It starts at about 1.4 eV and was previously assigned to a Cu *dd* ligand field transition character [31, 76]. While optically forbidden, this excitation can couple to the charge transfer excitons via phonons. It should be noted that the symmetry of this excitation—which remains controversial [31, 57, 76]—is not relevant for our discussion.

We therefore expanded our model to include the continuum of ligand field excitations. Since little is known about the bandwidth of these excitations, we have considered two different values for this parameter. In case (2a) we assumed that the LF bandwidth is the same as that of the charge transfer electron–hole continuum. Furthermore, the CT exciton binding energy was fitted to be 240 meV, $|M_{nm}|^2 = 20(\hbar\omega_0)^2$ was used for all coupling constants. In addition to the broadening due to the LO–phonons we include an inhomogeneous broadening of Γ_I=60 meV which accounts for sample imperfections. Homogeneous broadening must be included, yet has to be small compared to Γ_I, since otherwise a Lorentzian profile would become apparent for energies far below the CT exciton energy. Such a Lorentzian line shape is not observed experimentally. In order to minimize the number of adjustable parameters in our model, we have therefore decided not to include a homogeneous broadening in our model. Finally, to obtain best fit results we find that the spectral weight of the electron–hole continuum needs to be twice that of the exciton.

Figure (V.8) shows the results of the expanded model on a linear and logarithmic scale. They are in excellent agreement with the experimental data, shown by the dots. The broadening and the shift of the CT exciton are reproduced correctly and even the decrease in oscillator strength is well described.

It may be argued that the bandwidth of the ligand field exciton should be smaller than that of the charge transfer exciton. In order to investigate this eventuality, we have considered in case (2b) the effects of a narrower LF exciton bandwidth, only 1 eV, while maintaining the flat density of states suggested by the the absorption spectrum at 1.4 eV. We find that we can obtain the same excellent fit results as in case (2a), but now need two independent coupling constants. One constant governs the coupling to the LF excitons, and a second one interactions

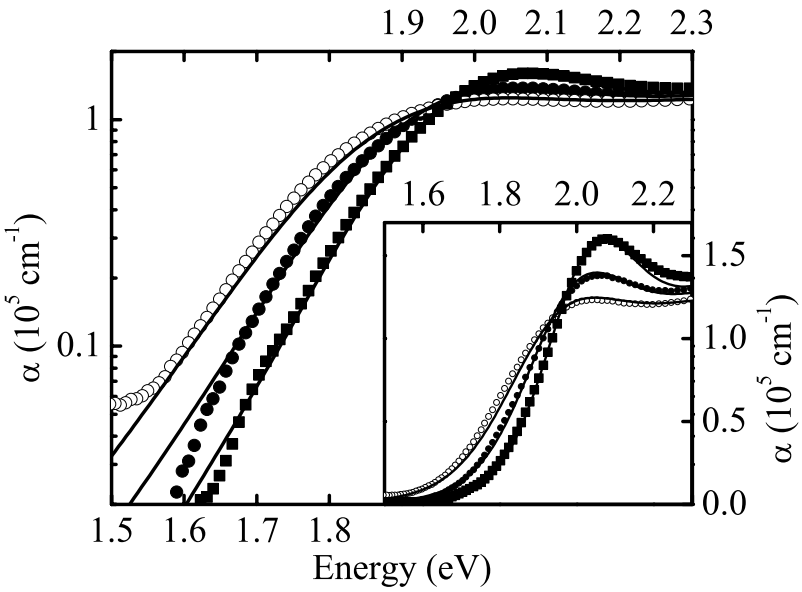

Figure V.8: Linear absorption data and theory, plotted on both a semilogarithmic (main diagram) and linear (inset) scale. Only three temperatures are shown for clarity. Squares T=15 K, closed circles T=250 K, open circles T=350 K (data). Calculated curved at the respective temperatures are shown as solid lines

within the CT exciton manifold.

Interestingly, numerical integration and fitting shows that the temperature shift of the CT exciton is governed by the coupling to its own continuum, whereas the broadening is mostly sensitive to the coupling to ligand field excitons.

Although the model formally exhibits a number of fit parameters, many (phonon energy, CT exciton bandwidth, onset of the LF absorption etc.), are set by experimental constraints. Furthermore, we have limited the number of free parameters by restricting the number of phonon coupling constants to one (case 2a) and two (case 2). As a consequence, only a small number of adjustable parameters remain: the phonon coupling constant, the instantaneous broadening, the relative spectral weight of the CT exciton and its continuum, the CT exciton binding energy and an overall scaling factor. With these variables, we are able to obtain excellent fit results over a wide energy, absorption and temperature range.

Our results indicate that the coupling constants thus obtained are indeed large.

Due to the different models they cannot be directly compared to the results of Falck *et al.* It is straightforward to verify if accounting for one–phonon processes only would be sufficient: if the **q**-dependence of the matrix elements is neglected, one could calculate F_2 . This has not yet been done.

Another theory often used to describe localized electronic excitations coupled to LO–phonons is Toyozawa's [97]. In the strong coupling regime it predicts a self-trapping of excitons, i. e. due to the phonon cloud surrounding the exciton its effective mass becomes extremely large. Since we have shown on very general physical grounds that the low temperature Urbach behavior requires the coupling of the CT-exciton to a continuum of states below the exciton energy, we expect that a model based on Toyozawa's theory would give rise to results qualitatively similar to ours.

V.2.4 Conclusions

In conclusion, we have presented for the first time linear absorption measurements across the charge transfer gap in $Sr_2CuO_2Cl_2$. Processing of samples with a thickness < 100 nm has enabled us for the first time to obtain the transmission spectrum directly, without having to rely on Kramers-Kronig transformations as in previous works [17, 26]. The absorption spectrum exhibits a broadening and a shift of the charge transfer gap exciton and, importantly, an Urbach behavior down to very low temperatures. This behavior is not explained by current theories. Our model, motivated by the observation of strong electron–phonon coupling and based on a cumulant expansion, provides an excellent fit for the measured absorption over a wide range of temperatures, photon energies and absorption values. To obtain these good fits, we need to allow the charge transfer gap exciton to couple by LO–phonons to a continuum of states with lower energy. We propose the Cu *dd* continuum of ligand field excitons, which is revealed in the absorption spectra owing to a weak, crystal field induced symmetry breaking. Our model does not rely on magnetic degrees of freedom. As a consequence, we would like to suggest that magnetism can be eliminated as a significant contributor in the temperature dependence of the charge transfer absorption edge in this material.

V.3 Coherent nonlinear optics at the CT gap

In the previous section we used *linear* optical measurements to extract information about the coupling between different electronic and lattice degrees of freedom. While being a powerful tool to investigate the location of optically active excitations and their line widths, we showed in chapter III that *nonlinear* techniques must be employed to study optical excitations between same parity states. In the following section, nonlinear experiments will be presented which probe optically dipole active and dipole forbidden electronic excitations at and near the charge transfer gap.

Apart from the optically active charge transfer excitation itself, a variety of optical dipole allowed and forbidden excitations exist the vicinity of the charge transfer gap. Their assignment remains in many cases subject to debate. Since the low–energy structure of the gap and its evolution with doping [99] is of great interest for theories of high-T_c superconductivity, efforts focus on how to identify the excitations in the undoped compounds. Optically inactive transitions are the four intra–atomic Cu $d-d$ excitations from the $3d_{x^2-y^2}$ hole ground state into configurations with $3d_{3z^2-r^2}$, $3d_{xy}$ and $3d_{xz,yz}$ symmetry. Furthermore, the models by Zhang [110] and Simon [89] predict parity forbidden inter–atomic transitions, which involve the O $2p\sigma$ as well as O $2p\pi$ states, respectively.

Nonlinear techniques which can probe the optically forbidden excitations have attracted considerable interest. Most importantly, conventional high–energy Raman spectroscopy [57], and more recently resonant X-ray Raman spectroscopy [31] have helped to identify the Cu $3d_{xz,yz}$ and $3d_{xy}$ states. In addition, Raman spectroscopy has helped to clarify the origin of the absorption feature at 0.5 eV. This peak is common to all insulating cuprates and now widely believed to be due to a transition involving two magnons and a phonon [58, 76]. Despite its advantage as a nonlinear technique, conventional Raman spectroscopy is not without challenges. Most notably are the high background luminescence and the strong elastic peak. Coherent nonlinear optical measurements probe the same susceptibility tensor $\chi^{(3)_{ijkl}}$, yet do not suffer from the high background problems. They have been extensively used in semiconductors and polymers [15,16]. But only a few experiments in strongly correlated systems have been reported, mostly with an eye towards technical applications of large susceptibilities. [48,70]

V.3.1 Resonant enhancement of $|\chi^{(3)}_{xxxx}|$

In a first step, we characterized the absolute value of the third–order susceptibility over a wide frequency range. Absolute measurements of nonlinear susceptibilities are generally difficult, since they require very accurate knowledge of all laser pulse and beam parameters. This problem can be circumvented by performing a measurement relative to a well characterized material, such as quartz. Quartz exhibits a flat absorption without resonances over the wavelength range of interest to us, and its nonlinear susceptibility has been established with great care by various authors ([37] and references therein).

In our experiment, we measured the absolute third harmonic intensity $I_{3\omega} \propto |\chi^{(3)}_{xxxx}|^2$ of $Sr_2CuO_2Cl_2$, and compared the results to a thin quartz plate. The quartz plate used for reference measurements had a thickness of d=150 μm, and was cut with the c-axis normal to the crystal surface. From the literature, $\chi^{(3)}_{xxxx}$(quartz)=(2.96±1.5)×10^{-14} esu [37][4]. Our experimental setup is

[4]For the discussion $\chi^{(3)}$, we will use the more common electrostatic units esu [cm^2statvolt^2]. To obtain $\chi^{(3)}$ in SI units [m^2V^2], one needs to divide by a factor of $4\pi c^{-2}\times 10^{12}$, with

shown in Fig. V.9. For the $|\chi^{(3)}_{xxxx}|$ measurement, we switched between the $Sr_2CuO_2Cl_2$ sample, held at room temperature (but under vacuum to avoid sample degradation due to moisture in the air) and the quartz plate.

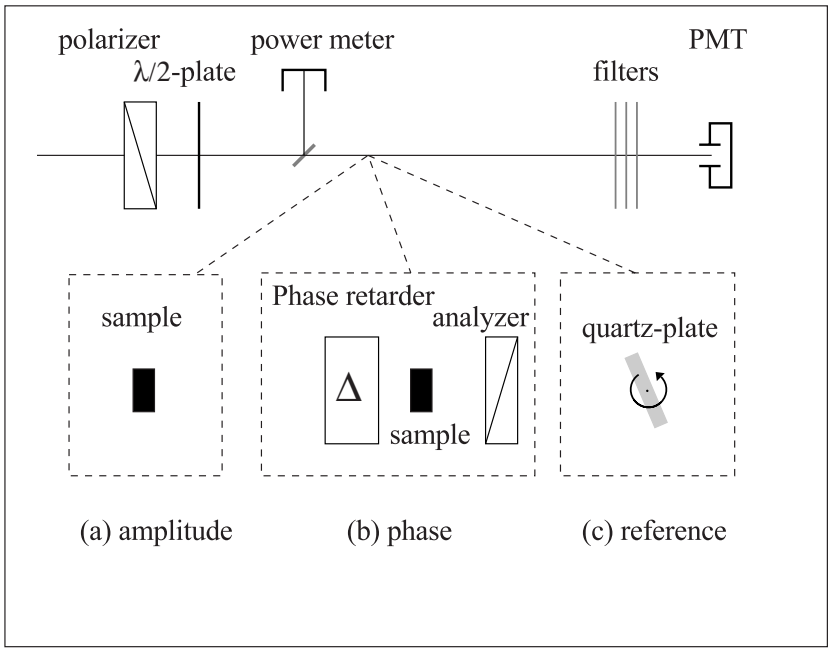

Figure V.9: Setup for phase- and amplitude measurement. Filters are used to block radiation at ω and 2ω. PMT: various photomultiplier tubes, depending on the frequency range of interest. For the $|\chi^{(3)}_{xxxx}|$ measurement, we switched between the sample (a) and a quartz plate (c) on a motorized rotation stage record the Maker fringes. For the phase measurement (b), the phase retarder Δ, allowed to continuously tune the ellipticity of the input electrical field $\mathbf{E} = \hat{x}\frac{E}{\sqrt{2}} + \hat{y}E\frac{E}{\sqrt{2}}e^{i\Delta}$. The analyzer transmits either I_x or I_y. A mirror on a kinematic mount directs the incoming beam to a power meter.

If higher harmonics are generated in a sample which is thick compared to the wavelength of light, a phase mismatch between the free wave $(\omega, \mathbf{k}_\omega)$ and the forced wave at $(3\omega, \mathbf{k}_{3\omega})$ can occur. As a result, the intensity $I_{3\omega}$ depends sensitively on the angle between $\mathbf{k}_\omega$ and $\mathbf{k}_{3\omega}$. This phase matching angle is given by the angle of incidence, and the light intensity at 3ω shows interference fringes as a function of the this angle ("Maker fringes" [63]). While this is not a concern for our l≈100 nm thick $Sr_2CuO_2Cl_2$ sample, the Maker fringes need to be considered for the d=150 μm thick quartz plate. We therefore mounted

c=2.998·10^{10}cm s^{-1}.

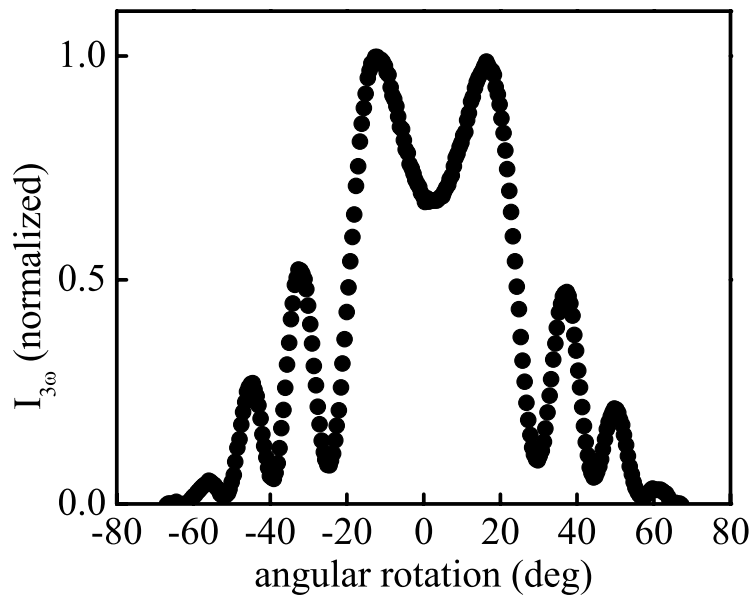

Figure V.10: Maker fringes on a d=150 μm thick, c-axis oriented SiO_2 plate. ω=1.5 eV.

the reference crystal on a motorized rotation stage. An example for the Maker fringes thus obtained is shown in Fig. (V.10).

For the quartz plate, the third harmonic intensity is given by [113]:

$$I_{3\omega}^{quartz} = \gamma(\chi_{xxxx}^{(3),quartz})^2 \, I_\omega^3 \, \frac{\sin^2\left(\frac{\Delta k d}{2}\right)}{\left(\frac{\Delta k}{2}\right)}. \tag{V.17}$$

I_ω^3 is the third power of the input intensity, γ a numerical pre–factor irrelevant for our relative measurement of $\chi^{(3)_{ijkl}}$ and Δk=$k_{3\omega} - 3k_\omega$ the phase mismatch. The $\sin^2\left(\frac{\Delta k d}{2}\right)$ term is the one responsible for the Maker fringes.

In the $Sr_2CuO_2Cl_2$ crystal, one needs to account for the re–absorption $\alpha_{3\omega}$ at 3ω. In the limit of l$\ll \lambda$, $\Delta kl \approx$0 this leads to the slightly different expression for the third harmonic intensity

$$I_{3\omega}^{SCOCl} = 2\gamma(\chi_{xxxx}^{(3),SCOCl})^2 I_\omega^3 \exp[-(\frac{3}{2}\alpha_\omega + \frac{1}{2}\alpha_{3\omega})], \tag{V.18}$$

where the interference term of the equation for the optically thick plate is no longer necessary.

The measured relative intensities, together with the absolute value of $\chi_{xxxx}^{(3)}$

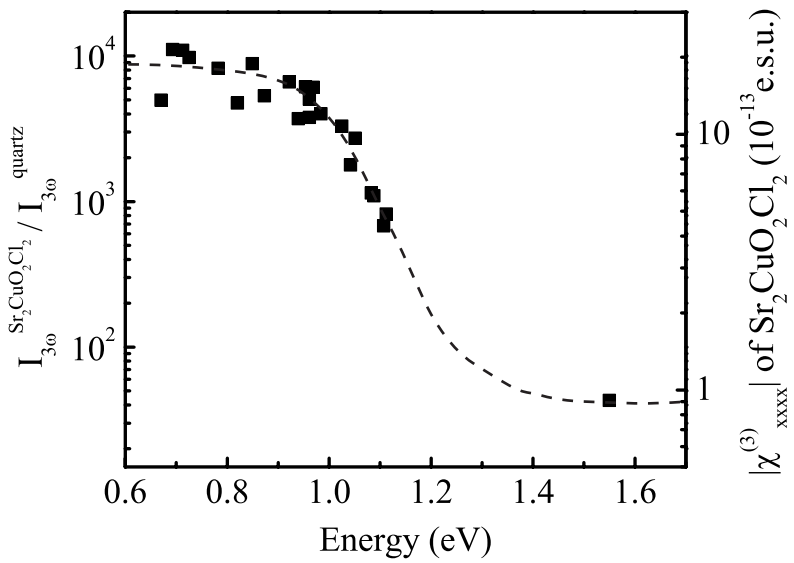

Figure V.11: Third harmonic generation in $Sr_2CuO_2Cl_2$. The left axis shows the relative values of $I_{3\omega} \propto |\chi^{(3)}_{xxxx}|^2$ The right scale indicates absolute values for $Sr_2CuO_2Cl_2$. The dashed line is a guide for the eye.

in $Sr_2CuO_2Cl_2$ are shown in Fig. (V.11). $\chi^{(3)}_{xxxx}$ exhibits a broad, ≈0.8 eV (measured as $1/e^2$) wide resonance between 0.7 and 0.8 eV, varying by more than a factor 20 over the range of frequencies explored. Since the susceptibility $\chi^{(3)}(-3\omega;\omega,\omega,\omega)$ involves summation over many intermediate states (see eq. III.10), the resonance may be indicative of a parity allowed transition at 3ω, or a parity forbidden transition at 2ω, or both. Nevertheless, it is instructive to compare the resonance energies—1.4 to 1.6 eV for a two-photon and 2.1 to 2.4 eV for a three–photon resonance—with previously published results. Very generally, one might differentiate between two different types of excitations, keeping in mind that mixing between the states might occur:

Inter–atomic excitations. Both the models of Zhang [110] and Simón [89] predict charge transfer excitons in addition to the one observed in linear optics. Depending on the model, these excitations would either involve the bonding O $2p\sigma$ or the non bonding $2p\pi$ states. Most of these excitons are parity forbidden, which would lead us to speculate about a resonantly enhanced *two* photon process at 1.6 eV responsible for our resonance. It is also possible that we excite a parity allowed transition at 3ω. In addition to the charge transfer exciton itself, a weak peak has been observed at 2.4 eV, which one group [17] attributed to

the Cu $3d_{x^2-y^2} \rightarrow$ O $2p\pi$ exciton. If this assignment is correct, we may excite this transition in a three photon allowed transition.

Lastly, at ω=0.7 eV, the resonant enhancement could result solely from the CT exciton at 2.1 eV itself, which is then excited by a three-photon transition. The charge transfer exciton bandwidth in $Sr_2CuO_2Cl_2$ was found to be ≈1.2 eV in electron energy loss spectroscopy, which is also the value we used in our model for the linear absorption. This is very close to the width of the third–harmonic peak in our measurement. In contrast, one would expect narrower lines from the atomic–like Cu *dd* transitions.

Intra–atomic Cu *dd* excitations. A number of researchers have suggested excitations from the Cu $3d_{x^2-y^2}$ ground state in $Sr_2CuO_2Cl_2$ to different levels. The weak linear absorption feature at 1.5 eV (see Fig.V.2) was first linked to a $3d_{xy}$ state [77]. Recent resonant Raman spectroscopy locates this $3d_{xy}$ excitation at 1.35 eV, but without offering an alternative explanation for the 1.5 eV feature [31]. The same work suggests 1.8 eV as the energy for the $3d_{x^2-y^2} \rightarrow 3d_{xz,yz}$ transition and speculates that the $3d_{3z^2-r^2}$ state is located also at 1.8 eV. Owing to the great uncertainty in their assignments, any one of the Cu *dd* excitations could be responsible for two or three photon enhancement of $\chi^{(3)}_{xxxx}$. It is therefore necessary to model the resonant behaviour of $\chi^{(3)}$ more carefully and compare the models to the experimental findings.

Existing models for $\chi^{(3)ijkl}$ in cuprates

A few different models have been proposed to calculate $|\chi^{(3)}|$ in quasi one-dimensional Mott–insulators. Kishida *et al.* [48] investigated $|\chi^{(3)}|$ in a number of 1D Mott insulators using the dc Kerr effect, which measures $\Im\chi^{(3)}(-\omega;0,0,\omega)$. Experimentally, they found one resonance peak below the gap, which they modeled and attribute to a large transition dipole moment between an intermediate and final state. Their calculations are based on eq. (III.10), and fit their data well. Mizuno and co–workers [70] use exact diagonalization of a two–bad Hubbard model on small clusters to predict two resonances in $\chi^{(3)}$ near the band gap. In both cases, only the absolute value $|\chi^{(3)}|$ is modeled for a limited range of experimental conditions. Given the number of adjustable parameters which are available in these models if the energy and the widths of the intermediate state are uncertain, it is not entirely surprising how well the models can be made to fit a single resonance observed in one component of $\chi^{(3)}$ experimentally.

V.3.2 Characterization of $\chi^{(3)}(-3\omega;\omega,\omega,\omega)$

Further information about the resonance in $|\chi^{(3)}|$ is clearly desirable. Such experiments, which characterize the complex elements of $\chi^{(3)}$ in amplitude *and* phase have been performed on polymers [16], and it was pointed out how concentrating on the absolute amplitude of the complex susceptibility alone can miss interesting information at best and lead to large errors in the modulus

determination of $\chi^{(3)}$ at worst. But to our knowledge, such careful experiments have not been done in many other materials and not in cuprates.

Yet varying the polarization state of the incoming electromagnetic wave provides us with the possibility of doing just that. Before showing the results of our measurement, the following section will review the symmetry properties of $\chi^{(3)}$ in $Sr_2CuO_2Cl_2$, and demonstrate how we can access phase and detailed amplitude information of the susceptibility.

Crystalographic analysis of third harmonic generation in $Sr_2CuO_2Cl_2$

$Sr_2CuO_2Cl_2$ belongs to the space group I4/mmm, and in our experiment, the **k**-vector of the electromagnetic field is always normal to the (001) plane, spanned by $\hat{x}$ and $\hat{y}$. Since different conventions are sometimes used, it is important to point out that throughout this work, $\hat{x}$ and $\hat{y}$ point in the direction of the Cu–O bonds. For the I4/mmm symmetry, only two *unique*, complex elements of the 4th rank susceptibility tensor $\chi^{(3)}_{ijkl}$ remain to be determined [87] :

$$\begin{aligned}
\chi^{(3)}_{xxxx} &= \chi^{(3)}_{yyyy}, \text{ and} \\
\chi^{(3)}_{xyxy} &= \chi^{(3)}_{xxyy} = \chi^{(3)}_{yxxy} = \chi^{(3)}_{yyxx} \\
&= \chi^{(3)}_{yxyx} = \chi^{(3)}_{xyyx}.
\end{aligned} \tag{V.19}$$

The induced third–order polarization (III.3) is therefore given as

$$\begin{aligned}
P_x &= \chi^{(3)}_{xxxx}E_x^3 + 3\chi_{xyxy}E_xE_y^2, \\
P_y &= \chi^{(3)}_{xxxx}E_y^3 + 3\chi_{xyxy}E_x^2E_y.
\end{aligned} \tag{V.20}$$

These two equations fully describe the macroscopic response of the third–order polarization to an electrical field of arbitrary polarization incident normal to the $\{\hat{x},\hat{y}\}$ plane. It will prove to be useful to distinguish between the amplitude and the phase of the complex susceptibilities,

$$\chi^{(3)}_{xxxx} = \kappa_{xx}\, e^{i\alpha},\ \chi^{(3)}_{xyxy} = \kappa_{xy}\, e^{i\beta} \text{ and } \delta = \beta - \alpha \tag{V.21}$$

Linear input polarization First, we can use linearly polarized light to excite the sample. A $\lambda/2$ plate in the input beam path located before the sample can be rotated to vary the angle of the electrical field continuously with respect to the crystal axes $\hat{x}$ and $\hat{y}$.

The electrical field incident on the sample can thus be expressed as $\mathbf{E} = \hat{x}E\sin\theta + \hat{y}E\cos\theta$. After the sample, we measure the total third harmonic (TH) intensity $|P|^2 = |P_x|^2 + |P_y|^2$, which equals

$$\begin{aligned}
|P|^2 &= E^6[\kappa_{xx}^2 + \frac{3}{4}(3\kappa_{xy}^2 - \kappa_{xx}^2 + 2\kappa_{xx}\kappa_{xy}\cos\delta)\sin^2(2\theta)] \\
&= E^6[\kappa_{xx}^2 + \eta\sin^2(2\theta)],
\end{aligned} \tag{V.22}$$

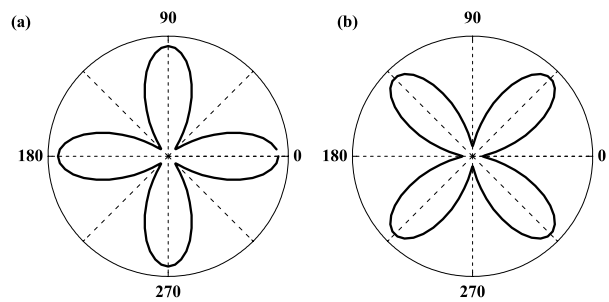

Figure V.12: Theoretical dependence of the TH intensity on the sign of η. (a) For $\eta < 0$, $|P|^2$ is maximized in the direction of the crystal axis. (b) For $\eta > 0$, the maximum occurs at an angle of 45° with respect to the crystal axes.

where we substituted $\eta = \frac{3}{4}(3\kappa_{xy}^2 - \kappa_{xx}^2 + 2\kappa_{xx}\kappa_{xy}\cos\delta)$.

Unless η=0, the third harmonic intensity $I_{3\omega} \propto |P|^2$ therefore shows a four–fold symmetry as shown in Fig. (V.12) (a) and (b), which we did observe experimentally. But as also illustrated in Fig. (V.12), this experiment alone is not sufficient to distinguish between the $\hat{x}$, $\hat{y}$ coordinate system and another one which is rotated by 45° with respect to it. Eq. (V.22) only predicts extrema for $\theta = (0, \frac{\pi}{4}, \frac{\pi}{2}, \frac{3\pi}{4}, \ldots)$, but since the sign of η is unknown, it is not clear if those are extrema *maxima* or *minima*. Regardless of this ambiguity, the experiment allowed us to observe the I4/mmm symmetry of the crystal experimentally.

As indicated in chapter III, we overcame this ambiguity by using X-ray sources to determine the orientation of $\hat{x}$ and $\hat{y}$.

Elliptical input polarization With this knowledge about the crystal orientation we can turn to the case of elliptical input polarization. We consider the case of equal electrical fields in the $\hat{x}, \hat{y}$ direction, where one component is retarded by an amount Δ with respect to the other. Experimentally, this is achieved by means of a Berek compensator; a uniaxial crystal which can be continuously tilted towards the incident laser beam:

$$\mathbf{E} = \hat{x}\frac{E}{\sqrt{2}} + \hat{y}\frac{E}{\sqrt{2}}\,e^{i\Delta}. \tag{V.23}$$

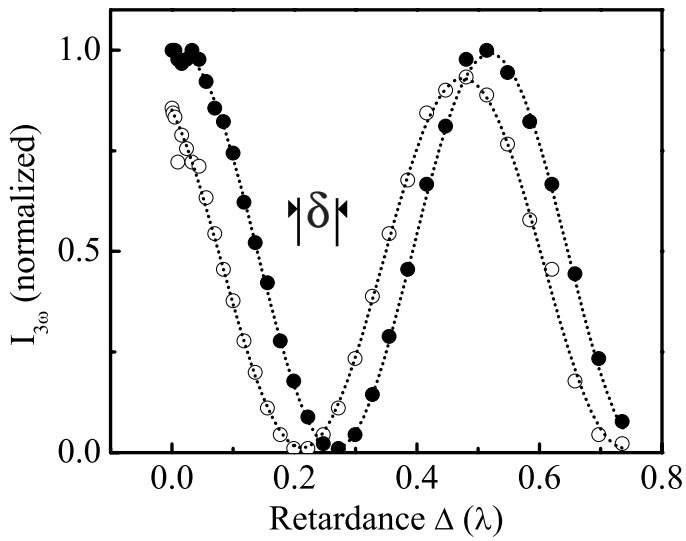

Figure V.13: Example of retardance measurement. $I^x_{3\omega} \propto |P_x|^2$ (filled circles) and $I^y_{3\omega} \propto |P_y|^2$ (open circles) were recorded at ω=1.13 eV. The dashed lines represent best fits to a cos function, from which the relative phase difference δ can be extracted.

Inserting (V.23) into (V.20), we can again find the total polarization $|P|^2$. Now, we are also interested in the third–harmonic intensity $|P_x|^2$ in the $\hat{x}$ and $|P_y|^2$ in the $\hat{y}$ direction (Experimentally, this is easily accomplished by using a polarization analyzer after the sample).

$$|P_x|^2 = \frac{E^6}{8}[\kappa_{xx}^2 + 9\kappa_{xy}^2 + 6\kappa_{xx}\kappa_{xy}\cos(\delta + 2\Delta)] \quad \text{(V.24)}$$

$$|P_y|^2 = \frac{E^6}{8}[\kappa_{xx}^2 + 9\kappa_{xy}^2 + 6\kappa_{xx}\kappa_{xy}\cos(\delta - 2\Delta)] \quad \text{(V.25)}$$

$$|P|^2 = \frac{E^6}{4}[\kappa_{xx}^2 + 9\kappa_{xy}^2 + 6\kappa_{xx}\kappa_{xy}\cos\delta\cos(2\Delta)]. \quad \text{(V.26)}$$

Figure (V.13) shows an example of such a measurement at λ=1400 nm. The slight difference in the absolute amplitude of the two curves is a result of measurement imperfections, and the dotted lines are best fits to $\cos(\delta + 2\Delta)$ and $\cos(\delta - 2\Delta)$.

This experiment therefore allows a complete characterization of $\chi^{(3)}_{xxxx}$ and $\chi^{(3)}_{xyxy}$: From a plot of $|P_x|^2$ and $|P_y|^2$, we can determine the relative phase shift δ, while $|P_{x,y}|^2_{\text{max,min}}$ determines κ_{xx} and κ_{xy}. Both these quantities, κ_{xx}/κ_{xy} and the relative phase shift are plotted in Fig. (V.14).

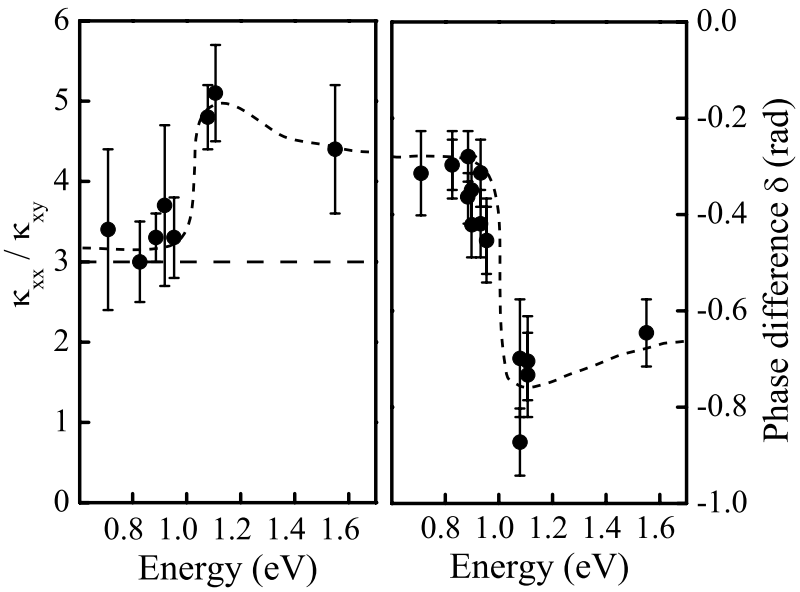

Figure V.14: Relative phase (right panel) and relative magnitude of $\chi^{(3)}_{xxxx}$ and $\chi^{(3)}_{xyxy}$ in $Sr_2CuO_2Cl_2$. Note in both cases the sharp step at 1.05 eV, which is the same energy as the onset of the resonance in V.11. The bars indicate peak–peak–errors, and the dashed lines are a guide to the eye.

Even without any further interpretation, it is evident that both the relative phase and the relative magnitude of $\chi^{(3)}_{xxxx}$ and $\chi^{(3)}_{xyxy}$ undergo a step–like change at 1.05 eV. This energy is identical to that of the resonance in $|\chi^{(3)}_{xxxx}|$, therefore offering an independent confirmation of the observed changes at that energy. But additional information can be extracted from the data in Fig. (V.14).

Spherical symmetry for $\chi^{(3)}_{xxxx}$=3$\chi^{(3)}_{xyxy}$ It is possible to extract additional symmetry properties from $\chi^{(3)}$. To see this, we decompose the susceptibility

tensor into two irreducible components S and D:

$$\begin{aligned}
\mathsf{S} &= 3\chi_{xxxx} + \chi_{xyxy} + \chi_{xxyy} + \chi_{xyyx} \\
&\quad +3\chi_{yyyy} + \chi_{yxyx} + \chi_{yyxx} + \chi_{yxxy} \\
&= 6\left(\chi_{xxxx} + \chi_{xyxy}\right) \\
\mathsf{D} &= \chi_{xxxx} - \left(\chi_{xyxy} + \chi_{xxyy} + \chi_{xyyx}\right) \\
&\quad +\chi_{yyyy} - \left(\chi_{yxyx} + \chi_{yyxx} + \chi_{yxxy}\right) \\
&= 2\left(\chi_{xxxx} - 3\chi_{xyxy}\right) \qquad \text{(V.27)}
\end{aligned}$$

To arrive at the last line of each equation, the identity (V.19) was used. Since we are interested in spherical symmetry properties, we perform a rotation by an angle ϕ of the $\hat{x}$, $\hat{y}$ coordinate frame into a new system $\hat{a}$, $\hat{b}$. The elements of $\chi^{(3)}_{ijkl}$ transform according to [42]

$$\chi_{abcd} = \sum_{ijkl=x,y,z} \left(\cos\phi_{ai}\cos\phi_{bj}\cos\phi_{ck}\cos\phi_{dl}\right)\chi_{ijkl}, \qquad \text{(V.28)}$$

The evaluation of this sum is simplified by the fact that we only need to calculate eight non–zero tensor elements as a function of their counterparts in the original coordinates (see V.19). Furthermore, because we transform one cartesian system into another one, ϕ_{ax}=ϕ_{by}=ϕ. The first element, χ_{aaaa}, reads:

$$\chi_{aaaa} = \left(\cos^4\phi + \sin^4\phi\right)\chi_{xxxx} + 6\cos^2\phi\sin^2\phi\,\chi_{xyxy}. \qquad \text{(V.29)}$$

Similar expressions can be derived for the other elements, and a lengthy but straightforward evaluation gives the new tensor components $\tilde{\mathsf{S}}$ and $\tilde{\mathsf{D}}$ in the new $\hat{a}$, $\hat{b}$ system.

$$\begin{aligned}
\tilde{\mathsf{S}} &= \mathsf{S} \\
\tilde{\mathsf{D}} &= \left(2\cos^2 2\phi - 1\right)\mathsf{D}, \qquad \text{(V.30)}
\end{aligned}$$

A spherical symmetry mandates that $\tilde{\mathsf{S}} = \mathsf{S}$ and $\tilde{\mathsf{D}} = \mathsf{D}\ \forall\ \phi$. The former condition is always satisfied, but the latter requires

$$\mathcal{D} \equiv 0 \iff \chi_{xxxx} = 3\,\chi_{xyxy} \qquad \text{(V.31)}$$

(Unless $(2\cos^2 2\phi - 1) \equiv 0$, which is not the case). In particular, this implies

$$\begin{aligned}
\frac{\kappa_{xx}}{\kappa_{xy}} &= 3 \\
\beta - \alpha &= 0 \qquad \text{(V.32)}
\end{aligned}$$

It is shown in Fig. (V.14) that $\kappa_{xx}\kappa_{xy}$ is indeed very close to 3 between 0.65 eV and 1.05 eV; commensurate with the resonance observed in the absolute value of $|\chi^{(3)}_{xxxx}|$. At higher energies, the ratio increases to five in a deviation from the spherical symmetry. The phase β-α undergoes a step from 0.2 to 0.8 at the

same energy of 1.05 eV. The phase does not go to exactly to zero between 0.65 and 1.05 eV, but this might be consistent with a number slightly above 3 for $\kappa_{xx}\kappa_{xy}$. It is interesting to speculate if the phase is a more sensitive measure to detect slight deviations from the ideal spherical symmetry. Nevertheless, these numbers imply a near–spherical symmetry of the underlying charge distribution commensurate with the resonance in $\chi^{(3)}_{xxxx}$. It is interesting to speculate if the slight non–spherical contribution we see might reflect the d-shaped charge arrangement of the Cu-atoms. Such an albeit weak distortion of the Cu charge density was recently observed using electron diffraction [112]. Beyond that, the additional information gained in this phase measurement is of particular value as we try to reconcile our experimental data with theoretical models.

V.3.3 Model calculations for $\chi^{(3)}$

Already in (V.3.1), we alluded to existing cluster calculations which model the optical nonlinearity at the charge transfer gap. To our knowledge, existing comparisons between theory and experiment focus preferentially on the absolute value of only one component of the nonlinearity, such as $\Im\chi^{(3)}(-3\omega;-\omega,\omega,\omega)$, and often in a limited frequency range. In contrast, the complete characterization carried out here allows us to better discriminate different models. Work is currently under progress to compare our result to a theory of the nonlinear response of $Sr_2CuO_2Cl_2$, which gives access to all the quantities measured here. Here, we present some preliminary results.

Figure (V.15) shows first calculations. They are based on eq. (III.10) and involve different intermediate states and values for transition matrix elements. For both models (left and right column), the matrix elements connecting the $|x^2-y^2\rangle$ ground state to the $|x,y\rangle$ charge transfer excited state are non–zero.

Amplitude of $|\chi^{(3)}_{xxxx}|$ suggests 3 photon resonance to the CT exciton

To obtain a first estimate for the strength of the resonance in $|\chi^{(3)}|$, we fit *linear* absorption with four Lorentzian oscillators and then calculated $\chi^{(3)}_{xxxx}$ using eq. (III.10) based on these oscillators. The result is shown in Fig (V.15), panel (d). The surprisingly good agreement with the experimentally measured of value of $\approx 2\times10^{-12}$ esu strongly implies that the resonance can be explained for the most part with a three photon resonance into the charge transfer state. This challenges works of Kishida *et al.* [48] and Ogasawara *et al.* [73], which both postulate novel resonance mechanism in the one—dimensional compound Sr_2CuO_3 and report "giant" third harmonic efficiencies.

In addition, it is worth noting that the absorption peak seems to contain states with longer lifetimes than the continuum, because otherwise $\chi^{(3)}$ would display a resonance rather than a step. Also, experimentally, the resonance decays much faster towards higher energies than our models based on Lorentzian oscillators (see Fig. V.11 versus Fig. V.15, (a) and (d). This should no be entirely surprising

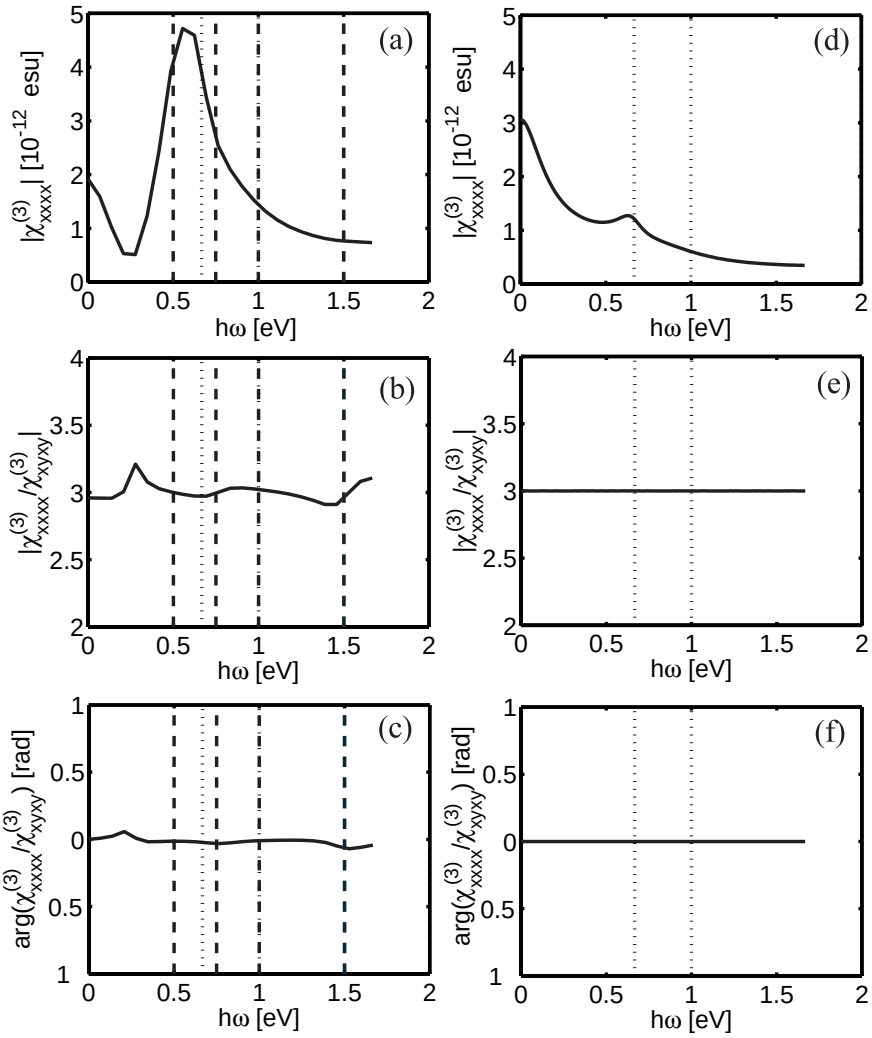

Figure V.15: Models for the nonlinear response of $Sr_2CuO_2Cl_2$. (a)–(c) and (d)–(f) show $|\chi^{(3)}_{xxxx}$, κ_{xx}/κ_{xy} and phase difference δ for two different models, respectively. For (a)–(c) the model incorporates the charge transfer $p_{x,y}$ states at 2 eV, a $3d_{xy}$ state at 1.35 eV, a $3d_{3z^2-r^2}$ state at 1.5 eV and finally an s state at 3 eV. Each level has a particular broadening, and the ground state is of $3d_{x^2-y^2}$ character. (d)–(f) are calculated using only the charge transfer state as an exited state. The apparent resonance at $\hbar\omega$=0 eV in (d) is an artifact.

though, since we demonstrated at the beginning of this chapter how the low energy absorption tail of the CT exciton follows an exponential rather than a

Lorentzian form. Most likely, the assumption of a simple Lorentzian oscillator is not correct.

Phase and relative amplitude of $\chi^{(3)}_{xxxx}$, $\chi^{(3)}_{xyxy}$

On the basis of the absolute $|\chi^{(3)}_{xxxx}|$ alone, it would be difficult to differentiate between the two models displayed in the left and right column of Fig (V.15). The models differ significantly once information about the relative phase and $\frac{\kappa_{xx}}{\kappa_{xy}}$ is included. For the model in the right column (d)–(f), only the $|x, y\rangle$ excited states are considered. The model produces flat values for δ=0 and κ_{xx}/κ_{xy}=3. As we demonstrated above, this implies a perfect spherical. More importantly, we can rule out this simple model on the basis that neither δ nor $\frac{\kappa_{xx}}{\kappa_{xy}}$ shown any variation with frequency. An additional state—either of $|s\rangle$, $|xy\rangle$ or $|3z^2 - r^2\rangle$ symmetry—is needed to explain theses variations.

Such a more complete model is displayed in the left column of Fig (V.15). First, states with $|xy\rangle$ symmetry could be excluded from consideration for $\chi^{(3)}$, since no non–zero matrix elements of eq. (III.10) can be formed for $\chi^{(3)}_{xxxx}$, and elements for $\chi^{(3)}_{xyxy}$ cancel to zero as well. Consequently, the $|xy\rangle$ state is not observable in third harmonic generation and has no influence on the amplitude or phase of $\chi^{(3)}$. The remaining even–parity $|s\rangle$ and $|3z^2 - r^2\rangle$ states indeed induce a deviation from spherical symmetry, as can be seen in Fig. V.15, (b) and (c). Work is currently under way to better understand the role of the two states, and to extract numerical values for transition matrix elements and energies.

V.3.4 Conclusions

We performed third–harmonic generation spectroscopy on the model cuprate $Sr_2CuO_2Cl_2$ over a wide range of energies. Supplementing linear spectroscopy, this technique allows the observation of states which are optically dipole forbidden. We report a resonant enhancement of $|\chi^{(3)}_{xxxx}|$ near 0.7 eV. The absolute value of the resonance was determined through careful measurements of the third harmonic intensity relative to quartz. We determine a peak value of 2×10^{-12} esu. Inferring from linear absorption data, we find that this number can be explained surprisingly well by a three photon transition from the ground state to the charge transfer exciton. We furthermore determined amplitude and phase of $\chi^{(3)}_{ijkl}$ over a range of frequencies, which allows us to characterize the resonance in a much more detailed way. By exploring the tensor's symmetry properties, we find indications for a near–spherical underlying charge distribution. Deviations from this symmetry, and more importantly a step in both relative phase and amplitude of $\chi^{(3)}_{xxxx}$ and $\chi^{(3)}_{xyxy}$ were found. This additional information is consistent with model calculations for the third order susceptibility, but *only* if additional transitions from the ground state to even–parity states are included. From model calculations we find that these states, which cannot be observed in linear spectroscopy, are likely of $|s\rangle$ and $|3z^2 - r^2\rangle$ character. The

effort to better reconcile model calculations and experimental data is ongoing.

V.4 Pump-probe spectroscopy at the CT gap

So far, we have not taken advantage of the temporal resolution which our laser system enables us to obtain. The impact of time–resolved nonlinear optical spectroscopy on solid state physics (and equally on other fields like biology or chemistry) can hardly be overestimated [44]: over the last two decades, a large number of studies have dealt with and explained in great detail ultrafast processes in solids, for example interband transitions in semiconductors [50, 86] or ultrafast thermalization in metals [82].

Encouraged by this success, many attempts have been made to study high-T_c superconductors with well established techniques, such as short–pulse excitation at with a femtosecond laser operating at ∼1.5 eV [13, 33].

- In their metallic state above T_c, superconductors were found to exhibit changes in the the optical properties of a few hundred femtosecond duration. Consistent with results obtained in metals, the fast decay of the signal is commonly ascribed to *ultrafast heating and cooling*. Upon heating with a fs–laser pulse, the electron population rapidly evolves from a non–Fermi distribution to a hot Fermi gas, heated far above the lattice temperature. After thermalization of the electrons, and partly during it, the hot electron gas loses its energy and externally thermalizes with the lattice through electron–phonon scattering [93]. Femtosecond pump–probe experiments therefore can give direct access to the electron–phonon coupling constant. In metals and metallic superconductors such experiments have been successful, and results compare favourably with theory [11].

- Below T_c, interpretation of the data is made more difficult by the lack of a Fermi surface, the absence of a distinct gap in the optical absorption and the presence of Cooper pairs. Empirically, one finds that the relaxation time increases to a few ps [19, 43]. It is believed that the pump laser pulse creates electron–hole pairs which then break up the Cooper pairs into new quasiparticles [33]. The latter act as optically induced scattering centers and break up further Cooper pairs. This avalanche effect explains the observed finite build–up time of the signal. Eventually, all particles relax back to their paired ground state within a few picoseconds. The mechanism(s) for the decay are currently debated.

V.4.1 Previous pump-probe experiments in undoped cuprate materials

To a lesser extent, undoped parent compounds of the cuprates have been investigated by ultrafast pump–probe spectroscopy as well [40,66]. These experiments have probed the optical response in the vicinity of the CT gap after excitation at or above the excitonic peak. Two ideas have been put forward as a result of the measurements, which to the best of our knowledge represent the only current explanation of pump–probe spectroscopy in undoped cuprates:

- The change observed in the spectral line shape upon optical excitation was found to mirror the spectral changes observed upon chemically doping the material with hole carriers [67]. This led to the conclusion that holes, rather than the bound charge transfer exciton or the electron, are responsible for the photoinduced changes as well.

- The temporal response shows a fast (<1 ps) decay similar to the response observed in metals and doped cuprates above T_c. It was suggested that coupling to *magnons* and not to phonons is the dominant decay mechanism [40, 66].

The second suggestion is surprising in light of the theories which prevail in metals and and have successfully explained the signal decay by a coupling to phonons. In addition, we showed at the beginning of this chapter how the *linear* absorption of $Sr_2CuO_2Cl_2$ can only be explained if a strong coupling of the charge transfer exciton to phonons is assumed, whereas magnetic effects do not play a pronounced role. Motivated by this apparent contradiction, we carried out pump–probe experiments on our samples.

Experimental conditions

To access the wide range of relevant energies, we performed time and energy resolved pump-probe spectroscopy with separately tunable pump and probe energies. We used the system described in chapter III, where part of the output of the amplifier system pumps a near-infrared OPA. The OPA allows us to set the pump energy between 0.80 eV and 1.05 eV. In addition, frequency doubling of the OPA or part of the amplifier output extends the range of the pump pulse energy to higher energies, 1.6 eV to 2.1eV or 3.1 eV, respectively. The remainder of the amplifier output can be used to produce a white light probe continuum. A 7–10 nm wide, 200 fs, nJ pulse can be selected from the broadband continuum. This probe is tunable over the entire energy range of the charge transfer exciton from 1.65 eV to 2.25 eV. The polarization of the pump beam was rotated to be orthogonal to the probe beam, so that stray light from the pump can be rejected by means of a polarizer before the detector. The measurements were performed on the same 900 Å thick $Sr_2CuO_2Cl_2$ sample as the third–harmonic generation experiments.

V.4.2 Instantaneous, spectrally resolved response

Overall line shape in comparison to thermal difference spectroscopy

We first focus on the instantaneous ($\Delta t \approx 0$) change in absorption. Figure (V.16) shows the response immediately after excitation at the absorption peak, recorded and compiled for 21 different probe wavelengths. Displayed for comparison is difference in linear absorption at T=250 K and T=15 K (scaled). An increase in absorption is observed for energies below 1.95 eV, whereas a decrease occurs above 1.95 eV. Overall, the spectral weight is not conserved; we will discuss the

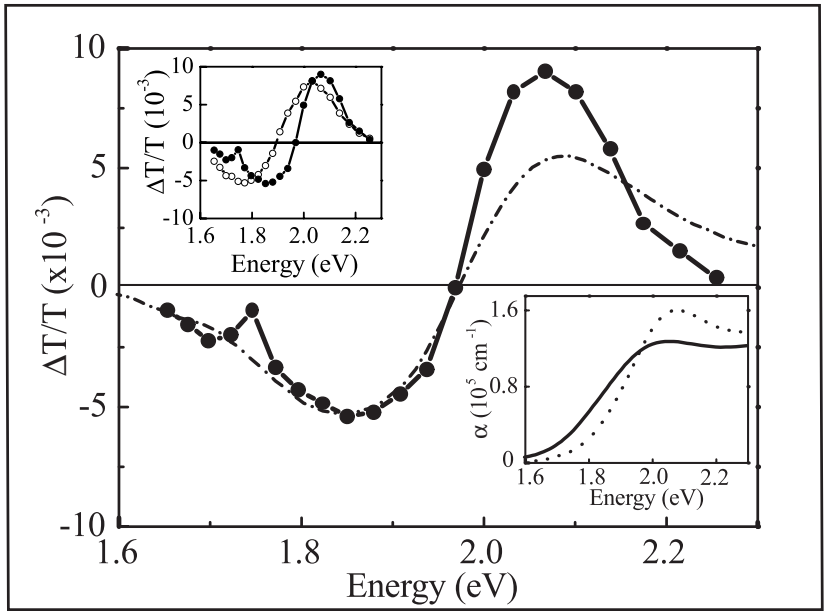

Figure V.16: Instantaneous ($\Delta t \approx 0$) photoinduced changes in $Sr_2CuO_2Cl_2$ after excitation at 2.1 eV, T=15 K (solid line and circles). The excitation density is 7×10^{18} cm^{-3}, or 8×10^{-4}Cu^{-1}. The signal decays as a spectral unit. Shown for comparison is the differential linear absorption, α(250 K)-α(15 K), scaled (dashed- dotted line). Left–top inset: Temperature dependence of the photoinduced signal. T=15 K (solid line and circles) and T=300 K (dashed line and open circles) Right–bottom inset: linear absorption at 15 K (dashed) and at 300 K (solid line) for reference.

weak photobleaching below. The transient changes appear as one spectral unit instantaneously after photoexcitation, and decay—again as one spectral unit—on a ps-timescale (illustrated in Fig. (V.17 for a higher pump energy). If the sample temperature is raised from 15 K to 300 K, the spectral feature is red–shifted, but the overall shape changes little (see left inset of Fig V.16). Apparently, the underlying physics is not strongly affected by the transition through the Néel point at T=255 K. Surprisingly, no hole–burning can be observed at the pump energy of 2.1 eV. In order to discuss the origin of the photoinduced spectral change as shown in Fig (V.16), we can compare the spectral shape of the transient the thermal difference spectrum between 50 K and 250 K. Apart from the photobleaching, the two curves show a remarkable similarity.

This similarity, and the fact that the transient decays as one spectral unit, strongly suggest that the underlying mechanism for the pump-probe line shape is the same as the one responsible for the changes in linear absorption with

temperature. In the first part of this chapter, we demonstrated how a strong coupling between the charge transfer exciton and phonons can be identified as the cause for the temperature–dependence of the linear absorption. We therefore suggest that the pump-probe response is dominated by the coupling of the charge transfer exciton to phonons as well. We take note that results published earlier [66] on insulating $YBa_2Cu_3O_{6.2}$ and Nd_2CuO_4 promote a different hypothesis. There, a similar increase in absorption at energies below, and decrease at energies above the charge transfer gap was observed. The authors however speculate that those are two independent spectral features. They assign the increase in absorption at lower energies to light–induced in–gap states, and propose an excited CT-exciton state, which allegedly couples to magnons rather than phonons to be at the origin of the decreased absorption at higher energies.

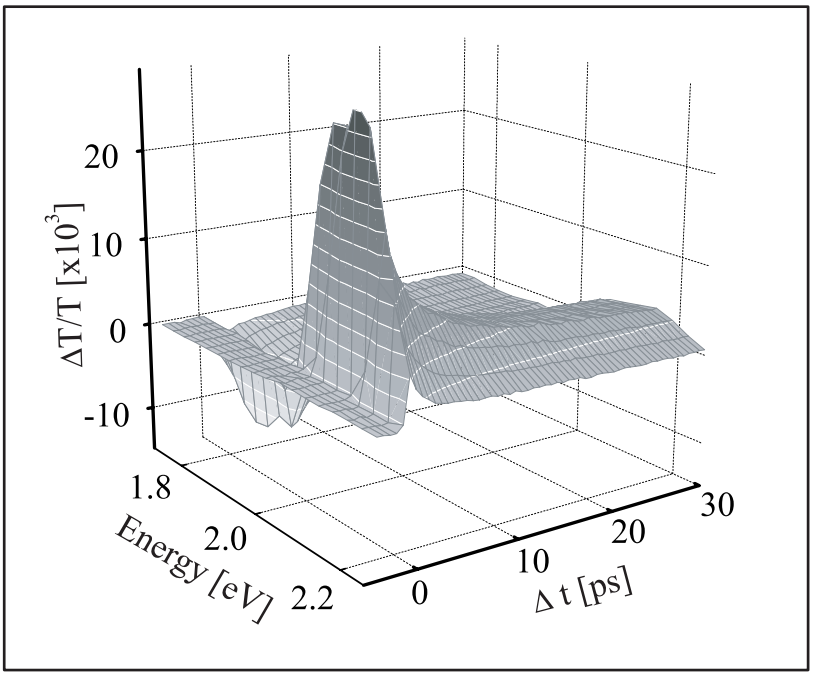

Figure V.17: Time– and energy resolved plot of photoinduced response at 3.1 eV pump energy. The transient feature appears and decays as one spectral unit. The excitation conditions are the same as for Fig. (V.16).

Strong coupling of exciton to phonons

Despite these earlier results, since empirically both photoexcitation and disordered, thermal heating show a very similar spectral signature, we feel confident

to conclude that both the presence of photoexcited excitons (or of their constituting parts) and the addition of thermal phonons influence the exciton energy in the same way. An effective phonon number n_{eff} can thus be associated with each exciton. For $\hbar\omega_{pump}$=2.1 eV, we find n_{eff}=9, which again is indicative for a strong coupling between the gap excitation and phonons in $Sr_2CuO_2Cl_2$. Work is currently under way to compare this effective phonon number n_{eff} with the exciton–phonon coupling matrix element $|M_{nm}|^2 = 20(\hbar\omega_0)^2$ obtained earlier in this chapter (see part V.2.3).

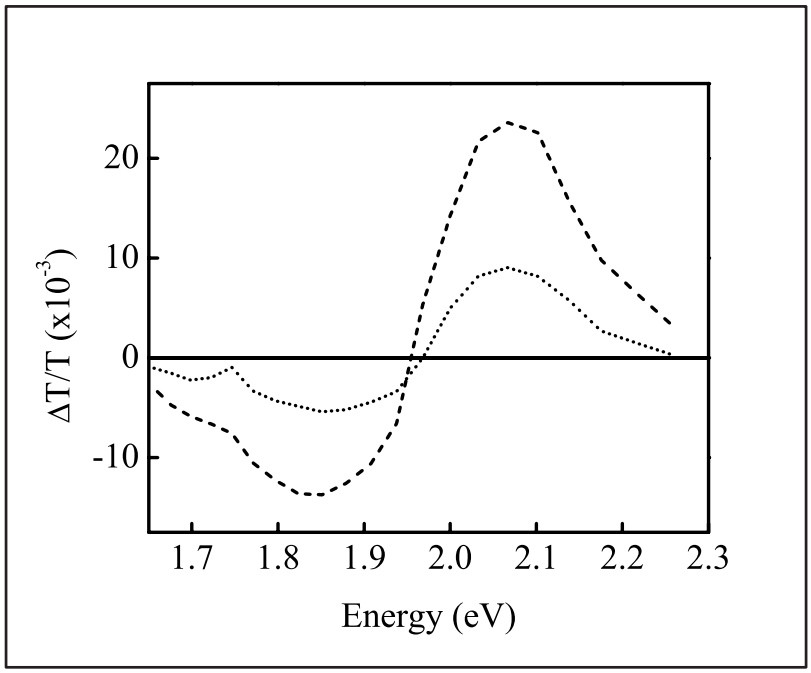

Figure V.18: Comparison between photoinduced response at 2.1 eV (dotted line) and 3.1 eV(dashed line) pump energy. In both cases the excitation density is again 7×10^{18} cm^{-3}, or $8\times$ 10^{-4}Cu^{-1}. T=15 K

To test this "effective phonon" picture, it is informative to see what happens if the pump energy is raised by $\Delta\hbar\omega_{pump}$=1 eV, which is more than four times the exciton binding energy of 240 meV. The results are shown in Fig. (V.18): The overall line shape is identical, but for the same number of absorbed photons the signal strength is larger, resulting in n_{eff}=23. This higher number strengthens our phenomenological argument, since with $\hbar\omega_{phonon}$ ≈50 meV, this accounts for all but 30% of the excess pump photon energy.

Matsuda *et al.* have pointed out how the pump–probe transient—both time and

energy resolved—in $YBa_2Cu_3O_{6.2}$ varies surprisingly little with the pump photon energy [67]. Like in our own experiment, they excited the sample at energies far above the charge transfer exciton and report no change in the spectral– or time–resolved response[5]. To explain their observation, Matsuda *et al.* put forward the idea that not the exciton itself, but only the *hole* in the O $2p$ band is responsible for the observed spectral changes. This argument is strengthened through an observation by Ichida *et al.*. They pointed out that *photoinduced* absorption changes in undoped cuprates, and the changes which occur after *chemically doping* the material with hole carriers at comparable densities are very similar [40]. While we cannot add new experimental insight to this argument, we point out that our theoretical model (see V.2.3) does not distinguish whether the signal is due to the charge transfer exciton or any of its constituting parts: the phonon coupling matrix elements in our model to explain the linear absorption are the same for the charge transfer exciton bound state and its electron–hole continuum.

Bleaching and "excluded area" of the exciton

Careful comparison between the thermal and the pump-probe line shape reveals a weak bleaching of the exciton line. The dominance of phonon-mediated effects over the bleaching deviates from results obtained in band semiconductors, where instantaneous bleaching due to phase space filling is strong [86].

To quantitatively asses the strength of the phase–space filling we can adopt the "excluded volume" argument [14] for our quasi—two dimensional material: Once an exciton is created, a (real space) area approximately equal to the spatial size of the exciton is excluded from further absorption. More careful many–body calculations confirm the validity of this phenomenological argument.

Excitation energy	2.1 eV		3.1 eV	
Temperature	15 K	300 K	15 K	300 K
$\alpha[\times 10^4\,\mathrm{eVcm}^{-1}]$	5.8	5.7	6.3	6.2
$\Delta\alpha[\mathrm{eVcm}^{-1}]$	65	93	230	351
n $[\mathrm{Cu}^{-1}]$	$8{\cdot}10^{-4}$	$8{\cdot}10^{-4}$	$8{\cdot}10^{-4}$	$8{\cdot}10^{-4}$
Excluded area [Cu]	1.4	2.7	4.5	7.1

Table V.2: Photobleaching of the charge–transfer exciton. α and $\Delta\alpha$ are the total absorption and the effective change in absorption (bleaching) over the energy range of the transient signal, respectively. n is the number of photoinduced excitations assuming a quantum efficiency of one.

[5] No comments were made on variations in the signal *strength* per absorbed photon. Furthermore, as mentioned above, Matsuda *et al.* favour a very different explanation for the overall line shape.

Table (V.4.2) summarizes the results. For different excitation conditions, we extracted the effective change in absorption $\Delta\alpha$ from our pump–probe data and related it to the total absorption α over the same energy range. By dividing the ration through the number of photoinduced excitations per copper atom (assuming a phonon–to–exciton quantum efficiency of unity), we obtain the number of "excluded" copper atoms per excitation.

The Zhang-Ng charge transfer exciton in Fig. (V.3) extends over an area of approximately five copper atoms in the CuO_2 layer. To first approximation, this is in a very good agreement with the numbers in table (V.4.2). It is surprising however that excluded volume appears to change by a factor of three as the pump energy is raised from 2.1 eV to 3.1 eV, and also undergoes a slight variation as a function of temperature. We can speculate that an unbound electron–hole pair at 3.1 eV has a combined larger effective area which is excluded from further absorption than the bound CT exciton at 2.1 eV.

Finally, we comment on a small feature in the pump probe time–resolved pump–probe line shape in Fig. (V.16). A weak absorption feature separate from the main peak can be observed around 1.7 eV at low temperature. This feature might be due to one of the intra–ionic Cu *dd* excitations. Since we did not yet examine the symmetry properties of the peak, we can only speculate that it might be due to the Cu $d_{x^2-y^2} \rightarrow d_{yz}$ excitation, which has previously been observed in resonant X-ray Raman spectroscopy [31]. Alternatively, a Cu $d_{x^2-y^2} \rightarrow d_{3z^2-r^2}$ transition should occur at roughly this energy, but so far has not been observed experimentally.

V.4.3 Temporal evolution of the pump-probe signal

The temporal evolution of the pump probe signal is plotted in Fig. (V.19). While we show here only one excitation condition ($\hbar\omega_{pump}$=3.1 eV, T=15 K) at three different pump intensities, the decay behaviour shows a remarkable invariance to external conditions in general. We can characterize it by an initial fast decay, followed by a much slower second decay process. For a wide range of pump energies, intensities and temperatures explored here, the fast decay can be characterized by τ_1=(3±1) ps, whereas the longer time constant is τ_2=(55±15) ps. Furthermore, as evident from the poor fit results in Fig. (V.19), the decay cannot be characterized simply by the sum of two exponential terms. We would like to point out the similarity between the initial fast time scale observed here, and the similar time scales which can be observed in doped, superconducting materials below T_c.

An interpretation of the data is complicated by the lack of variation with temperature, excitation wavelength or intensity. Owing the strong coupling between CT exciton and phonons which dominates both linear and nonlinear experiments, it seems natural to assume a nonradiative multi–phonon process in the strong coupling regime. In localized objects, such as small molecules, excited

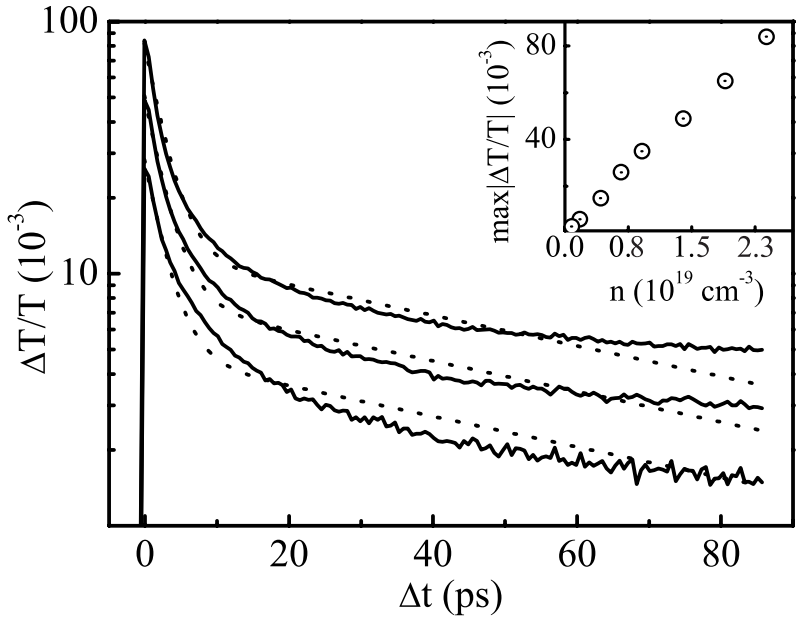

Figure V.19: Time–resolved spectroscopy at 3.1 eV pump and 2.1 eV probe energy for three different excitation densities (0.3, 1.5, 2.3 $\times 10^{19}$cm^{-3} from bottom to top). The dashed lines represent global best fits to a double exponential decay with τ_1=2.6 ps and τ_2=70 ps. The inset shows the linear power dependence of the instantaneous signal as a function of the carrier density n. Sample temperature 15 K

electronic states often display altered atomic coordinates, which can lead to self–trapping of excitons, an effect which cannot be observed in solids with delocalized excitations [80]. We might speculate that a similar situation occurs for the charge transfer exciton: We know that either the exciton as a bound object, or perhaps the hole individually couples very strongly to phonons. It is conceivable that the initial photoexcitation occurs into a state with altered atomic coordinates, from which an fast relaxation occurs. The relaxation of such a localized object would create high–energy phonons, which could then in a second process transfer the energy to a thermal phonon population. But clearly, further experiments are needed to address the issue of relaxation time scales exhaustively.

V.4.4 Pump-probe experiments below the charge transfer gap

We have also performed pump-probe spectroscopy below the charge transfer gap. Such experiments might shine light onto the coupling between charge–transfer exciton and states below the gap and furthermore supplement the third–harmonic spectroscopy presented above. Our interpretation is at an early stage, but we would nevertheless like to show first results.

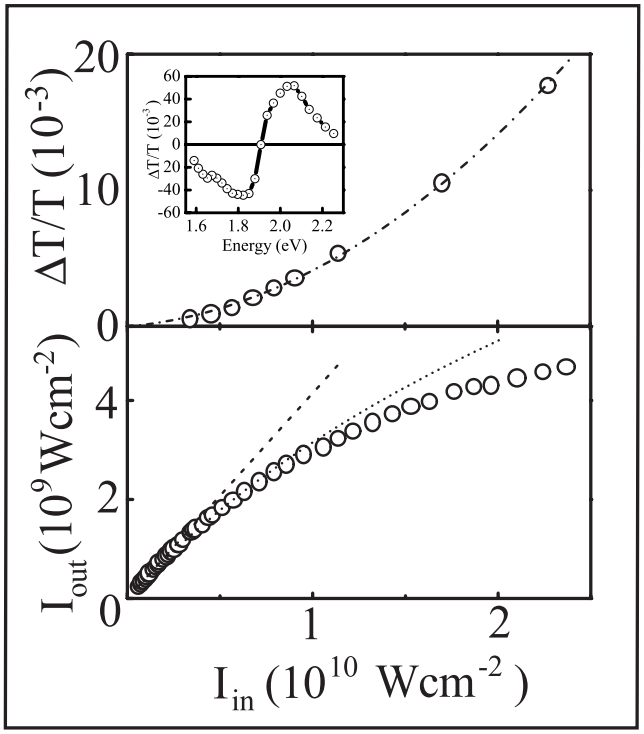

Figure V.20: Pump–probe spectroscopy below gap. Inset shows the spectrally resolved response at $\Delta t \approx 0$. Top panel: Nonlinear power dependence of the same signal as function of the incident intensity (the dashed-dotted line represents a fit to a 3rd order polynomial. The bottom panel gives the transmitted intensity as a function of the incident one (dashed line: linear absorption line, dotted line: one plus two–photon absorption)

Most importantly, as shown in the top panel of Fig. (V.19), the dependence of the pump probe signal signal is no longer a linear one when pumped at 1.03 eV. This is not entirely surprising, owing the three–photon process we identified, and the possible presence of optically dipole forbidden states which could be

accessed by means of a two–photon process. The lower panel of Fig. (V.20) plots the transmitted intensity as a function of the incident intensity for the same excitation conditions. The dashed line shows the linear functional form expected if only one–photon absorption would be present in the sample. Clearly, higher–order processes need to be considered, as even combined one– and two–photon absorption (dotted line) does not fit the measured data over the entire range.

At the same time, the spectrally resolved response at the charge transfer gap (Inset of Fig. V.20) remains much the same compared to above–the–gap pumping, shown in (Fig. V.18).

Ogasawara *et al.* report a nonlinearity in the one dimensional compound $SrCuO_3$ under similar excitation conditions [73]. They report that the absolute value of the *nonlinear* susceptibility, if plotted for different energies around the charge transfer gap, mirrors the value of the *linear* susceptibility (i. e. the linear absorption). In contrast to the linear absorption, which shows a step–like behaviour, the nonlinear absorption decreases towards higher energies. Overall, the spectral shape reported by Ogasawara *et al.* bears some similarity to the resonance which we measured in $\chi^{(3)}_{xxxx}$ with third harmonic spectroscopy. Ogasawara *et al.* propose a novel, two–photon active state caused by an even parity superposition of two charge transfer excitons to explain the results.

Considering our findings in third harmonic spectroscopy, which strongly imply a three–photon resonance to the charge transfer gap, an alternative explanation for the nonlinear response should also be considered. If excited and probed below the gap, two photons from the strong pump beam at ω_{pump} and one probe photon ω_{probe} can coherently interact and cause a three photon transition at $2\omega_{pump}+\omega_{probe}$ to the charge transfer exciton. The re–emitted photons at $\omega_r=2\omega_{pump}+\omega_{probe}$ would be re–absorbed in the sample. Alternatively, a direct three photon transition with $3\omega_{pump}$ is possible. In both cases, the intermediate states which we identified through third harmonic spectroscopy, would be accessible through a two photon resonance. Most likely, both two and three photon resonances appear simultaneously. The explanation of a multi–photon process, follow by re–emission of a photon at higher energies and subsequent re–absorption is strengthened by our spectrally resolved measurements at 1.03 eV (inset of Fig V.20) which are strikingly similar to the results obtained by pumping at 2.1 eV and 3.1 eV: This can naturally be explained by re-absorption of a photon at ω_r. On the other hand, it is not immediately obvious why the novel two–photon state proposed by Ogasawara *et al.* should cause the same spectral response as the excitation of a charge transfer exciton.

V.4.5 Conclusions

We have monitored the temporal and spectral evolution of the charge transfer exciton over a wide range of parameters. By spectrally resolving the pump–

probe data, we find the light–induced changes to be strikingly similar to changes obtained by disordered heating of the sample. In contrast to earlier work on similar materials, we therefore propose that the pump–probe signal is dominated by strong coupling between the charge transfer exciton and phonons. It is therefore likely that the complex decay dynamics, which can be described by two time scales of order 2 ps and 55 ps, are dominated by a nonradiative multi–phonon processes. We also observed a weak photobleaching of the pump probe signal. A phenomenological model based on the the "excluded volume" argument, accounts for this effect. Pumping below the CT exciton reveals a nonlinear relationship between the pump probe signal and the pump intensity. We presented some evidence that a multi–photon transition to the charge transfer exciton, followed by re–absorption of the high–energy photon might explain our data.

Bibliography

[1] R. R. Alfano. *The supercontinuum light source.* Springer Verlag, New York, 1 edition, 1989.

[2] J. W. Allen, R. M. Macfarlane, and R. L. White. Magnetic Davydoff splitting the the optical absorption spectrum of Cr_2O_3. *Phys. Rev.*, 179(2):523–41, 1969.

[3] P. W. Anderson. An approximate quantum theory of the antiferromagnetic ground state. *Phys. Rev.*, 86(5):694–701, 1952.

[4] P. W. Anderson. *Phys. Rev.*, 115:2, 1959.

[5] P. W. Anderson. Resonating valence bonds: a new kind of insulator? *Mater. Res. Bull.*, 8(2):153–60, 1973.

[6] P. W. Anderson. The resonating valence bond state in $LaCuO_4$ and superconductivity. *Science*, 235:1196–8, 1987.

[7] J. G. Bednorz and K. A. Müller. Possible high T_c superconductivity in the Ba– La–Cu–O system. *Z. Phys.*, B64:189–93, 1986.

[8] F. Bloch. *Z. Physik*, 61:206, 1930.

[9] R. W. Boyd. *Nonlinear Optics.* Academic Press, Inc., San Diego, 9 edition, 1992.

[10] A. Brodeur and S. L. Chin. Band-gap dependence of the ultrafast white–light continuum. *Phys. Rev. Lett.*, 80(20):4406–9, 1998.

[11] S. D. Brorson et al. Femtosecond room-temperature measurement of the electron–phonon coupling constant λ in metallic superconductors. *Phys. Rev. Lett.*, 64(18):2172–4, 1990.

[12] S. Chakravarty, M. G. Gelfand, and S. Kivelson. Electronic correlation effects and superconductivity in doped fullerenes. *Science*, 254(5034):970–4, 1991.

[13] S. V. Chekalin et al. Femtosecond spectroscopy of YBa_2Cu_3 $O_{7-\delta}$: Electron–phonon–interaction measurement and energy–gap observation. *Phys. Rev. Lett.*, 67(27):3890–3, 1991.

[14] D. S. Chemla, D. A. B. Miller, P. W. Smith, A. C. Gossard, and W. Wiegmann. Room temperature excitonic nonlinear absorption and refraction in Ga As/AlGaAs multiple quantum well structures. *IEEE J. Quantum Electr.*, 20(3):265–75, 1984.

[15] D. S. Chemla and J. Zyss. *Nonlinear optical properties of organic molecules and crystals*, volume 1 of *Quantum Electronics—Principles and Applications*. Academic Press, Inc., New York, 1 edition, 1987.

[16] D. S. Chemla and J. Zyss. *Nonlinear optical properties of organic molecules and crystals*, volume 2 of *Quantum Electronics—Principles and Applications*. Academic Press, Inc., New York, 1987.

[17] H. S. Choi et al. Anomalous temperature dependence of charge-transfer excitation in the undoped cuperate $Sr_2CuO_2Cl_2$. *Phys. Rev. B*, 60:4646–52, 1999.

[18] A. V. Chubukov and D. K. Morr. Dispersion of a single hole in an antiferromagnet. *Phys. Rev. B*, 57(9):5298–311, 1998.

[19] J. M. Chwalek et al. Femtosecond optical absorption studies of nonequilibrium electronic processes in high T_c superconductors. *Appl. Phys. Lett.*, 57:1696–98, 1992.

[20] P. A. Cox. *Transition metal oxides*, volume 27 of *International Series of Monographs in Chemistry*. Clarendon Press, Oxford, 1992.

[21] D. P. DiVincenzo, D. Bacon, J. Kempe, G. Burkard, and K. B. Whaley. Universal quantum computation with the exchange interaction. *Nature*, 408:339–42, 2000.

[22] J. D. Dow and D. Redfield. Towards a unified theory of Urbach's rule and exponential absorption edges. *Phys. Rev. B.*, 5(2):594–60, 1972.

[23] F. Dyson, E. H. Lieb, and B. Simon. Phase transitions in quantum spin systems with isotropic and nonisotropic interactions. *J. Stst. Phys.*, 18(4):335–83, 1978.

[24] F. J. Dyson. General theory of spin-wave interactions. *Phys. Rev.*, 102(5):1217–44, June 1956.

[25] V. J. Emery. Theory of high-T_c superconductivity in oxides. *Phys. Rec. Lett.*, 58:2794–97, 1987.

[26] J. P. Falck, A. Levy, M. A. Kastner, and R. J. Birgeneau. Charge-transfer spectrum and its temperature dependence in La_2CuO_4. *Phys. Rev. Lett.*, 69:1109–12, 1992.

[27] F. Gebhard. *The Mott Metal–Insulator transition*, volume 137 of *Spinger tracts in modern physics*. Springer Verlag, Heidelberg, 1997.

[28] R. L. Greene, D. D. Sell, W. M. Yen, A. L. Schwalow, and R. M. White. *Phys. Rev. Lett.*, 15:656–59, 1965.

[29] M. Greven et al. Spin correlation in the 2 dimensional Heisenberg antiferromagnet $Sr_2CuO_2Cl_2$: neutron scattering, Monte Carlo simulations, and theory. *Phys. Rev. Lett.*, 72(7):1096–9, 1994.

[30] M. Grueninger et al. Mid-infrared absorption in $YBa_2Cu_3O_6$: Failure of spin-wave theory in undoped cuperates? *http://xxx.lanl.gov*, pages cond–mat/9904394, 1999.

[31] P. Kuiper J.-H. Guo, C. Sathe, L.-C. Duda, and J. Nordgren. Resonant X-ray Raman spectra of Cu *dd* excitations in $Sr_2CuO_2Cl_2$. *Phys. Rev. Lett.*, 80:5204–7, 1998.

[32] M. C. Gutzwiller. *Phys. Rev. Lett.*, 10:159, 1963.

[33] S. G. Han, Z. V. Vardeny, K. S. Wong, O. G. Symko, and G. Koren. Femtosecond optical detection of quasiparticle dynamics in high–T_c $YBa_2Cu_3O_{7-\delta}$ thin films. *Phys. Rev. Lett.*, 65:2708–11, 1990.

[34] E. Hanamura, N. T. Dan, and Y. Tanabe. Excitons and two-magnon Raman scattering of the strongly correlated systems La_2CuO_4 and $YBa_2Cu_3O_6$. *Phys. Rev. B*, 62(11):7033–44, 2000.

[35] S. M. Hayden et al. High energy spin waves in $LaCuO_4$. *Phys. Rev. Lett.*, 67(25):3622–5, 1991.

[36] B. Henderson and G. F. Imbusch. *Optical Spectroscopy of Inorganic Solids.* Clarendon Press, Oxford, 1989.

[37] J. P. Hermann. Absolute measurement of third order susceptibilities. *Opt. Commun.*, 9(1):74–8, 1973.

[38] T. Holstein and H. Primakoff. Field dependence of the intrinsic domain magnetization of a ferromagnet. *Phys. Rev.*, 58:1098, 1940.

[39] J. Hubbard. Electron correlations in narrow energy bands. *Proc. Roy. Soc.*, A276:238–257, 1963.

[40] M. Ichida, K. Hayakawa, K. Matsuda, A. Nakamura, and I. Hirabayashi. Femtosecond optical response of optical constants due to charge–transfer excitation in Nd_2CuO_4. *Solid State Commun.*, 108(3):145–9, 1998.

[41] J. Igarashi. 1/S expansion for thermodynamic quantities in a two dimensional Heisenberg antiferromagnet at zero temperature. *Phys. Rev. B*, 46(17):10763–71, 1992.

[42] J. Jerphagnon and D. S. Chemla. Optical activity of crystals. *J. Chem. Phys.*, 65(4):1522–29, 1976.

[43] R. A. Kaindl. *Ultrafast midinfrared studies of low energy excitations in solids*. PhD thesis, Humbolt University, Berlin, 2000.

[44] W. Kaiser. *Ultrashort Laser Pulses - Generation and Application*, volume 60 of *Topics in Applied Physics*. Springer Verlag, New York, 2 edition, 1992.

[45] J. Kanamori. *Prog. Theor. Phys.*, 30:275, 1963.

[46] M. A. Kastner, R. J. Birgeneau, G. Shirane, and Y. Endoh. Magnetic, transport, and optical properties of monolayer copper oxides. *Rev. Mod. Phys.*, 70(3):897–928, 1998.

[47] T. Kennedy, E. H. Lieb, and B. S. Shastry. Existence of Neel order in some spin-1/2 Heisenberg antiferromagnets. *J. Stat. Phys.*, 53:1019, 1988.

[48] H. Kishida et al. Giant optical nonlinearity in one–dimensional Mott–Hubbard–insulators. *Nature*, 405:929–32, 2000.

[49] C. F. Klingshirn. *Semiconductor Optics*. Springer Study Edition. Springer Verlag, Berlin, 1997.

[50] P. Kner. *Exciton–Exciton Correlations in Semiconductors in High Magnetic Fields*. PhD thesis, University of California, Berkeley, 1998.

[51] P. Kopietz. Magnon damping in the two-dimensional quantum Heisenberg antiferromagnet at short wavelength. *Phys. Rev. B*, 41(13):9228–38, 1990.

[52] Thilo Kopp. private communication, 1999.

[53] R. Kubo. The spin wave theory of antiferromagnetics. *Phys. Rev.*, 87(4):568–80, 1952.

[54] M. V. Kurik. Urbach rule. *Phys. Stat. Sol. A*, 8:9–45, 1971.

[55] W. M. Dennis L. D. Rotter and W. M. Yen. Dynamics of large-wave-vector magnons and phonons in MnF_2Er^{3+} using a far infrared quantum-counter technique. *Phys. Rev. B*, 42(1):720–4, 1990.

[56] J. G. Liebler, S. Schmitt-Rink, and H. Haug. Theory of the absorption tail of Wannier excitons in polar semiconductors. *J. Lum.*, 24:1, 1985.

[57] R. Liu et al. Novel Raman-active electronic excitations near the charge-transfer gap in insulating cuprates. *Phys. Rev. Lett.*, 71:3709–12, 1993.

[58] J. Lorenzana, J. Eroles, and S. Sorella. Does the Heisenberg model describe the multimagnon spin dynamics in antiferromagnetic CuO layers? *Phys. Rev. Lett.*, 83(24):5122–5, 1999.

[59] J. Lorenzana and G. A. Sawatzky. Phonon assisted multimagnon optical absorption and long lived two-magnon states in undoped lamellar copper oxides. *Phys. Rev. Lett.*, 74:1867–70, 1995.

[60] J. Lorenzana and G. A. Sawatzky. Theory of phonon-assisted multimagnon optical absorption and bimagnon states in quantum antiferromagnets. *Phys. Rev. B*, 52:9576–89, 1995.

[61] R. M. Macfarlane and J. W. Allen. Exciton bands in antiferromagnetic Cr_2O_3. *Phys. Rev. B*, 4(9):3054–67, November 1971.

[62] Gerald D. Mahan. *Many–particle physics*, volume II. Plenum Publishing Corp., New York, 1990.

[63] P. D. Maker, R. W. Terhune, M. Nisendorf, and C. M. Savage. Effects of dispersion and focusing on the production of optical harmonics. *Phys. Rev. Lett.*, 8(1):21–2, 1962.

[64] S. V. Maleyev. Spin-wave interaction and renormalization of magnetic anisotropy in 2d antiferromagnets. *Phys. Rev. Lett.*, 85(15):3281–4, 2000.

[65] E. Manousakis. The spin-1/2 Heisenberg antiferromagnet on a square lattice and its applications to the cuprate oxides. *Rev. Mod. Phys.*, 63:1, 1991.

[66] K. Matsuda et al. Femtosecond spectroscopic studies of the ultrafast relaxation process in the charge–transfer state of insulating cuprates. *Phys. Rev. B*, 50(6):4097–101, 1994.

[67] K. Matsuda et al. Femtosecond spectroscopic studies of photodoping effects in insulating $YBa_2Cu_3O_{6+x}$ and Nd_2C uO_4 thin films. *Physica C*, 280:84–92, 1997.

[68] N. D. Mermin and H. Wagner. Absence of ferromagnetism or antiferromagnetism in one– or two–dimensional isotropic Heisenberg models. *Phys. Rev. Lett.*, 17(22):1133–6, 1966.

[69] L. L. Miller et al. Synthesis, structure, and properties of $Sr_2CuO_2Cl_2$. *Phys. Rev. B*, 41:1921–5, 1990.

[70] Y. Mizuno, K. Tsutsui, T. Tohyama, and S. Maekawa. Nonlinear optical response and spin–charge seperation in one–dimensional Mott insulators. preprint, arXiv:cond-mat/0006335.

[71] B. Norden and E. Krutmeijer. The Nobel prize in chemistry, 2000: Conductive polymers. *Royal Swedish Academy of Sciences*, 1:1–16, 2000.

[72] T. Norris. Femtosecond pulse amlification at 250 kHz with a Ti:sapphire regenerative amplifier and application to continuum generation. *Opt. Lett.*, 17(14):1009–12, 1992.

[73] T. Ogasawara et al. preprint, arXiv:cond-mat/0002286.

[74] T. Oguchi. Theory of spin-wave interaction in ferro- and antiferromagnetism. *Phys. Rev.*, 117(1):117–23, 1960.

[75] J. Orenstein and A. J. Millis. Advances in the physics of high–temperature superconductivity. *Science*, 288:468–74, 2000.

[76] J. D. Perkins et al. Mid-infrared optical absorption in undoped lamellar copper oxides. *Phys. Rev. Lett.*, 71:1621–4, 1993.

[77] J. D. Perkins et al. Midinfrared optical excitations in undoped lamellar copper oxides. *Phys. Rev. B*, 58:9390–9401, 1998.

[78] M. K. Reed, M. K. Steiner-Shepard, M. S. Armas, and D. K Negus. Microjoule–energy ultrafast optical parametric amplifiers. *Opt. Lett.*, 12(11):2229–36, 1995.

[79] M. K. Reed, M. K. Steiner-Shepard, and D. K. Negus. Tunable ultraviolett generation using a femtosecond 250 kHz Ti:sapphire regenerative amplifier. *Opt. Lett.*, 31(9):1614–18, 1995.

[80] L. H. Robins. *Optical and magnetic studies of the photoluminescence centers in crystalline and amorphous arsenic triselenide.* PhD thesis, Massachusetts Institute of Technology, Boston, 1979.

[81] E. J. Samuelsen, M. T. Hutchings, and G. Shirane. Inelastic neutron scattering investigation of spin waves and magnetic interactions in Cr_2O_3. *Physia*, 48:13–42, 1970.

[82] R. W. Schoenlein, W. Z. Lin, J. G. Fujimoto, and G. L. Easley. Femtosecond studies of nonequilibrium processes in metals. *Phys. Rev. Lett.*, 58(16):1680–83, 1987.

[83] M. Schreiber and Y. Toyazawa. Mumerical experiments on the absorption lineshape of the exciton under lattice vibrations. *J. Phys. Soc. Jpn.*, 51(5):1528–36, 1982.

[84] A. B. Schumacher. Regenerative amplification of femtosecond pulses: Design and construction of a sub–100 fs, μJ laser system. Master's thesis, Technical University of Karlsruhe, Karlsruhe, Germany, 1996.

[85] D. D. Sell, R. L. Greene, and R. M. White. *Phys. Rev.*, 158:489–510, 1968.

[86] J. Sha. *Ultrafast spectroscopy of semiconductors and semiconductor nanostructures*, volume 115 of *Springer Series in Solid State Sciences.* Springer Verlag, New York, 1992.

[87] Y. R. Shen. *The Principles of Nonlinear Optics.* Wiley & Sons, New York, 1984.

[88] R. Silberglitt and A. B. Harris. Effect of bound states on the excitation spectrum of a Heisenberg ferromagnet at low temperatures. *Phys. Rev. Lett.*, 19(1):30–3, July 1967.

[89] M. E. Simon, A. A. Aligia, C. D. Batista, E. R. Gagliano, and F. Leman. Excitons in insulating cuprates. *Phys. Rev. B.*, 54(6):3780–3, 1996.

[90] T. Skettrup. Urbach's rule derived from thermal fluctuations in the band gap energy. *Phys. Rev. B*, 18(6):2622–31, 1978.

[91] D. Spence, P. Kean, and W. Sibbet. 60 fs pulse generation from a self mode locked Ti:sapphire laser. *Opt. Lett.*, 16(1):42–4, 1991.

[92] J. Squier and G. Mourou. Tunable solid–state lasers create ultrashort pulses. *Laser Focus World*, 6:51, 1992.

[93] C.-K. Sun, F. Vallée, L. H. Acioli, E. P. Ippen, and J. G. Fuijimoto. Temtosecond-tunable measurement of eletron thermalization in gold. *Phys. Rev. B*, 50(20):15337–47, 1994.

[94] S. Tajima et al. Optical–phonon study of single crystals of various layered cuperates and related materials: Evidence of unique electron–phonon coupling in the CuO_2 plane. *Phys. Rev. B*, 43:10496–507, 1991.

[95] Y. Tokura et al. Cu–O network dependence of optical charge–transfer gaps and spin–pair excitations in single–CuO_2–layer compounds. *Phys. Rev. B*, 41:11657–60, 1990.

[96] Y. Toyazawa. *Prog. Theor. Phys.*, 22:455, 1959.

[97] Y. Toyozawa. *Polarons and Excitons.* Plenum Press, New York, 1963.

[98] E. B. Treacy. Optical pulse compression with diffraction gratings. *IEEE J. Quant. Electr.*, 5(9):454–8, 1969.

[99] S. Uchida et al. Optical spectra of $La_{2-x}Sr_xCuo_4$: Effect of carrier doping on the electronic structure of the CuO_2 plane. *Phys. Rev. B*, 43:7942–54, 1991.

[100] F. Urbach. The long–wavelength edge of photographic sensitivity and the electronic absorption of solids. *Phys. Rev.*, 92:1324, 1953.

[101] C. M. Varma, S. Schmitt-Rink, and E. Aabrahmans. *Solid State Commun.*, 621:681, 1987.

[102] Y. Y. Wang et al. Momentum-dependent charge transfer excitations in $Sr_2CuO_2Cl_2$ angle-resolved electron energy loss spectroscopy. *Phys. Rev. Lett.*, 77:1809–12, 1996.

[103] W. Weber. *Electronic Properties of High T_c Superconductors and Related Compounds*, page 352. Springer Verlag, Berlin, 1990.

[104] B. O. Wells. E versus k relations in many body effects in the model insulating copper oxide $Sr_2CuO_2Cl_2$. *Phys. Rev. Lett.*, 74(6):964–7, 1995.

[105] R. M. White. Spin wave renormalization in MnF_2. *Phys. Lett.*, 19(6):453–4, December 1965.

[106] M. Wortis. Bound state of two spin waves in the Heisenberg ferromagnet. *Phys. Rev.*, 132(1):85–97, October 1963.

[107] A. Yariv. *Quantum Electronics*. John Wiley and Sons, New York, 3 edition, 1988.

[108] W. B. Yelon and R. Silberglitt. Renormalization of large-wave-vectot magnons in $CrBr_3$ studied by by inelastic neutron scattering: Spin-wave correlation effects. *Phys. Rev. B*, 4(7):2280–6, October 1971.

[109] J. Zaanen, G. A. Sawatzky, and J. W. Allen. Band gaps and electronic structure of transition-metal compounds. *Phys. Rev. Lett.*, 55:418–21, 1985.

[110] F. C. Zhang and K. K. Ng. Theory of excitons in the insulating Cu-O_2 plane. *Phys. Rev. B*, 58:13520–5, 1998.

[111] F. C. Zhang and T. M. Rice. Effective hamiltonian for the superconducting Cu oxides. *Phys. Rev. B*, 37:3759–61, 1988.

[112] J. M. Zuo, M. Kim, M. O'Keeffe, and J. C. H. Spence. Direct observation of d-orbital holes and Cu–Cu bonding in Cu_2O. *Nature*, 401:49–52, 1999.

[113] J. Zyss and D. S. Chemla. *Nonlinear optical properties of organic molecules and crystals*, chapter II-1, pages 23–60. Quantum Electronics—Principles and Applications. Academic Press, Inc, New York, 1987.

A number of publications and conference contributions have been made in conjunction with this thesis

Publications in reviewed journals:

- A. B. Schumacher, J. S. Dodge, D. S. Chemla, and L. L. Miller, *Time- and energy resolved pump–probe spectroscopy of the charge transfer gap in* $Sr_2CuO_2Cl_2$, in preparation
- A. B. Schumacher, J. S. Dodge, M. A. Carnahan, R. A. Kaindl, L. L. Miller and D. S. Chemla, *Third-harmonic spectroscopy of the charge transfer gap in* $Sr_2CuO_2Cl_2$, submitted to Phys. Rev. Lett.
- R. Lövenich, A. B. Schumacher, J. S. Dodge, D. S. Chemla and L. L. Miller, *Urbach tail and temperature dependence of the charge transfer exciton in* $Sr_2CuO_2Cl_2$, accepted for publication in Phys. Rev. B.
- A. B. Schumacher, *Nonlinear spectroscopy of a strongly correlated insulator* Technical Digest. Summaries of papers presented at the Quantum Electronics and Laser Science Conference, San Francisco, CA, USA, 15-20 May 2000. Postconference Edition. Washington, DC, USA: Opt. Soc. America, 2000.
- J. S. Dodge, A. B. Schumacher, J.-Y. Bigot, D. S. Chemla, N. Ingle and M. R. Beasley *Time-resolved observation of spin wave dynamics*, Phys. Rev. Lett. **83**, 4650 (1999)
- J. S. Dodge, A. B. Schumacher, J.-Y. Bigot, D. S. Chemla, and others. *Time-resolved observation of magnon renormalization effects in* Cr_2O_3 Technical Digest. Summaries of papers presented at the Quantum Electronics and Laser Science Conference, Baltimore, MD, USA, 23-28 May 1999. Postconference Edition. Washington, DC, USA: Opt. Soc. America, 1999. p. 222-3
- J. S. Dodge, A. B. Schumacher, J.-Y. Bigot, N. Ingle, M. R. Beasley, and D. S. Chemla, *Time-resolved optical observation of spin-wave dynamics*, Magnetoresistive Oxides and Related Materials, Proceedings of Symposium JJ, 1999 Fall Materials Research Society Meeting, M. Rzchowski, M. Kawasaki, A. J. Millis, M. Rajeswari, and S. von Molnr, ed.

Invited contributions to conferences:

- M. A. Carnahan, A. B. Schumacher, R. A. Kaindl, J. S. Dodge and D. S. Chemla, *Third-harmonic spectroscopy at the charge transfer gap in* $Sr_2CuO_2Cl_2$, Quantum Electronics and Laser Science Conference (QELS), accepted as contributed talk, May 2001
- J. S. Dodge, A. B. Schumacher, D. S. Chemla, *Nonlinear optics of Mott insulators*, Fall Meeting of the Materials Research Society, Invited talk, November 2000

- A. B. Schumacher, *Nonlinear spectroscopy of strongly correlated insulators*, R. G. Herb Materials Physics Colloquium, University of Wisconsin Madison, Invited talk, September 21st, 2000

- A. B. Schumacher, J. S. Dodge, J.-Y. Bigot, D. S. Chemla, N. Ingle and M. R. Beasley, *Time resolved optical observation of spin wave dynamics* Induced Cooperative Phenomena Meeting (ICP 2000), Invited poster, June 2000

- J. S. Dodge, A. B. Schumacher, D. S. Chemla, *What can pulsed lasers tell you about correlated electrons?* Correlated Electrons Gordon Conference, Invited talk, June 29th, 2000.

- A. B. Schumacher, *Time-resolved optical spectroscopy of a strongly correlated insulator*, Quantum Electronics and Laser Science Conference (QELS), Invited talk, May 2000

- J. S. Dodge, A. B. Schumacher, D. S. Chemla, *Time-resolved nonlinear optics in strongly correlated insulators*, March Meeting American Physical Society, Invited talk, March 21st, 2000

- J. S. Dodge, A. B. Schumacher, D. S. Chemla, *Time-resolved optical observation of magnon renormalization in antiferromagnetic* Cr_2O_3, American Chemical Society Fall National Meeting, Invited talk, August 24th, 1999.

- J. S. Dodge, A. B. Schumacher, D. S. Chemla *Time-resolved observation of magnon renormalization effects in* Cr_2O_3, Quantum Electronics and Laser Science Conference (QELS), Upgraded from contributed to invited talk, May 27^{th}1999.